Spring 5-22-2021

An Examination Of Γ-valerolactone Ring Opening And Decarboxylation In Multiphase System And Over Various Solid Acid Catalysts

Xinlei Huang
Syracuse University, xhuan102@syr.edu

Abstract

Lignocellulosic biomass is an alternative carbon source for industrial applications. γ-valerolactone (GVL) is an example of biomass-derived platform chemicals that provides multiple commercial potentials. Of interest here is the acid-catalyzed ring opening of GVL to form pentenoic acid (PEA) isomers and following decarboxylation to produce butenes. In this study, GVL ring opening, and decarboxylation are examined in both liquid and gas phases over various catalytic systems aiming at improving the efficiency in selective preparation of target product.

An initial attempt was made in a biphasic reactor to improve the yield to PEA catalyzed by mineral acids (H_2SO_4). A wide range of solvents was tested for their affinity towards GVL and PEA. And alkanes appeared to have the best resolution to separate PEA from GVL. A two-parameter Margules model was further applied to regress the activity coefficient, and it successfully described the phase distribution at any given compositions in the biphasic system. Furthermore, an activity-based model was proposed to simulate the reaction in the biphasic reactor. Finally, some experiments were performed to verify the simulation results. The results turned out that theocratically, the biphasic system can significantly improve the PEA yield. However, due to practical limitations and uncertainty in simulation, the PEA yield can be enhanced by introducing a second phase but not as much as predicted in the simulation.

Furthermore, four solid acids abundant in Lewis acid sites were considered for GVL/PEA interconversion in the presence of water. SiO_2/Al_2O_3, γ-Al_2O_3, TiO_2, and ZrO_2 are characterized and tested in a pack bed reactor. Catalytic performances were examined over

various contact times and temperatures. γ-Al_2O_3 proved to be an optimistic catalyst that can realize a high yield to PEA with high selectivity at a wide operation window. SiO_2/Al_2O_3 can also achieve a high yield to PEA at certain conditions. But the selectivity to PEA was relatively low. ZrO_2 exhibited a high selectivity to PEA, but its overall activity was limited due to a lack of active sites on the surface. TiO_2 was not practical for this application. Proximity to equilibrium was found to be the critical element influencing selectivity to PEA. Meanwhile, the GVL ring opening activity was more controlled by Lewis acidity instead of Brønsted acidity in this system. Deactivation was observed on these materials, and calcination can only partially regenerate the catalysts.

Finally, different framework zeolites that had a high density of Brønsted acid sites were examined. GVL decarboxylation was performed over MFI, FAU, BEA, FER, and MOR zeolites in the gas phase. These zeolites were well characterized and were found that Brønsted acid site density, Lewis acid site density as well as BAS: LAS ratio increased as the aluminum content decreased in zeolites. Brønsted acid site was the primary active site for GVL decarboxylation instead of the Lewis acid site. Brønsted acidity in different framework zeolites seemed to be identical. However, the intrinsic activity of materials was not only dependent on the strength of Brønsted acid sites. Significantly high activity was observed in MFI framework zeolites. The confinement effect and the local environment of acid sites may contribute to the increased activity in MFI zeolites. Severe deactivation was found in zeolites due to coking formation. But the catalysts were fully regenerable after calcination. Pore diameter and micropore area were the most critical elements for designing an efficient and stable zeolite catalyst.

An examination of γ-valerolactone ring opening and decarboxylation in multiphase system and over various solid acid catalysts

By

Xinlei Huang

B.Sc, Central China Normal University, 2013

Dissertation

Submitted in partial fulfillment of the requirements for the Degree of

Doctor of Philosophy in Chemical Engineering

Syracuse University

May 2021

Acknowledgments

I would like to thank my parents, Jianying and Yunlong, for raising me up in a healthy and positive environment. In my childhood, they gave me sufficient love and taught me how to be a good man. I have been living in my hometown, Wuhan, for almost 25 years and never left there except traveling. When I decided to go abroad to expand my horizons, I was appreciated that my parents supported me as much as they can. I also would like to thank my grandparents, Chunyang and Jinyu, for their understanding of my choice. In the six years of my Ph.D. life, I only went back to my hometown once. Without the support and love from my family, I cannot make it so far.

I would also like to thank my girlfriend, Jiang Zhu, who has kept me company for the last three years during my Ph.D. study. You always take care of my life and cook delicious dishes for me. When I was busy on experiments in the late nights, you always wait for me at home. You really have enriched my life and made me a better person. I cannot wait for life together in the future.

Moreover, I would like to especially thank my little friends: Silly, Chaofan, Meimei, and Oolong, four cats living with me. Thanks for being there next to me when I was working on my computer. Your existences really bring more color into my life.

I would show special gratitude to my advisor, Professor Jesse Q. Bond, who gave me this invaluable chance to be a member of his lab. At first, I was not a Ph.D. student, and you allowed me to join the lab and started my own experiments at an early stage. Your encouragement and guidance enlighten me, showing me what needs to be done as an excellent academic researcher. Your attitude towards challenges in life and class also

taught me what I should do when facing trials and errors in my life. Under your leadership, the group was really like a family to me. And I will remember the life I have in your lab.

Also, to everyone in Jesse`s lab, thank you for all the help and guidance in these years. I would show my gratitude to Omar Ali Abdelrahman, Anargyros Chatzidimitriou, Christian Jungong, Joshua Gopeesingh, Ran Zhu, Zijian Wang, Weixuan Huang, Patrick Howe, Bowei Liu, Siwen Wang, Xin Gao, Robert Glasser, Li Zhi, Robson Luis Schuarca, Weixin Li, and Emir Hadzic. It is an honor to work with you in the lab. Omar, Argy, and Christian, thanks for your early guidance when I first stepped into the lab. Especially Argy, who taught me characterization skills such as TPD and FTIR. This knowledge lays the foundation for me to go deep into the world of solid acids. Zijiang Wang, and Weixuan Huang, thanks for giving me the chance to train you to be a qualified researcher. Bowei Liu, Siwen Wang, and Robert Glasser, thanks for assisting me with some characterization works. And the most important one, Ran Zhu, you are not only a college but also my best friend here in Syracuse. You will always be my best friend, and we will explore more in the world catalysis in the future. I will send you a portable Pizza maker once it comes out.

I would also thank Syracuse University and the Department of Biomedical and Chemical Engineering. Ameila and Jason, thanks for the help in dealing with the ordinary affairs. Professor Ashok S. Sangani, thanks for your early guidance and suggestion in the simulation and modeling classes. I learned and got motivated a lot from it. Professor Lawrence L. Tavlarides, and Professor Viktor J. Cybulskis, thanks for your expertise in kinetics and surface structures, which benefit me and sharpen my understanding as a surface scientist. Professor Ian D. Hosein, thanks for sharing the knowledge you have in

the sustainable development of energy systems. Furthermore, thank everyone who works on the third floor of Link Hall for creating a healthy and efficient working environment.

I want to also acknowledge Professor Micheal T. Timko from Worcester Polytechnical Institute, Professor Stephanie G. Wettstein from Montana State University, and Professor Lawrence L. Tavlarides from Syracuse University. Thanks for giving me the chance to perform the catalyst characterization for your catalysts. These collaboration opportunities are precious, and they really sharpen my understanding of surface science.

Last but not least, I would also appreciate all members of my defense committee:

Professors Arindam Chakraborty, Ashok S.Sangani, Ian D. Hosein, Lawrence L. Tavlarides, and Viktor J.Cybulskis,

Thanks for your patience and assistance in this final part of my journey at Syracuse University.

Life in Syracuse was challenging and rewarding. And I have a lot of good memories. Even though I have to move, everything here will always be remembered in my life.

April 2021

Table of Contents

Chapter 3 Thermodynamic and kinetic analysis of γ-valerolactone ring opening in multiphase reactors

Chapter 4 Optimization of selective pentenoic acids production from ring opening of gamma valerolactone over solid acid catalysts

List of Figures

List of tables

Chapter 1

Introduction

1.1 Energy system today

The rapid development of the economy depends on a large amount of energy consumption, which inevitably results in excessive greenhouse gas emissions (GHG) and leads to air pollution issues and severe climate changes. The typical greenhouse gas is carbon dioxide, making up 65% of the total GHG emission. Since 1970, the global CO_2 emission has increased 90% due to industrial development and fossil fuel combustion [1]. The increased CO_2 concentration in the atmosphere exacerbated global warming and decreased the biological activity on earth [2]. The United States, as the most developed country with the highest GPD in the world, released more than 5000 million metric tons of CO_2 equivalent in 2017. This amount makes the US the highest CO_2 emissions in the developed countries and the second highest CO_2 emissions in the world [3]. To curtail the greenhouse gas emission and maintain long-term sustainable development, the US government has taken several measures to control greenhouse gas (GHG) emissions [4]. One strategy is to displace traditional energy sources with renewable energy sources with relatively low GHG emissions [5].

Based on figure 1.1, US total energy consumption has increased dramatically from 30 quads to 102 over the past 60 years. Petroleum has always been the primary energy consumption source, followed by nature gas since 1960. In addition, renewable energy consumption has also rapidly increased since 1970, while the US nuclear energy consumption has remained the same since 2008. On the contrary, coal consumption has significantly dropped in the past ten years, even though it once reached peak value near 2008. This can be ascribed to the fact that the US decided to gradually displace coal with renewables in many areas in 2008 [6]. Consequently, in 2019, renewable energy consumption surpassed coal consumption for the first time in history. Moreover, the wide use of renewable energy has led to a 15% decrease in global greenhouse gas emissions since 2008 [7].
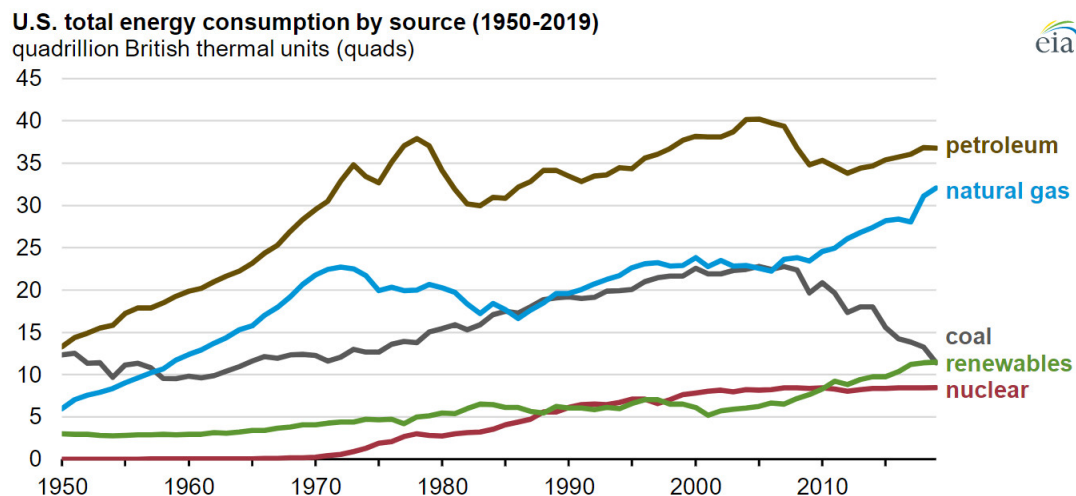
Figure 1.1: US total energy consumption by source since 1950. [6]

Renewable energy has played a significant role in providing sustainable development in the long term. Based on EIA reports, renewables will eventually surpass petroleum and natural gas on a global scale, becoming the dominant energy source by 2050 [8].

Nowadays, renewable energy is applied in multiple sectors in daily life, such as electric generation, transportation, residential, commercial, and industrial consumptions [9]. Solar, geothermal, hydro, and wind energy are primarily consumed in generating electric power. However, biomass, which includes biogenic waste, wood, and biofuel, is used in every aspect. Especially, biofuel and co-products from the biomass upgrading process are significant contributors to industrial and transportation energy consumption [10].

Biomass has emerged as a promising carbon alternative to address the environmental impact issues caused by petroleum and natural gas-based product consumption. However, the relevant technologies still cannot meet the demand of the rapid market development. Biofuel and bio-based chemicals are two major applications of biomass. By 2030, the US government attempts to implement the Billion-Ton Bioeconomy plan to reduce the total GHG emission by 26-28% compared with the 2005 level [11]. Among all fields, transportation is considered one the most

significant contributors to high GHG emissions. Thus, displacing fossil fuels with biofuels is a primary target. Since 2005, the United States Environmental Protection Agency has been implementing the renewable fuel standard mandate (RFS2) to supervise the biofuel market [12]. In the RFS2, the four kinds of fossil fuel replacement: conventional renewable fuel, advanced biofuels, biomass-based diesel, and cellulosic biofuel, are clearly defined with a level of GHG reduction. Conventional biofuel contains ethanol and biobutanol made from corn starch with a total of 20% GHG reduction. Advanced biofuels are ethanol made from sugarcane and grain sorghum with a total of 50% GHG reduction. Also, the naphtha and liquefied petroleum gas (LPG) produced from camelina oil are considered in this type. Biomass-based diesel represents the biodiesel made from soybean oil, canola oil, waste oil, and animal fats with 50% GHG reduction. The final category is cellulosic biofuels which are made from corn stover, wood chips, crop residues, and biogas through thermochemical pyrolysis, gasification, and biochemical fermentation with catalytic upgrading with a total of 60% GHG reduction [13]. Based on the EPA`s report in 2019, the production capacity for conventional biofuel and biodiesel can meet the demand for annual consumption. However, due to the low efficiency in conversion technologies, cellulosic biofuel production is still far behind the requirement. The EPA has decreased the annual anticipation from 100 million gallons of cellulosic biofuel production to 5 million gallons [14].

Besides biofuels, another application of biomass that has great potential and needs attention is bio-based chemicals. The biomass feedstock is abundant but not unlimited. Considering ethical reasons, biomass that served as a food supply cannot be used as a carbon source in the biomass upgrading process. After excluding food recourses, in 2014, the US annual biomass availability is around 365 million dry tons, and this number will rise to 1042 million dry tons by 2030 [15]. The allocation
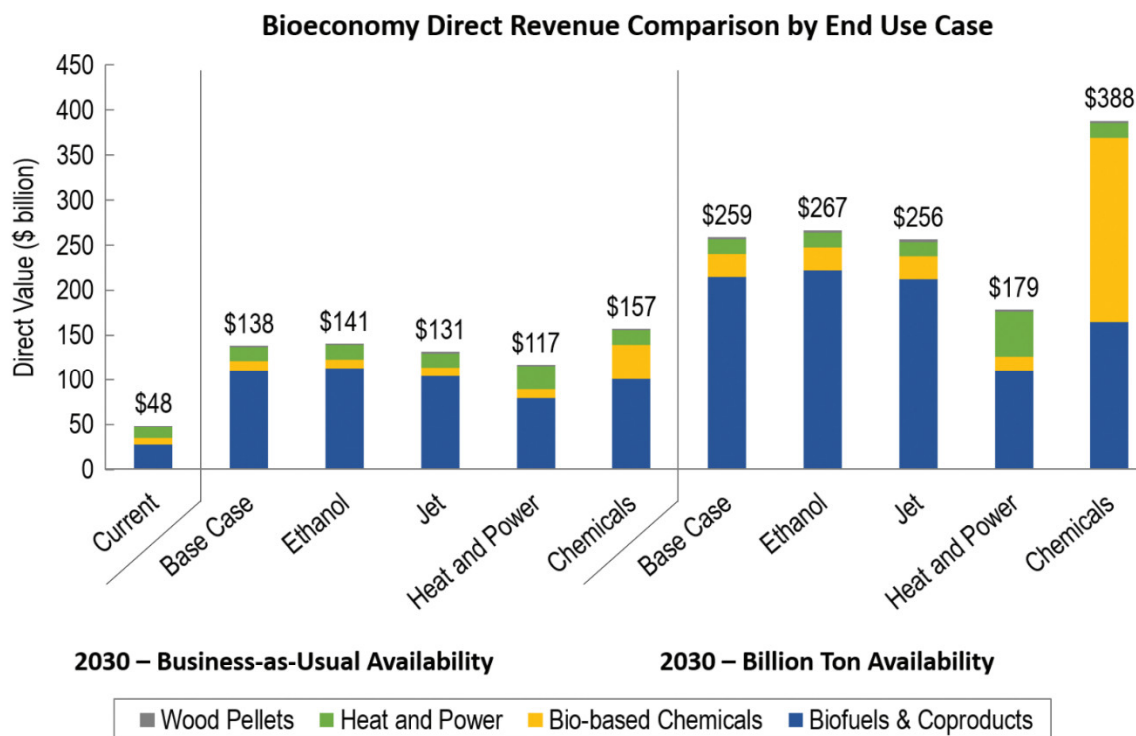
Figure 1.2: Bioeconomy direct revenue comparison based on different allocation of raw biomass materials in 2030. [11]

of raw materials in different applications will have a considerable impact on the bioeconomy output. Current application of biomass includes ethanol production, biogas production, bio-based chemicals production, diesel-jet fuel production, electricity generation, and heat generation. Among these, bio-based chemicals have the potential to generate the most value in the future. Figure 1.2 illustrates that if 50% of agricultural residues, energy crops, and algae resources are reallocated to produce bio-based chemicals, biomass relevant Business can contribute almost $388 billion and 1.75 million jobs to the US economy in 2030 [11]. Therefore, aiming to enhance the bioeconomy and achieve a low-carbon society, there is an urgent need to develop advanced biomass upgrading processes that can deliver high-quality bio-based fuels and chemicals on a large scale.

1.2 Biomass as a reliable carbon alternative

Biomass refers to the renewable organic materials derived from plants and animals, including wood, landfill gas, energy crops, waste from forests, and agriculture [16]. The energy of biomass is originally from solar energy, which is stored through the photosynthesis of plants over the years. Most of the biomass is distributed in plants and bacteria [17]. The fundamental structures of plants are cellulose, hemicellulose, and lignin.

Cellulose is the linear polysaccharide made of glucose (C_6 sugar) units. It is the primary structure of a plant cell, and its shape is a long straight macrofibre [18]. Hemicellulose is a branched polysaccharide consisting of C_5 and C_6 sugar monomers such as xylose, galactose, and glucose [19]. It can form hydrogen bonds with lignin and cellulose, existing as a cross-linked structure. Lignin is a phenolic macromolecule connected by some phenylpropane units. It is the foundation of the cell wall and maintains the whole wood cell structure [20]. Figure 1.3 illustrates the typical distribution and composition of lignocellulose in plants. The distribution of cellulose,
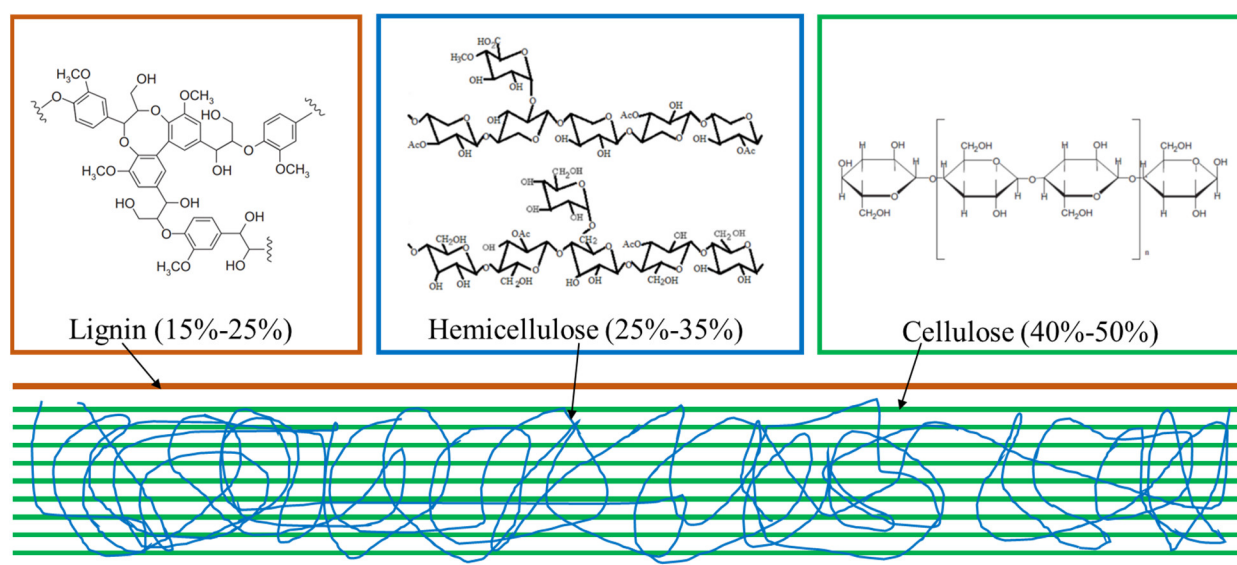
Figure 1.3: Chemical structure of lignocellulose and their distributions in plants.

hemicellulose, and lignin has a significant difference based on the type of plants [21]. Of the interest here is the lignocellulose biomass, which is more abundant in cellulose and hemicellulose.

Comparing to traditional biomass, cellulose and hemicellulose content in lignocellulose biomass can be up to 85%. They can be used to produce cellulosic biofuel and bio-based chemicals [22]. The latest developed processes for converting cellulose and hemicellulose in the woody biomass to liquid transportation fuels are limited to thermochemical and hydrolysis pathways such as syngas FT pathway, pyrolysis bio-oil pathway, hydrolysis-ketonization & condensation pathway, and biochemical pathways [23]. Companies have applied some technologies in the commercial-scale production of biofuels. For example, KiOR company uses catalytic pyrolysis & hydrotreating to produce to realize a 41-million-gallon annual production. The gasification & F-T synthesis to hydrocarbons has been commercialized by the Clear Fuels company in Collinwood (TN) to generate cellulosic biofuels, which can reach 20 million gallons per year. However, other companies only use enzymatic hydrolysis to produce ethanol [24]. The market is still waiting for more types of biofuel and biobased products different than ethanol.

Based on the report from Pacific Northwest National Laboratory (PNNL) and National Renewable Energy Laboratory (NREL), twelve chemicals from biomass upgrading are listed as top value intermediate molecules [25]. These compounds possess the potential to be further transformed into profitable industrial products. Figure 1.4 illustrates the chemical structure of twelve bio-based chemicals. Of various compounds with economic potential, levulinic acid (LA), a five-carbon ketoacid that can be used as a precursor to multiple industrial intermediates [26], has received a lot of attention in recent years. Its production technology has been well optimized in the past five years. Many companies have realized a commercial-scale production capability of LA. For example, the company GF Biochemicals in Italy has achieved LA production with an annual
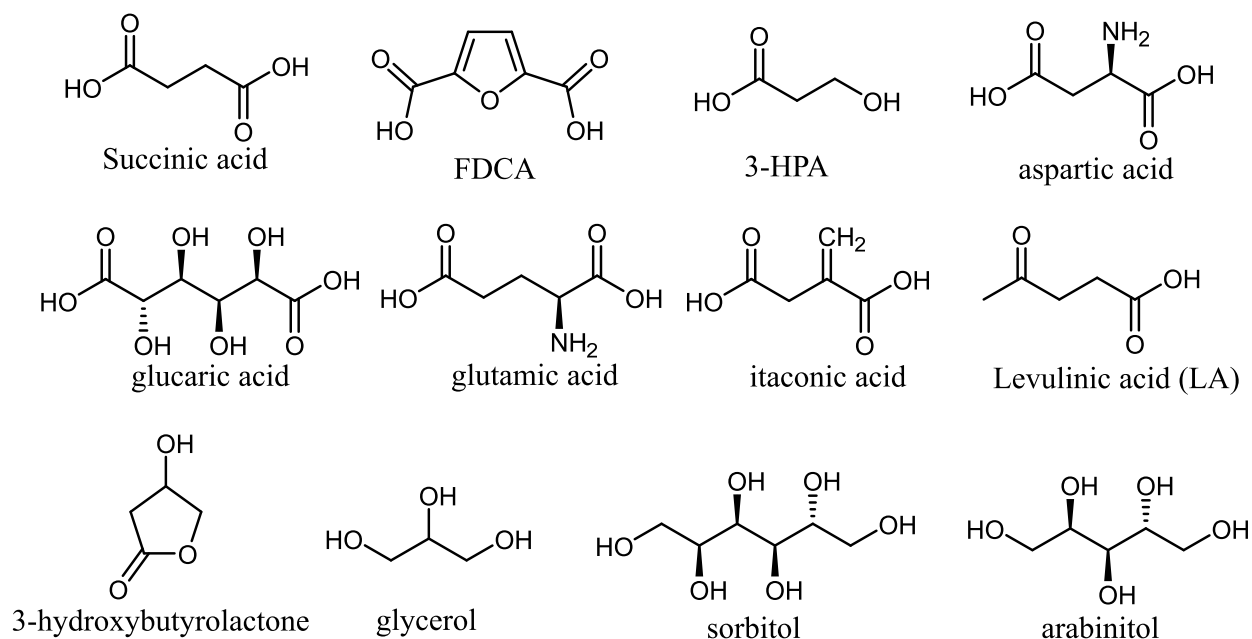
Figure 1.4: Top-value added chemicals from biomass upgrading.

capacity of 10 km^3. An assessment from a plant in Indonesia showed that it could reach a minimum LA m production capacity of 7.7 tons per day. Currently, LA can be produced through the first generation of biomass (starchy and sugary biomass), the second generation of biomass (food waste and lignocellulosic biomass), and the third generation of biomass (algal biomass) [27-30].

There are commonly two pathways to produce LA: cellulose pathway and hemicellulose pathway. The cellulose pathway consists of 4 stages: hydrolysis of cellulose in the raw biomass materials over Brønsted acid sites to produce glucose, isomerization of glucose over Lewis acid catalysts to form fructose, dehydration of fructose to generate 5-hydroxymethylfurfural (HMF) over bifunctional acid catalysts, and finally, the rehydration of HMF to give LA [31]. The hemicellulose pathway involves the hydrolysis of hemicellulose to form xylose, dehydration of xylose in an acid environment to deliver furfural, hydrogenation of furfural to give furfural alcohol, and final hydration to generate LA [32]. LA can be used as a precursor to produce other valuable chemicals such as α-angelica lactone, 2-butanone, maleic anhydride, 2-MTHF, acrylic acid, and so on [33-

40]. Figure 1.5 demonstrates various applications of LA. One particular application of LA is the production of γ-valerolactone (GVL), which can be acquired from the hydrogenation of LA over metal catalysts [41].
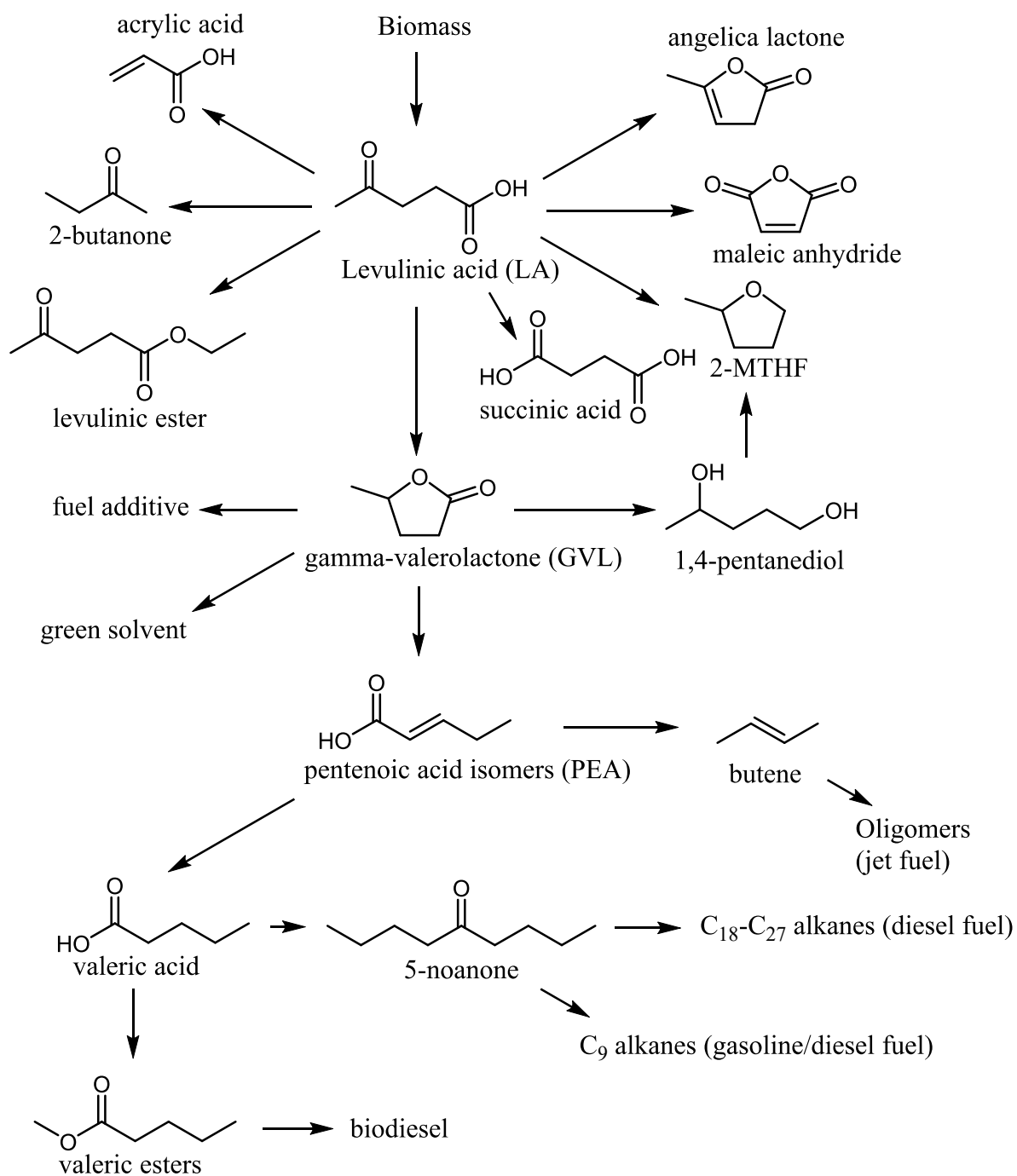
Figure 1.5: Landscape of potential application of levulinic acid and γ-valerolactone.

1.3 GVL as a platform chemical

The traditional uses of gamma γ-valerolactone (GVL) are mostly food additives [42]. And the high boiling point and low melting point render GVL preferable as a fuel additive than ethanol. In recent years, more studies have been performed to develop its potential for multipurpose applications besides additive. Nowadays, GVL serves as a critical lignocellulosic platform chemical that possesses the potential to be subsequently converted into biodiesel, bio-jet fuel, acrylic polymers, gasoline blenders. Figure 1.5 also summarizes the primary application of GVL.

Considering the stability and zero-toxicity, GVL is recognized as a sustainable polar solvent. Lignin is hard to break and insoluble in most solvents. Meanwhile, GVL can promote lignin solubility by breaking down the hydrogen bonds in the lignin structure [43-45]. In a GVL mineral acid system, cellulose can be transformed into LA and formic acid with a total yield of 70% [26]. In a recent study, GVL displaced N-methyl-2-pyrrolidone (NMP) and served as a coating solvent to manufacture lithium-ion battery electrodes [46].

Moreover, 2-MTHF can be efficiently synthesized from dehydration of 1,4-pentanediol (1,4-PDO), which is obtained through hydrogenation of GVL over Cu/Al_2O_3 catalyst. The overall yield of MTHF can reach 90% at 473K [47]. Also, 1,4-PDO, another valuable industrial intermediate that can be converted into 1,4 pentadiene through dehydration reaction over self-pillared pentasil (SPP) catalyst, can be selectively prepared from the hydrogenation of GVL over $Zn_{1.5}Cu/Al_2O_3$ catalysts at 473K [48].

Another application of GVL is to produce renewable jet fuels [49]. Two packed bed reactors and distillation towers are required in this process. At 648K, GVL is initially decarboxylated into butene and CO_2 in a SiO_2/Al_2O_3 or H-ZSM-5 reactor. Both products are sent to the subsequent

reactors packed with H-ZSM-5 or Amberlyst-70 to generate C_{8+} alkenes. The overall yield of butene through these two-step reactions can reach 75%.

In addition to 2-MTHF and bio-jet fuel, C_{18}-C_{27} diesel fuels and C_9 alkane gasoline can also be obtained from GVL [50-51]. Through series ring opening & hydrogenation reaction over Pd/Nb$_2$O$_5$, valeric acid can be generated. It is further ketonized and reduced in H_2 to form 5-nonanone in the presence of Ce and Ru/C catalysts. On the one hand, C_9 alkane gasoline is produced from 5-nonanol through dehydration and isomerization reaction with H-ZSM-5 catalysts. On the other hand, C_9-C_{18} alkanes diesel fuels are produced from 5-nonanol via a series of dehydration, oligomerization, and hydrogenation reactions.

Velaric biofuels, as known as biodiesel, can also be produced from GVL conversion. The fatty acid methyl ester (FAME) is the primary chemical structure in biodiesel. It is usually synthesized from plant oils through transesterification. Valeric esters have a similar structure to FAME. Although its energy density is lower than FAME, the better physical properties still make it a decent diesel fuel. Pentyl valerate can be generated from the esterification of pentanoic acid in the presence of alcohols and solid acid. Meanwhile, pentanoic acid can be obtained through continuous ring-opening and hydrogenation of GVL. Numerous catalysts have been developed for this reaction. Pd/HY, SiO$_2$-ZrO$_2$, and Pd/Nb$_2$O$_5$ are all proven to be efficient catalysts, which can lead to at least 90% yield [52-54].

Among these conversion pathways, several pilot-scale tests have been performed to examine the economic potential of the GVL application [49]. One proposed commercial strategy is the integrated catalytic process for converting whole biomass from red maple into aviation fuels. It aims at an annual production capacity of 38 million gallons of liquid fuels for a selling price of $4.75 per gallon. However, considering the current aviation fuel price of $1.08 per gallon, this

price is still not competitive [55]. There are several technical issues that can reduce the production cost waiting to be addressed. One of such difficulties is the scale-up of ring opening and decarboxylation of GVL process. In the GVL decarboxylation reactor, the catalysts will be deactivated in the initial 24 hours on steam at 648K, and this deficiency makes it unreliable to maintain a high butene yield over a long period of time. Also, the high reaction temperature and frequent need for regeneration of catalysts increase the energy consumption and operational cost in the system [56]. Thus, the fundamental knowledge of GVL ring opening and decarboxylation is essential for improving the PEA yield and butene yield. The comprehensive examination of kinetics and stability of GVL ring opening over different catalysts will provide vital information for designing catalysts with higher efficiency. And this is the primary concern of this thesis.

1.4 Research Overview
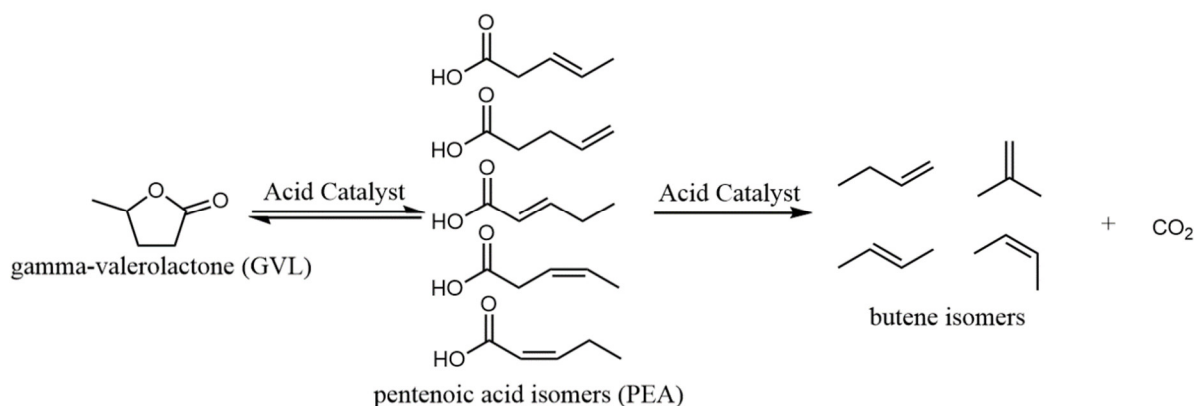
Figure 1.6: Reaction pathway of GVL ring opening and PEA decarboxylation.

The primary reaction we studied in this paper is GVL ring opening and the following PEA decarboxylation (Figure 1.6). Chapter 2 briefly summarized experimental methods, catalyst characterizations techniques, and reactors for activity tests in this study. The reaction kinetics and thermodynamics of GVL ring opening in the condensed phase, comprehensive solvent selection and thermodynamic modeling in the biphasic reactor to improved PEA yields and selectivity are discussed in Chapter 3. After attempts taken in a homogenously catalyzed environment, the heterogeneous catalysis conditions are also considered. Chapter 4 explores the activity of GVL ring opening over various solids acid abundant of Lewis acid sites (silica alumina, gamma alumina, Titanium oxide, and Zirconium dioxide). A wide range of temperature and contact time has been examined in a packed bed reactor to find the optimal operating condition to achieve maximum PEA yield and selectivity. Moreover, all catalysts are characterized and the relationship between catalysts structure and their performance on GVL ring opening and decarboxylation is explored. Lastly, the stability of all catalysts is examined and significant factors for design a high activity and regenerable catalysts for GVL ring opening are proposed. In Chapter 5, the catalytic performance of GVL decarboxylation over various zeolites (MFI, FAU, MOR, FER, and BEA) is studied. Different from materials covered in the previous chapter, zeolite is abundant in Brønsted

acid sites, and they are microporous materials. Extensive sets of kinetic data for both GVL ring opening and decarboxylation over zeolites are collected to resolve the influence of pore structure, acid site type and acid site concentrations on production rate, catalysts stability and intrinsic activity of different materials. Finally, in Chapter 6, several future recommendations with potential value are proposed to improve our understanding of the application of GVL-PEA related biomass technologies. Future works will cover: 1) Investigating ZrO_2 catalysts prepared from zirconyl nitrate hydrate as a Lewis acid catalyst to catalyze GVL ring opening; 2) Microkinetic modeling of GVL ring opening and decarboxylation reaction based on our extensive data sets collected in Chapter 5 to examine the transition state formation in the different zeolites; 3) Exploring potential use of PtSn catalysts to synthesize valuable chemicals such as 2-MTHF and 1,4-PDO from the hydrogenation of GVL or LA in one single-run reaction; 4) Examining the possibility of selective preparation of pentadiene and butadiene from biomass derivatives.

1.5 References

1. Olivier, J. G., Peters, J. A., & Janssens-Maenhout, G. (2012). Trends in global CO2 emissions. 2012 report.
2. Norby, R. J., & Luo, Y. (2004). Evaluating ecosystem responses to rising atmospheric CO2 and global warming in a multi-factor world. *New phytologist*, *162*(2), 281-293.
3. Boden, T. A., Marland, G., & Andres, R. J. (2009). Global, regional, and national fossil-fuel CO2 emissions. *Carbon dioxide information analysis center, Oak ridge national laboratory, US department of energy, Oak Ridge, Tenn., USA doi*, *10*.
4. Rausch, S., Metcalf, G. E., Reilly, J. M., & Paltsev, S. (2010). *Distributional implications of alternative US greenhouse gas control measures*.
5. Menyah, K., & Wolde-Rufael, Y. (2010). CO2 emissions, nuclear energy, renewable energy and economic growth in the US. *Energy policy*, *38*(6), 2911-2915.
6. U.S. Energy Information Administration. (2021). *March 2021 Monthly Energy Review*. (DOE/EIA-0035(2021/3). U.S. Department of Energy.
7. U.S. Energy Information Administration. (2021). *Short-Term Energy Outlook*. U.S. Department of Energy.
8. Stephen Nalley, Angelina LaRose. (2021). *Annual Energy Outlook 2021 with projections to 2050*. U.S. Energy Information Administration-U.S. Department of Energy.
9. Bhattacharya, M., Paramati, S. R., Ozturk, I., & Bhattacharya, S. (2016). The effect of renewable energy consumption on economic growth: Evidence from top 38 countries. *Applied Energy*, *162*, 733-741.
10. Fernandes, S. D., Trautmann, N. M., Streets, D. G., Roden, C. A., & Bond, T. C. (2007). Global biofuel use, 1850–2000. *Global Biogeochemical Cycles*, *21*(2).
11. Rogers, J. N., Stokes, B., Dunn, J., Cai, H., Wu, M., Haq, Z., & Baumes, H. (2017). An assessment of the potential products and economic and environmental impacts resulting from a billion ton bioeconomy. *Biofuels, Bioproducts and Biorefining*, *11*(1), 110-128.
12. Schnepf, R. D., & Yacobucci, B. D. (2010). *Renewable fuel standard (RFS): overview and issues* (Vol. 40155). Congressional Research Service Washington, DC.
13. United States Environmental Protection Agency. (2020). *Overview for Renewable Fuel Standard*. U.S. EPA.
14. Council, N. R. (2012). *Renewable fuel standard: Potential economic and environmental effects of US biofuel policy*. National Academies Press.
15. Perlack, R. D., Eaton, L. M., Turhollow Jr, A. F., Langholtz, M. H., Brandt, C. C., Downing, M. E., Graham, R. L., Wright, L. L., Kavkewitz, J. M., & Shamey, A. M. (2011). US billion-ton update: biomass supply for a bioenergy and bioproducts industry.
16. Vassilev, S. V., Baxter, D., Andersen, L. K., & Vassileva, C. G. (2010). An overview of the chemical composition of biomass. *Fuel*, *89*(5), 913-933.
17. Bar-On, Y. M., Phillips, R., & Milo, R. (2018). The biomass distribution on Earth. *Proceedings of the National Academy of Sciences*, *115*(25), 6506-6511.
18. Nevell, T. P., & Zeronian, S. H. (1985). Cellulose chemistry and its applications.
19. Carvalheiro, F., Duarte, L. C., & Gírio, F. M. (2008). Hemicellulose biorefineries: a review on biomass pretreatments. *Journal of Scientific & Industrial Research*, 849-864.

20. Vanholme, R., Morreel, K., Ralph, J., & Boerjan, W. (2008). Lignin engineering. *Current opinion in plant biology*, *11*(3), 278-285.

21. Huber, G. W., Chheda, J. N., Barrett, C. J., & Dumesic, J. A. (2005). Production of liquid alkanes by aqueous-phase processing of biomass-derived carbohydrates. *Science*, *308*(5727), 1446-1450.

22. Brown, T. R., & Brown, R. C. (2013). A review of cellulosic biofuel commercial-scale projects in the United States. *Biofuels, Bioproducts and Biorefining*, *7*(3), 235-245.

23. Alonso, D. M., Bond, J. Q., & Dumesic, J. A. (2010). Catalytic conversion of biomass to biofuels. *Green chemistry*, *12*(9), 1493-1513.

24. Sims, R. E., Mabee, W., Saddler, J. N., & Taylor, M. (2010). An overview of second generation biofuel technologies. *Bioresource technology*, *101*(6), 1570-1580.

25. Werpy, T., & Petersen, G. (2004). *Top value added chemicals from biomass: volume I--results of screening for potential candidates from sugars and synthesis gas*.

26. Wettstein, S. G., Alonso, D. M., Chong, Y., & Dumesic, J. A. (2012). Production of levulinic acid and gamma-valerolactone (GVL) from cellulose using GVL as a solvent in biphasic systems. *Energy & Environmental Science*, *5*(8), 8199-8203.

27. Chang, C., Cen, P., & Ma, X. (2007). Levulinic acid production from wheat straw. Bioresource technology, 98(7), 1448-1453.

28. Galletti, A. M. R., Antonetti, C., De Luise, V., Licursi, D., & Nassi, N. (2012). Levulinic acid production from waste biomass. *BioResources*, *7*(2), 1824-1835.

29. Rackemann, D. W., & Doherty, W. O. (2011). The conversion of lignocellulosics to levulinic acid. *Biofuels, Bioproducts and Biorefining*, *5*(2), 198-214.

30. Jeong, G. T., Ra, C. H., Hong, Y. K., Kim, J. K., Kong, I. S., Kim, S. K., & Park, D. H. (2015). Conversion of red-algae Graciaria verrucosa to sugars, levulinic acid and 5-hydroxymethylfurfural. *Bioprocess and biosystems engineering*, *38*(2), 207-217.

31. Weingarten, R., Conner, W. C., & Huber, G. W. (2012). Production of levulinic acid from cellulose by hydrothermal decomposition combined with aqueous phase dehydration with a solid acid catalyst. *Energy & Environmental Science*, *5*(6), 7559-7574.

32. Gürbüz, E. I., Wettstein, S. G., & Dumesic, J. A. (2012). Conversion of hemicellulose to furfural and levulinic acid using biphasic reactors with alkylphenol solvents. *ChemSusChem*, *5*(2), 383-387.

33. Al-Shaal, M. G., Hausoul, P. J., & Palkovits, R. (2014). Efficient, solvent-free hydrogenation of α-angelica lactone catalysed by Ru/C at atmospheric pressure and room temperature. *Chemical Communications*, *50*(71), 10206-10209.

34. Min, K., Kim, S., Yum, T., Kim, Y., Sang, B. I., & Um, Y. (2013). Conversion of levulinic acid to 2-butanone by acetoacetate decarboxylase from Clostridium acetobutylicum. *Applied microbiology and biotechnology*, *97*(12), 5627-5634.

35. Chatzidimitriou, A., & Bond, J. Q. (2015). Oxidation of levulinic acid for the production of maleic anhydride: breathing new life into biochemicals. *Green Chemistry*, *17*(8), 4367-4376.

36. Phanopoulos, A., White, A. J., Long, N. J., & Miller, P. W. (2015). Catalytic transformation of levulinic acid to 2-Methyltetrahydrofuran using ruthenium–N-Triphos complexes. *Acs Catalysis*, *5*(4), 2500-2512.

37. Dharne, S., & Bokade, V. V. (2011). Esterification of levulinic acid to n-butyl levulinate over heteropolyacid supported on acid-treated clay. *Journal of Natural Gas Chemistry*, *20*(1), 18-24.

38. Podolean, I., Kuncser, V., Gheorghe, N., Macovei, D., Parvulescu, V. I., & Coman, S. M. (2013). Ru-based magnetic nanoparticles (MNP) for succinic acid synthesis from levulinic acid. *Green chemistry*, *15*(11), 3077-3082.

39. Li, M., Li, G., Li, N., Wang, A., Dong, W., Wang, X., & Cong, Y. (2014). Aqueous phase hydrogenation of levulinic acid to 1, 4-pentanediol. *Chemical Communications*, *50*(12), 1414-1416.

40. Hu, X., Song, Y., Wu, L., Gholizadeh, M., & Li, C. Z. (2013). One-pot synthesis of levulinic acid/ester from C5 carbohydrates in a methanol medium. *ACS Sustainable Chemistry & Engineering*, *1*(12), 1593-1599.

41. Galletti, A. M. R., Antonetti, C., De Luise, V., & Martinelli, M. (2012). A sustainable process for the production of γ-valerolactone by hydrogenation of biomass-derived levulinic acid. *Green Chemistry*, *14*(3), 688-694.

42. Horváth, I. T., Mehdi, H., Fábos, V., Boda, L., & Mika, L. T. (2008). γ-Valerolactone—a sustainable liquid for energy and carbon-based chemicals. *Green Chemistry*, *10*(2), 238-242.

43. Lê, H. Q., Alonso, D. M., Bond, J. Q., Serrano-Ruiz, J. C., & Dumesic, J. A. (2010). Production of liquid hydrocarbon transportation fuels by oligomerization of biomass-derived C 9 alkenes. *Green chemistry*, *12*(6), 992-999.Zaitseva, A., Pokki, J. P., Ståhl, M., Alopaeus, V., & Sixta, H. (2016). Solubility of organosolv lignin in γ-valerolactone/water binary mixtures. *ChemSusChem*, *9*(20), 2939.

44. Luterbacher, J. S., Azarpira, A., Motagamwala, A. H., Lu, F., Ralph, J., & Dumesic, J. A. (2015). Lignin monomer production integrated into the γ-valerolactone sugar platform. *Energy & Environmental Science*, *8*(9), 2657-2663.

45. Tabasso, S., Grillo, G., Carnaroglio, D., Calcio Gaudino, E., & Cravotto, G. (2016). Microwave-assisted γ-valerolactone production for biomass lignin extraction: a cascade protocol. *Molecules*, *21*(4), 413.

46. Ravikumar, V. R., Schröder, A., Köhler, S., Çetinel, F. A., Schmitt, M., Kondrakov, A., ... & Schmidt-Hansberg, B. (2021). γ-Valerolactone: An Alternative Solvent for Manufacturing of Lithium-Ion Battery Electrodes. *ACS Applied Energy Materials*, *4*(1), 696-703.

47. Obregón, I., Gandarias, I., Ocio, A., García-García, I., de Eulate, N. A., & Arias, P. L. (2017). Structure-activity relationships of Ni-Cu/Al2O3 catalysts for γ-valerolactone conversion to 2-methyltetrahydrofuran. *Applied Catalysis B: Environmental*, *210*, 328-341.

48. Du, X. L., Bi, Q. Y., Liu, Y. M., Cao, Y., He, H. Y., & Fan, K. N. (2012). Tunable copper-catalyzed chemoselective hydrogenolysis of biomass-derived γ-valerolactone into 1, 4-pentanediol or 2-methyltetrahydrofuran. *Green Chemistry*, *14*(4), 935-939.

49.   Bond, J. Q., Alonso, D. M., Wang, D., West, R. M., & Dumesic, J. A. (2010). Integrated catalytic conversion of γ-valerolactone to liquid alkenes for transportation fuels. *Science*, *327*(5969), 1110-1114.

50.   Serrano-Ruiz, J. C., Braden, D. J., West, R. M., & Dumesic, J. A. (2010). Conversion of cellulose to hydrocarbon fuels by progressive removal of oxygen. *Applied Catalysis B: Environmental*, *100*(1-2), 184-189.

51.   Alonso, D. M., Bond, J. Q., Serrano-Ruiz, J. C., & Dumesic, J. A. (2010). Production of liquid hydrocarbon transportation fuels by oligomerization of biomass-derived C 9 alkenes. *Green chemistry*, *12*(6), 992-999.

52.   Chan-Thaw, C. E., Marelli, M., Psaro, R., Ravasio, N., & Zaccheria, F. (2013). New generation biofuels: γ-valerolactone into valeric esters in one pot. *RSC advances*, *3*(5), 1302-1306.

53.   Lange, J. P., Price, R., Ayoub, P. M., Louis, J., Petrus, L., Clarke, L., & Gosselink, H. (2010). Valeric biofuels: a platform of cellulosic transportation fuels. *Angewandte Chemie International Edition*, *49*(26), 4479-4483.

54.   Yan, K., Lafleur, T., Wu, X., Chai, J., Wu, G., & Xie, X. (2015). Cascade upgrading of γ-valerolactone to biofuels. *Chemical Communications*, *51*(32), 6984-6987.

55.   Davidson, C., Newes, E., Schwab, A., & Vimmerstedt, L. (2014). *Overview of Aviation Fuel Markets for Biofuels Stakeholders* (No. NREL/TP-6A20-60254). National Renewable Energy Lab.(NREL), Golden, CO (United States).56.   Trimm, D. L. (2001). The regeneration or disposal of deactivated heterogeneous catalysts. *Applied Catalysis A: General*, *212*(1-2), 153-160.

Chapter 2

Experimental Methods

2.1 Introduction

The primary target of this study is to develop a fundamental understanding of the role of acid site in the γ-valerolactone (GVL) ring opening reaction to form pentenoic acid (PEA) and the following decarboxylation reaction to yield butene in homogenous and heterogeneous environments. This knowledge will guide us to improve catalyst performance in reactions over Brønsted acid sites (BAS) and Lewis acids sites (LAS). Therefore, a good description of physicochemical properties for the materials considered in this study is essential. Characterizations such as surface area, pore structure, acid site concentration, and acid site distribution are thoroughly defined, and their influences on the activity, selectivity, and stability of the reaction are further examined. N_2 physical adsorption, temperature programmed desorption (TPD), and Fourier-transform infrared (FTIR) are applied here to characterize catalysts prior to activity tests. Also, several reactors are designed for evaluating the performances of catalysts on GVL ring opening and following decarboxylation reactions in various environments.

2.2 Materials

γ-valerolactone (GVL, >98%, Aldrich) and trans-2-pentenoic acid (t2-PEA, Acros, 97%) were used as reactant and product in this study. Prior to use in the activity test, GVL and PEA were dried over silica gel (5% w/v, 12–24 mesh, Strem Chemicals). Type I water used in sample preparation was prepared in-house by sequential reverse osmosis, UV oxidation, and double deionization.

Sulfuric acid (95%) was obtained from Acros and served as acid catalysts (pH=1 solution) in the homogeneous catalysis study. Amorphous silica alumina (ASA) 3901, gamma alumina, two metal oxide catalysts (Titanium oxide and Zirconium dioxide), MFI structure zeolite samples of different

aluminum contents, Beta zeolite (BEA), Ferrierite structure zeolite (FER), Faujasite structure zeolite (FAU) and Mordenite structure zeolite (MOR) were used as acid catalysts in the heterogeneous catalysis study. All solid acid catalysts were obtained from commercial suppliers directly and provided in the acid or ammonium form. Therefore, catalysts were calcined in a downflow quartz U-cell placed in a furnace under zero-grade air (50 sccm) ex-situ before examining their activity in the reactor. The temperature of the furnace was ramped to 723K at a rate of 3 K/min and held for 4 hours with the thermal couple placed right above the catalysts beds.

2.3 Catalyst Characterizations

2.3.1 N_2 physical adsorption

The surface area of samples was determined by N_2 (99.999%, Airgas) adsorption at 77K in a surface area and porosity analyzer (Micromeritics ASAP 2020). Prior to N_2 dosing, approximately 100 mg of sample was degassed under vacuum for four hours at 623K. Total and micropore surface areas were calculated by Brunauer-Emmett-Teller (BET) and t-plot micropore analyses. Pore volumes were characterized by nitrogen cumulation at a relative pressure of 0.995. Pore sizes were estimated by Barrett-Joyner-Halenda (BJH) analysis of the desorption branch of N_2 uptake isotherms [1,2].

2.3.2 Acid sites titration

Based on the previous research, the Brønsted acid site and Lewis acid site play an essential role in the GVL ring opening and decarboxylation reaction [3]. Therefore, precise quantification of Brønsted acid site and Lewis acid site density on the solid acid catalysts is necessary for exploring the activity over different catalysts. Generally, Brønsted acid site concentration is determined by isopropylamine temperature programmed desorption experiment. For the materials with low

Brønsted acid site concentrations, such as γ-Al$_2$O$_3$, isopropylamine titration is not adequate to fully characterize the acidity on the surface. Thus, isopropanol temperature programmed desorption experiment is further introduced to estimate the materials abundant in the Lewis acid site.

Brønsted site densities were determined by isopropylamine (IPA, Acros, 99%) temperature programmed desorption (TPD). Typically, 60-80 mg of sample was added into a 1/2 inch quartz tube between two quartz wool (Grace) end plugs. The whole tube was further placed in an Omega furnace. The temperature of the furnace was regulated by a process controller (Love, series 16A) and monitored by a type K thermocouple (Omega). All samples were calcined under airflow (50 sccm). A ramping protocol that prevents the structural changes of the zeolites due to water evaporation was followed. The cell containing the samples was ramped to 373 (2 K/min) and was held at 373 K for 30 min. The cell was further heated at 393 K at the same rate and was held at 393 K for 30 min as well. Finally, the cell was ramped to 623 K (5 K/min) and was kept at that temperature for 300 min. The cell was subsequently cooled to 423K and purged in dry Helium flow (100 sccm) for more than 90 minutes. Catalysts were further dosed with isopropylamine in He flow. After saturation of IPA on the surface, physisorbed isopropylamine was removed by applying a high He flowrate (400 sccm) for at least 1 hour. The furnace was then ramped to 973K (10 K/min) under He, including 1% Ar serving as an internal standard. Chemisorbed isopropylamine was converted into propene and ammonia after ramping. During the whole process, a mass-selective residual gas detector (Stanford Instruments RGA 100) was used to track MS signals of isopropylamine (m/z=44), propylene (m/z=41), and Ar (m/z=40) in the effluent. Evolved propylene was used to calculate Brønsted site density, assuming that one molecule of isopropylamine adsorbs per Brønsted site [4,5].

The total acid site densities were determined by temperature programmed desorption (TPD) of ammonia or isopropanol in this study. Typically, 50-70 mg of sample were prepared into a ½ inch quartz tube with two quartz wool end plugs. The whole tube was future positioned in a high-temperature furnace (Omega) and connected to a gas flow manifold. A process controller (Love, series 16A) and a Type K thermocouple (Omega) were used to regulate and monitor the temperature. Prior to analysis, samples were calcined in situ at 723K for 4 hours under 50 sccm of air (Airgas, Ultra Zero). Subsequently, the samples were cooled to 373K and purged under 100 sccm of He flow dried over molecular sieves for more than 90 mins. After pretreatment, the samples were dosed with ammonia (1% ammonia and1% argon, Airgas) or isopropanol (7 torr), respectively. Once the surface was saturated with ammonia or isopropanol, the cell was purged under 400 sccm of He for one hour to eradicate the physically adsorbed probe molecule. The furnace was then ramped to 973K at 10K/min under Helium with 1.0% Ar serving as an internal standard to remove the chemisorbed compound. Throughout the analysis, a mass-selective residual gas detector (Stanford Instruments RGA 100) was applied to monitor MS signals of ammonia ($m/z = 16$), isopropanol ($m/z = 45$), propylene ($m/z = 41$) and Ar ($m/z = 40$) in the effluent gas continuously. Evolved ammonia or propene were used to estimate acid site density on the catalyst surface based on the assumption that one molecule of product is adsorbed and forms at one acid site only [6,7,8].

2.3.3 FTIR spectroscopy

Brønsted acid sites to Lewis acid sites ratio was determined using pyridine FTIR (Nicolet 6700 DTGS detector). 15-25 mg of catalysts were pressed into a 13mm pellet through a hydraulic press. The pellet was loaded on a self-designed cell placed in a built-in chamber, as illustrated in figure 2.1. Samples were calcined in-situ as the procedure described before. Subsequently, the cell was
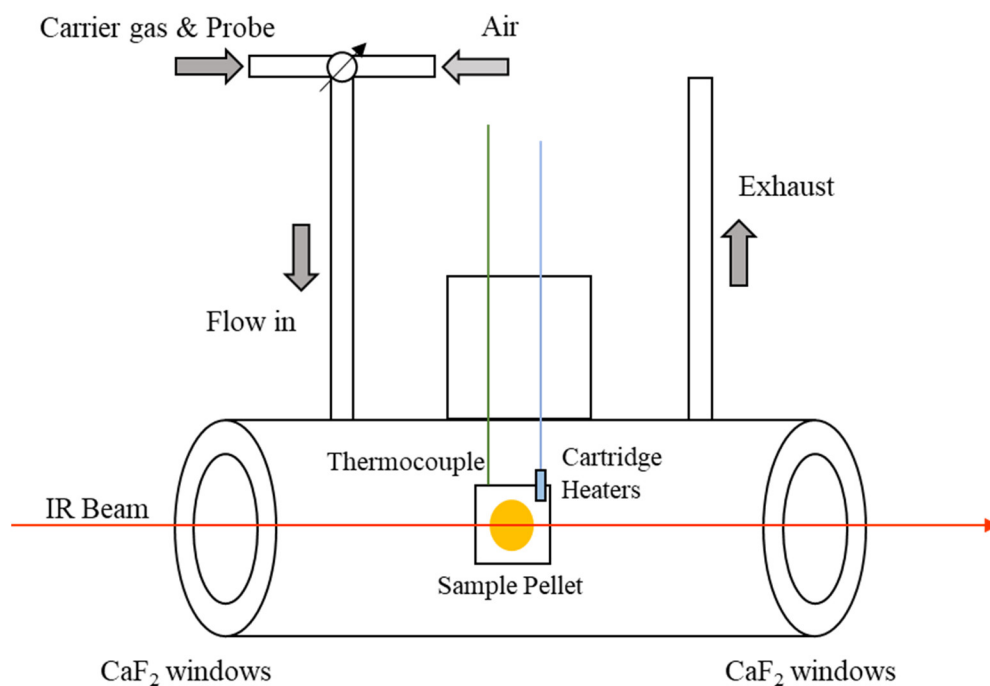
Figure 2.1: A schematic of home-built chamber for performing in-situ the FTIR experiments. The sample was adjusted to the height where IR beam can pass through the center of the pellet.

cooled to 423K and purged under a flow of 60 sccm of Helium. Helium was purified by a liquid nitrogen trap followed by a moisture trap. The pellet was then dosed with four torrs of pyridine (Sigma Aldrich, 99%). After the pellet was fully saturated with pyridine, the cell was purged under a He flow of 200 sccm at 423K to remove physically adsorbed pyridine. Spectra were collected at 423 K. and Brønsted to Lewis ratios were determined by the ratio of the integrated IR bands at 1545 cm^{-1} (pyridinium ion) and 1455 cm^{-1} (pyridine), respectively. The following equation 2.1 was applied to calculate Brønsted acid sites to Lewis acid sites ratio where C(BAS, LAS) represents the concentration of Brønsted acid sites and Lewis acid site and IA (B, L) represents the integrated absorbance of BAS or LAS [9,10].

$$\frac{C(BAS)}{C(LAS)} = \frac{1.88 * IA(B)}{1.42 * IA(L)}$$

(2.1)

2.4 Catalytic reactor setup

2.4.1 Biphase batch reactor

The interconversion between GVL and PEA in the liquid phase was examined in an autoclave batch reactor. Figure 2.2 demonstrates the system used for studying the kinetics of GVL ring opening in the pure aqueous phase. This setup was also used to test the productivity of GVL ring opening in the decane-water biphasic system. Reactant and catalysts were added to a 50 mL glass vessel along with a small magnetic stir bar to mix the liquid compound thoroughly. This vessel was further placed in a batch reactor made of 316 stainless steel. The temperature of the reactor was controlled by a temperature process controller (Love, series 16A) and measured by a type K thermocouple (Omega). A heating coil was used to heat up the reactor. The reaction temperature was recorded by another thermocouple placed in the liquid reactant. The pressure of the reactor was held was 200 psi before reaction using Helium as the inert gas. The whole system was placed on a heating stir plate. Samples can be collected through a Hastelloy tube and 4-port peek valve for every 30 minutes to track the product concentration changes. The concentrations of products were determined with a High-performance liquid chromatography through (Agilent Technology,
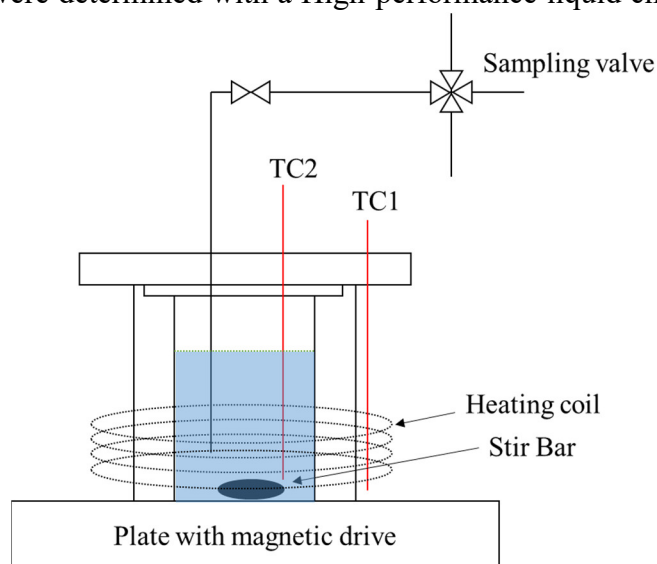
Figure 2.2: Setup of batch reactor for measuring kinetics of GVL ring opening in the liquid phase.

HPLC 1100 Series). The mole fractions of GVL and PEA in phase k are defined by the following equations:

$$X_{gvl,k} = \frac{n_{gvl,k}}{n_{gvl,k} + n_{solvent,k}} \tag{2.2}$$

$$X_{pea,k} = \frac{n_{pea,k}}{n_{pea,k} + n_{solvent,k}} \tag{2.3}$$

2.4.2 Flow reactor

In order to examine the catalytic activity of solid acids towards GVL ring opening to form PEA, packed bed reactors were applied in this study to analyze the chemistry of GVL ring opening in various reaction environments. A known mass of catalyst was diluted with sieved silica (40-90 um) and further loaded into a half-inch 316 stainless steel tube with two pieces of quartz wools placed on both sides to hold the bed. When measuring kinetics in the packed bed reactor, the GVL conversion is maintained under 5% at operation conditions to keep the reaction rate change in differential conditions, allowing us to quantify the reaction rate as a function of the mass of the
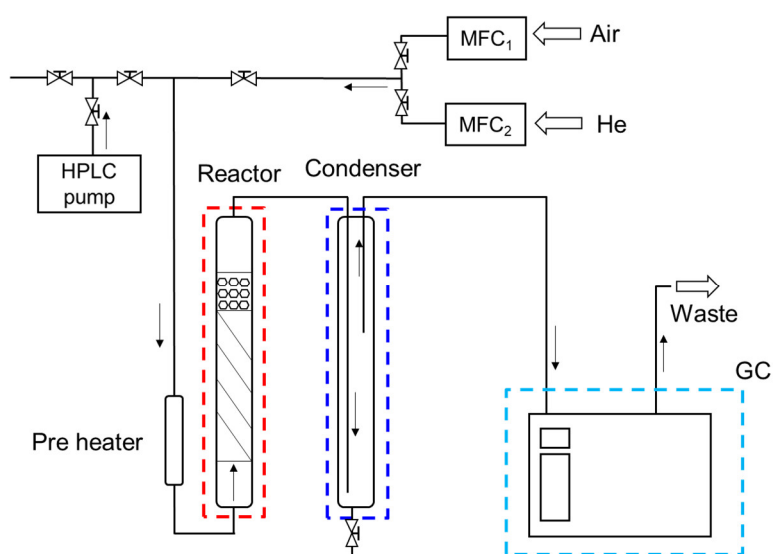
Figure 2.3: Setup of flow reactor for optimizing the yield of PEA from GVL ring opening in the aqueous environment.

catalyst bed. When optimizing the yield to PEA from GVL ring opening, catalysts performances were examined over a wide range of contact time and reaction temperatures.

Figure 2.3 and Figure 2.4 illustrate the flow system setup for testing catalysis activity in this study. For the aqueous setup, a pre-mixed aqueous GVL solution was introduced to the system through an HPLC pump. For the gas setup, pure liquid GVL was introduced to the system by using a programmable syringe pump (Cole-Parmer, model 110) and gasified in a homemade vaporizer in Helium flow. Gases are introduced into the system with digital mass flow controllers (Brooks). Detailed operation protocols are described in the corresponding chapter considering GVL ring opening chemistry investigated.
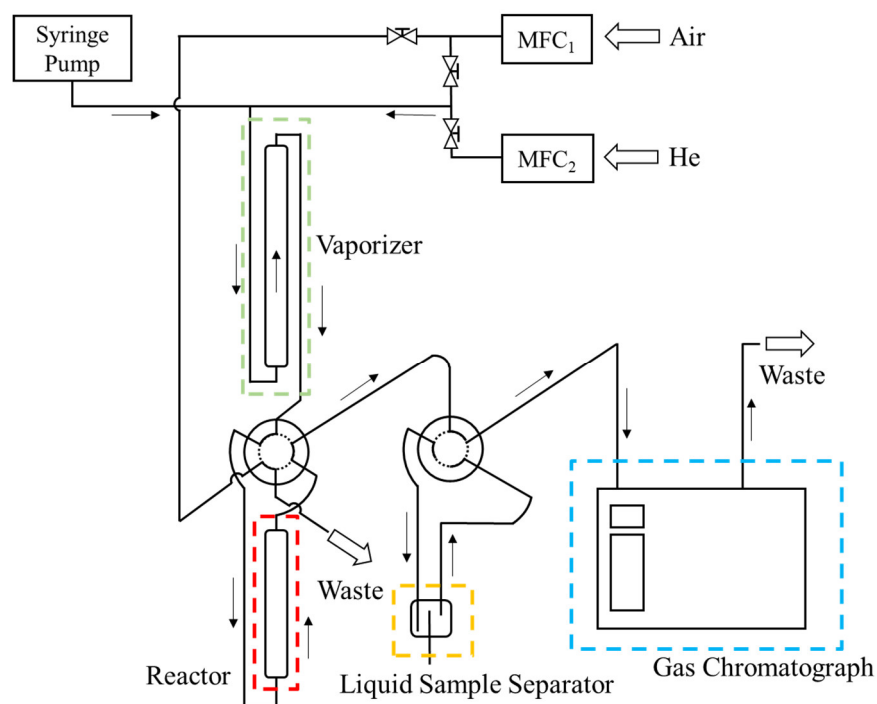
Figure 2.4: Setup of flow reactor for measuring kinetics of GVL ring opening in the gas phase.

2.5 References

1. Liu, J., Nan, Y., Huang, X., Bond, J. Q., & Tavlarides, L. L. (2018). Continuous esterification of oleic acid to ethyl oleate under sub/supercritical conditions over γ-Al2O3. *Applied Catalysis B: Environmental*, *232*, 155-163.

2. Zhang, J., Liu, J., Huang, X., Choi, S., Zhu, R., Tang, S., Bond, J. Q., & Tavlarides, L. L. (2020). Heterogeneous catalytic esterification of oleic acid under sub/supercritical methanol over γ-Al2O3. *Fuel*, *268*, 117359.

3. Bond, J. Q., Jungong, C. S., & Chatzidimitriou, A. (2016). Microkinetic analysis of ring opening and decarboxylation of γ-valerolactone over silica alumina. *Journal of Catalysis*, *344*, 640-656.

4. Farneth, W., & Gorte, R. (1995). Methods for characterizing zeolite acidity. *Chemical reviews*, *95*(3), 615-635.

5. Palkhiwala, A., & Gorte, R. (1999). Characterization of H-FER and H-TON using temperature-programmed desorption of alkylamines. *Catalysis letters*, *57*(1), 19-23.

6. Bates, S. A., Delgass, W. N., Ribeiro, F. H., Miller, J. T., & Gounder, R. (2014). Methods for NH3 titration of Brønsted acid sites in Cu-zeolites that catalyze the selective catalytic reduction of NOx with NH3. *Journal of Catalysis*, *312*, 26-36.

7. Srinivasan, S., Narayanan, C., Biaglow, A., Gorte, R., & Datye, A. (1995). The role of sodium and structure on the catalytic behavior of alumina: I. Isopropanol dehydration activity. *Applied Catalysis A: General*, *132*(2), 271-287.

8. Ji, Y., Lawal, A., Nyholm, A., Gorte, R. J., & Abdelrahman, O. A. (2020). Dehydra-decyclization of tetrahydrofurans to diene monomers over metal oxides. *Catalysis Science & Technology*, *10*(17), 5903-5912.

9. Emeis, C. (1993). Determination of integrated molar extinction coefficients for infrared absorption bands of pyridine adsorbed on solid acid catalysts. *Journal of Catalysis*, *141*(2), 347-354.

10. Zaker, A., Guerra, P., Wang, Y., Tompsett, G. A., Huang, X., Bond, J. Q., & Timko, M. T. (2018). Evidence of heterogeneous catalytic activity of ZSM-5 in supercritical water for dodecane cracking. *Catalysis Today*, *317*, 2-11.

Chapter 3

Thermodynamic and kinetic analysis of γ-valerolactone ring opening in multiphase reactors

3.1 Introduction

Biomass is considered a promising carbon alternative to control the increasing greenhouse gas emissions nowadays [1]. Recent studies have proven that there are potential markets for biofuel and bio-based platform chemicals [2,3]. In general, biomass upgrading is predicated upon the intermediate formation of functional platform chemicals, which can be converted as desired into a range of commodity products [4,5]. However, considering that biomass-derived chemicals always contain multiple functional groups, the selective preparation of target molecules is challenging due to the uncontrollable side reactions. One type of such productions is furfural. The furfural yields in a traditional preparation strategy are only 30% [6]. Another downside in biomass upgrading is the high cost and energy consumption during the separation process. In the bio-oil upgrading procedure, solvent extraction, distillation, and column separation are standard techniques involved in production extraction. However, the low efficiency in recovery of target chemicals and the high cost of the separation process made it difficult to scale up the biomass-based applications [7-9]. Thus, it is essential to develop efficient strategies to deliver a high yield of bio-based chemical production with feasible operation costs.

Among all possible solutions, the biphasic reactor has been received a lot of attention in recent years. The biomass-derived chemicals are commonly processed in an aqueous environment due to the instability of cellulose and hemicellulose content. Several studies have proven that by introducing an organic phase, not only the yield and selectivity of the target product can be improved, but also a sequential reaction can take place in the second phase to further produce more valuable chemicals [10-13]. For example, in a methyl isobutyl ketone (MIBK)-water binary system, the furfural yields obtained through xylose dehydration can be enhanced from 30% to 85%. Also, in a 2-sec-butylphenol -water binary system, the 5-hydroxymethylfurfural generated from fructose

dehydration can be improved up to 62% compared to the original 26% yield in water. Other organic solvents such as 2-methyltetrahydrofuran (MTHF) and tetrahydrofuran (THF) have also been used as an extraction phase for the production of biomass-based chemicals to manipulate the selectivity and yield of desired product [14].

Besides furan, GVL is another valuable platform chemical derived from biomass. It provides a spectrum of interesting opportunities for the production of biofuel and several significant industrial products [15-22]. Of interest here is the acid-catalyzed ring opening of GVL to form pentenoic acid (PEA) isomers, which are a family of bifunctional alkene-acids. PEA can be served as a precursor to produce nylon-66, biodiesel, jet fuel, and diesel fuel, rendering with a remarkable potential in commercial applications [21-23]. There are two challenges in the production of PEA. First, GVL ring opening is kinetically facile. It occurs readily in the gas phase over solid acids; however, thermodynamic limitations and secondary reactions make it generally difficult to recover pentenoic acids in good yield. Although GVL ring opening is entropically favorable, it is substantially endothermic, such that PEA yields are equilibrium limited below 20% at low temperatures. Raising operating temperatures will theoretically address this issue; unfortunately,
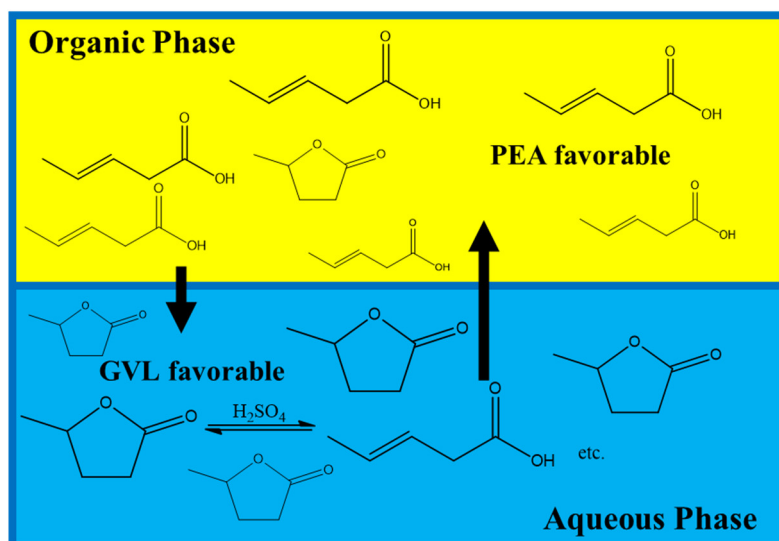
Figure 3.1: The proposed system for the ring opening of γ-valerolactone (GVL) to yield pentenoic acid (PEA) in a biphasic system.

increasing temperatures to the point where ring opening becomes thermodynamically favorable also makes undesired secondary reactions kinetically accessible. In particular, PEA isomers will undergo decarboxylation over solid acids, irreversibly forming butenes and carbon dioxide. Thus, there exists no gas-phase operating window where PEA isomers can be prepared in a good single pass yield [24].

In this study, our objective here is to propose a biphasic reactor catalyzed by homogeneous mineral acids to navigate thermodynamic and kinetic constraints and deliver high PEA yields. Figure 3.1 briefly illustration GVL and PEA distributed in the biphasic system. In the liquid phase system, the biphasic reactor has already shown its potential in the biomass upgrading process to improve the conversion and selectivity of several reactions considering its advantage of instantaneous product separation. Design a biphasic system rationally requires a detailed understanding of the kinetic and thermodynamic aspects of ring opening in a liquid phase. Furthermore, it requires an understanding of how GVL, protons, and PEA isomers partition behavior between water and various organic phases. A wide range of organic solvents is examined in this work to testify the affinity and separation ability towards GVL and PEA. Moreover, the activity coefficient is regressed by two parameters Margules thermodynamic model. Finally, based on the kinetic data of GVL ring opening and phase composition simulations at equilibrium, an activity-based model is acquired to probe the product distribution in any reaction conditions. The accessibility and best operation condition will be examined to maximize the PEA yield. The fundamental nature for the biphasic system to improve selectivity and yield will also be discussed.

3.2 Materials and Methods

3.2.1 Materials

γ-valerolactone (GVL, >98%, Sigma-Aldrich) and tran-2-pentenioc acid (PEA, 97%, Acros) were purified over molecular sieves ((5% w/v, 12–24 mesh, Strem Chemicals)) before use. Deionized water was applied in this study when preparing aqueous phase. The following reagents were used as supplied by manufacturers for the preparation of organic phase: n-Hexane (ACROS, 99+%), n-Octane (Alfa Aesar, 98+%), n-Decane (Alfa Aesar, 99%), n-Dodecane (Alfa Aesar, 99+%), 2-Pentanone (ACROS, 99%), 2-Hexanone (ACROS, 98%), 2-Octanone (ACROS, 99+%), 1-Hexanol (Alfa Aesar, 99%), 1-Octanol (ACROS, 99%), Phenol (Fisher, 90%), Diethyl ether (Alfa Aesar, 99%), methyl tert-Butyl ether (MTBE, ACROS, 99.0%), Ethylene glycol dimethyl ether(ACROS, 99+%), Heptanal dimethyl acetal (Alfa Aesar, 96%) , Ethyl acetate (ACROS, 99.5%), Methyl valerate (ACROS, 99%), 2,2,4-trimethylpentane (ACROS, Decalin (Fisher, Laboratory Grade), Toluene (Alfa Aesar, 99.5%), Benzene (SIGMA-ALDRICH, ≥99.7%), Acetone (Fisher, 99.5%). Helium (99.999%) was purchased from Airgas and used as inert gas in the reactor. Sulfuric acid (95%) was obtained from Acros and served as acid catalysts in this study.

3.2.2 Kinetics and thermodynamics of GVL ring opening in the aqueous phase

The interconversion between GVL and PEA was examined in an autoclave batch reactor. 30 mL of GVL (a concentration of 0.5 mol/L H_2SO_4, pH = 1) was added to a 100 mL glass vessel, which was placed in a batch reactor made of 316 stainless steel. Additionally, a sample with two mole percent water was also prepared. The temperature of the reactor was controlled by a temperature process controller (Love, series 16A). The temperature of the reaction was measured by a type K thermocouple (Omega) with its tips placed in the liquid solution. The kinetic data of GVL ring

opening was collected at multiple temperatures (453K, 473K and 493K). The pressure of the reactor was held was 200 psi before reaction using Helium as inert gas phase to maintain every compound in a liquid phase. Through a Hastelloy tube and 4-port peek valve, samples were taken from the reactor every 30 minutes and analyzed with a High-performance liquid chromatography (Agilent Technology, HPLC 1100 Series), until the product concentrations were no longer changing, indicating that the GVL opening reaction was near equilibrium. Resolution of GVL and PEA was achieved by elution method in HPLC through a reverse phase column (Agilent, C_{18} Zorbax). The mobile phase consisted of 0.05mM H_2SO_4 solution. GVL and PEA are quantified in a RID detector and UV detector. The response factors and retention time for GVL and PEA were determined by calibration of standard solutions.

3.2.3 Estimation of partition coefficient and resolution coefficient

The partition coefficient ($K_{d,j,k}$) was introduced to examine the solubility of GVL and PEA in different solvents [25-27]. The partition coefficient ($K_{d,j,k}$) for species "j" in solvent "k" was defined as the ratio between mole fraction of species j in organic phase k to its mole fraction in aqueous phase at equilibrium (Equation 3.1) where $X_{j,org}$ and $X_{j,aq}$ represented the mole fraction of species "j" in organic phase and aqueous phase, respectively. The resolution coefficient ($K_{R,k}$) was applied to describe the separation ability of GVL and PEA in different solvents. The resolution coefficient was defined as the ratio between partition coefficient of species j in organic phase to its partition coefficient in aqueous phase at equilibrium (Equation 3.2) where $K_{d,pea,k}$ and $K_{d,gvl,k}$ represented the partition coefficient of PEA in solvent k and partition coefficient of gvl in solvent k, respectively.

$$K_{d,j,k} = \frac{X_{j,org}}{X_{j,aq}} \tag{3.1}$$

$$K_{R,k} = \frac{K_{d,pea,k}}{K_{d,gvl,k}} \tag{3.2}$$

In order to measure the mole fraction of species j (GVL or PEA) in different solvents, a 0.15 mole fraction of partition compound (GVL or PEA) was prepared in water as aqueous phase in a 10 mL thick-wall glass vial (Chromatography Research Supplies). Subsequently, selected organic solvent was added into the vial under constant stirring at 80 rpm. The vessel was stirred for 24 hours to allow the biphasic system to reach complete equilibrium. Samples of each phase were collected and analyzed through a GC (Agilent Technology, GC 7890A) with an autosampler. The mass and density of both were also measured. Based on the partition coefficient measured, resolution coefficients for different solvents are further calculated. A wide range of solvents involving alkanes, alcohols, aromatics, ketones, and esters have been tested for comparing the resolution ability for GVL and PEA.

3.2.4 Activity coefficient Regression

Commonly, there are two types of models for regressing activity coefficient: (1) Empirical Models: Regular Solution Model, Van Laar Model and Margules Model. (2) Local Composition models: Wilson Model, Non-random Two Liquid (NRTL) model and Universal Quasi Chemical Model (UNIQUAC) [28-32]. While there are several options for regressing activity coefficients, parameters in some models are difficult to obtain for the compounds of interest here. Considering the unavailability of parameters and the purpose of our study, a two-parameter Margules activity model is introduced in this study.

With the intention of developing a feasible activity model for effective solvents, detailed studies in the water/hexane system and water/octane system were carried out over different partition compound (GVL or PEA) mole fractions ranging from 0 to 1 in its miscible phase. The total mass

$$mole\ ratio = \frac{X_{j,org}}{X_{j,aq}} \tag{3.3}$$

of organic phase and aqueous phase was fixed at 1.5g. For the estimation of GVL activity coefficient, different mass of GVL ranging from 0 to 1.5g (from pure water to pure GVL) were initially added into water under constantly stirring in a 10mL thick-wall glass vial (10ml, Chromatography Research Supplies). 1.5g selected organic solvent was further added into this GVL solution. For the estimation of PEA activity coefficient, different mass of PEA ranging from 0 to 1.5g (from pure solvent to pure PEA) were initially added into a selected solvent (hexane or octane) under constantly stirring in a 10mL thick-wall glass vial (10ml, Chromatography Research Supplies). 1.5g water was further added to this PEA solution. The vessel was stirred for 24 hours to allow the biphasic system to reach complete equilibrium. Samples of each phase were collected and analyzed through a GC (Agilent Technology, GC 7890A) with an autosampler. The mass and density of both were also measured. The ratio of aqueous and organic activity coefficients was calculated as the ratio of GVL equilibrium mole fraction in the organic phase to that in the aqueous phase (Equation 3.3).

3.2.5 Activity coefficient modeling and Biphasic Reactor modeling

In the activity coefficient modeling, the activity coefficient for GVL and PEA in hexane-water and octane-water biphasic systems were regressed from two-parameter Margules model based on the phase composition profile obtained before.

In the Biphasic Reactor modeling, it was assumed that GVL ring opening only occurred in the aqueous phase and was first order to GVL concentration. Monophase experiments were performed to collect the kinetic data for GVL ring opening to form PEA at temperatures ranging between 450 to 500K. These data were further used to estimate the kinetic parameters such as activation energy, enthalpy, and entropy. A value of 1 mole GVL was set as the initial reactant in the biphasic system. The mass transfer coefficient was set at 10^{11}, and we assumed that the mass transfer would not

influence the reaction rate in our conditions. A set of ordinary differential equations (ODEs) was correlated by the phase equilibrium at the interface of organic and aqueous phase. Both modeling processes are performed in Matlab.

3.3.6 Biphasic reactor testing

The interconversion between GVL and PEA in the biphasic system was carried out in an autoclave batch reactor. Different concentration of GVL-water solution with sulfuric acid (0.05 mol/L H_2SO_4, pH= 1) was prepared. 1g of this premixed solution was initially added to a 100 mL glass vessel as aqueous phase. Subsequently, 20g of hexane was added into the vessel as organic phase. The vessel was placed in a batch reactor made of 316 stainless steel and pressurized to 200 psi using Helium as inert gas phase to keep every compound in a liquid phase. The temperature of the reactor was controlled by a temperature process controller (Love, series 16A) and measured by a type K thermocouple (Omega). The reaction temperature was varied from 453K to 493K to track the temperature influence on the ring opening reaction. The reactor was constantly stirred for 24-72 hours to allow the reaction in the biphasic system to fully equilibrate. Finally, the reactor was cooled down to the ambient temperature and depressurized. The product concentrations in the aqueous phase were determined with High-performance liquid chromatography through (Agilent Technology, HPLC 1100 Series) while the product concentrations in the organic phase were determined through a GC (Agilent Technology, GC 7890A) with an autosampler.

3.3 Results and Discussions

3.3.1 Kinetics and thermodynamics of GVL ring opening in aqueous solution

Previous work proved that GVL ring opening was an entropically favorable but substantially endothermic reaction in the gas phase [33], such that PEA yields were below 10% due to equilibrium limitation at 493K. Kinetic and thermodynamic parameters are essential for describing GVL ring opening in the liquid phase. Figure 3.2 shows a time on stream PEA concentration profile for GVL ring opening at 453K, 473K, and 493K. The pea concentration increased dramatically in the initial 5 hours. After 20 hours, the PEA concentration became stable, which indicated that the GVL ring opening reaction was almost reaching equilibrium. However, this was still hard to predict the fully equilibrium composition for PEA and GVL at low temperature conditions. Considering that GVL ring opening reaction was a first order in GVL concentrations and also reversible in H_2SO_4 catalyzed environment [34], via applying the first order reversible model in the batch reactor for single reactant, equation 3.4 was derived to describe the GVL and PEA

$$C_{PEA} = \frac{K_{eq}}{K_{eq}+1} \cdot C_{GVL_0} \cdot (1 - e^{-k_a \cdot \left(1+\frac{1}{K_{eq}}\right) \cdot t}) \tag{3.4}$$
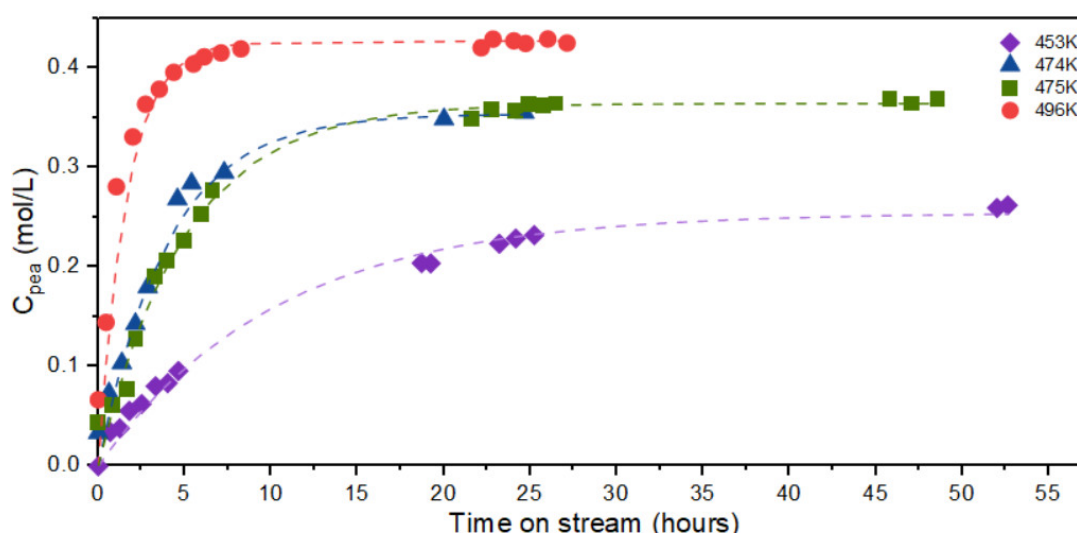
Figure 3.2: The PEA concentration time on stream profile of GVL ring opening reaction in the mono liquid phase at 453K, 474K and 496K (pH=1 H_2SO_4) and data fitting by first-order reversible biphasic reactor model.

concentration in different reaction environment as a function of time and initial GVL concentration (the derivation was shown in the supply information) . Here, K_{eq} represented the equilibrium constant of GVL ring opening at the reaction temperature. k_a referred to the forward rate constant of GVL ring opening. C_{GVL0} indicated the initial concentration of GVL. The simulation results were plotted in figure 1 as dash lines, which showed a good fitting for the PEA concentration profile. The activation energy for the forward reaction was determined by correlating Arrhenius Equation as the figure 3.3a showed. The enthalpy and entropy were determined by correlating Van`t Hoff Equation as shown in figure 3.3b. Table 3.1 shows the comparison between the experimental results for enthalpy, entropy and activation energy in the liquid phase against their predicted values based on gas phase results and condensation energy. According to previous research, in the gas phase, the enthalpy and entropy for GVL ring opening were 33.6 kJ/mol and 49.5 J/mol/K, respectively [24]. Considering the heats of vaporization for GVL and PEA during
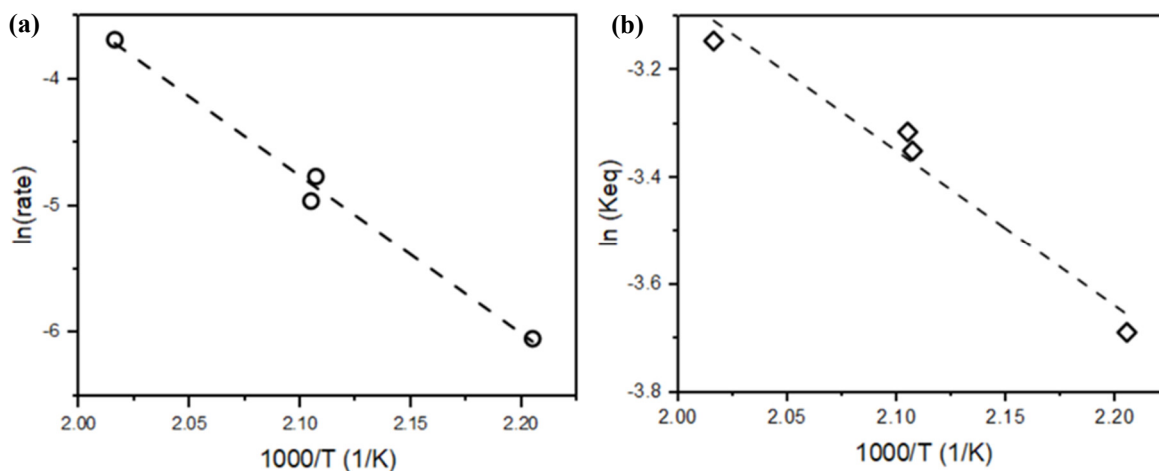
Figure 3.3: Arrhenius plot (a) and Van`t Hoff plot (b) of thermochemistry parameters regressed from experimentally measured distributions of PEA concentration profile.

	$\Delta H°$ (kJ mol^{-1})	$\Delta S°$ (J mol^{-1} K^{-1})	E_a (kJ mol^{-1})
Gas Phase	33.6	49.5	91 ± 29
ΔCondensation	-9.1	-23.1	
Liquid Phase Simulation Results	24.5	26.4	
Liquid Phase Experiment Results	24.1 ± 14.1	22.6 ± 14.1	103.5 ± 30.9

Table 3.1: Summary of kinetics and thermodynamics parameters of GVL ring opening in gas phase and liquid phase.

condensation [35-36], we estimated that the enthalpy and entropy should be around 24.5 and 26.4

in the liquid phase. Also, the activation energy for GVL ring opening was reported to be 91± 29

kJ/mol. Based on the experimental data in the liquid phase, enthalpy and entropy were 26.9 kJ/mol

and 22.6 J/mol/K, respectively, while the activation energy was 103± 30 kJ/mol. These results

showed that our experimental results regressed from the batch reactor model were highly

consistent with the estimation results. These suggested that GVL ring opening was more

enthalpically favorable but less entropically favorable comparing to the gas phase. Thus, between

a temperature range of 433K and 573K, the GVL ring opening was not thermodynamically

favorable, and the highest yield of PEA at equilibrium of 573K was only 5.1 %, which leaves a

large room for improvement of PEA yield by introducing the biphasic system.

3.3.2 Solvent Selection

Figure 3.4 summarizes the partition coefficient for GVL and PEA in 19 different organic solvents.

The exact phase compositions of these solvents are concluded in table S3.1. The partition

coefficient (K_d) captured the affinity of a specie for a given solvent. A large partition coefficient

implied high solubility for the dissolving species relative to water. A partition coefficient less than

1 indicates that the solvent has a low affinity for the given specie. A broad range of organic solvents

such as alkanes, alcohols, esters, ethers, ketones, aldehydes, and aromatic hydrocarbons have been

examined in this study. As shown in figure 3.4, overall, PEA had a high affinity in organic solvent

with a K_d above 50 while GVL showed relatively low affinity in organic solvent with a K_d below

25, indicating that organic phase is more favorable of dissolving PEA instead of GVL. Moreover,

high polarity alcohols and ketones like hexanol, octanol, heptanone and octane showed high

affinity both for GVL and PEA. However, low polarity alkanes and ethers like hexane, octane and

toluene only showed a high affinity for PEA rather than GVL. This may be explained by the
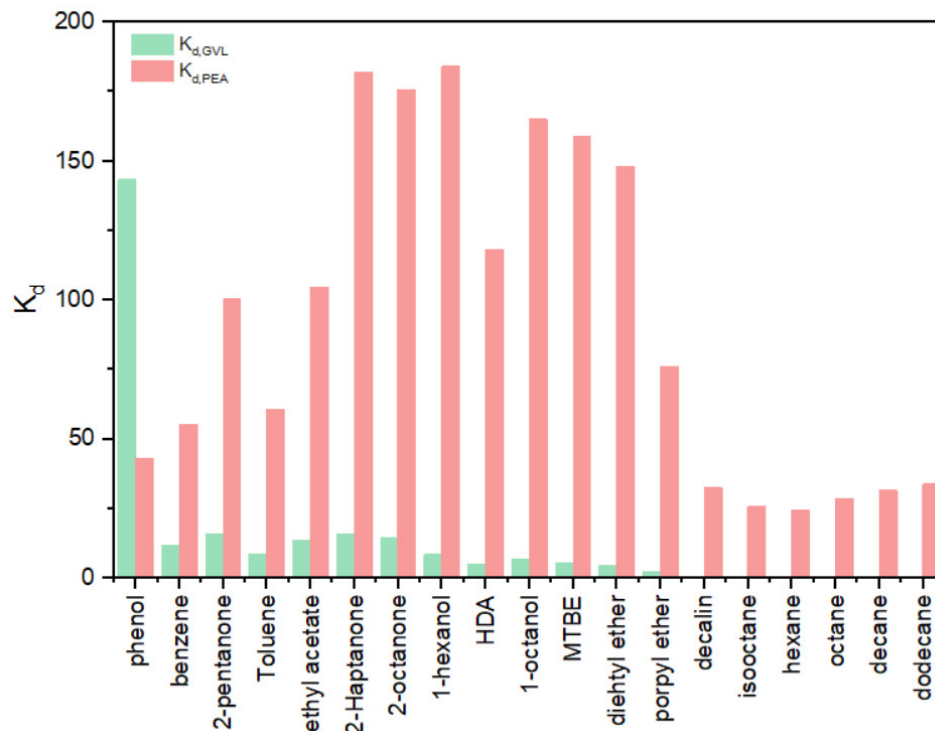
Figure 3.4: Summary of partition coefficient K_d for GVL and PEA in various water-organic systems.

difference in polarity of GVL and PEA. GVL was generally recognized as a polar aprotic solvent

and many studies have reported that GVL is effective for extracting lignin, which is comprised of

phenolic molecules [37-40]. This was consistent with our observation that GVL had the highest

partition coefficient in phenol and some relatively high partition coefficients in other polar solvents

such as esters or alcohols. In contrast, the hydrophilic feature of the carboxylic group in the PEA

molecule renders it with a high polarity, which resulted in a higher affinity for PEA than GVL in

a polar solvent. Also, the hydrophobic feature of the C=C double bond on the other end of PEA

rendered PEA some solubility in a non-polar solvent. Thus, these features render PEA a

significantly high solubility in both polar and non-polar solvents.

In order to further elucidate the ability for separating PEA and GVL in different solvent, the

resolution coefficients ($K_{R,k}$) for each solvent are listed in figure 3.5. A high resolution coefficient

($K_{R,k}$) indicated that the solvent k has a better ability for separating GVL and PEA. In a high K_R
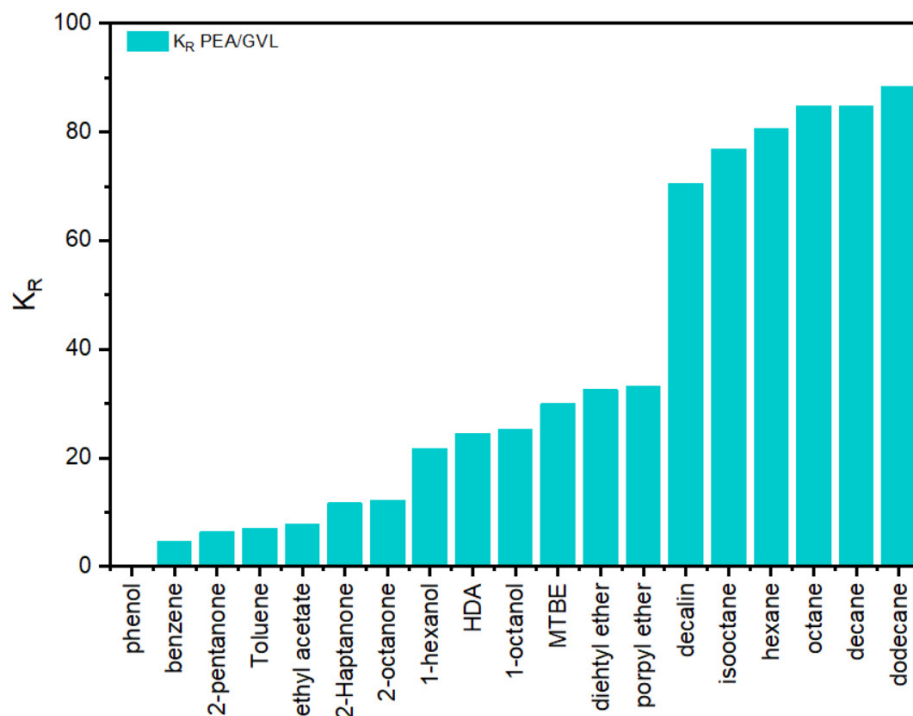
Figure 3.5: Summary of resolution coefficient K_R for GVL and PEA in various water-organic systems.

solvent, pea is more favorable to partition into organic phase while GVL stays in the aqueous phase.

Figure 3.5 shows that among all tested solvents, the resolution coefficients of alkanes such as hexane, octane and decalin were more than 60, suggesting that these alkanes had the best capacity for separating GVL and PEA into different phases, which can be considered as an ideal organic solvent in the biphasic system. Moreover, we observed that some ethers (propyl ether, diethyl ether, methyl tertiary-butyl ether (MTBE)) and alcohols (1-octanol, 1-hexanol) also presented a relatively high resolution coefficient around 30, which made them potential candidates as organic solvents. However, during further investigation, we found that MTBE showed some mutual solubility with water at equilibrium condition when the ratio of organic phase to aqueous phase was high. This may attribute to the hydrophilic property of ether. The same trend was observed in hexanol since its hydroxyl group was also hydrophilic. Last but not least, the resolution coefficients of ketones and acetates are less than 20, indicating that ketones and acetates are not appropriate for separate GVL and PEA. Overall, the results of partition coefficients and resolution

coefficients show that there is a significant difference in affinity for GVL and PEA among nineteen solvents. To achieve the goal of extracting PEA in the organic and leaving GVL in the aqueous phase, the ideal solvent for separation purposes is alkane considering its high affinity for PEA and low affinity for GVL.

3.3.3 Modeling phase equilibrium in biphasic system

Based on the result of the solvent study, hexane and octane were identified as potential organic solvents for resolve GVL and PEA in a biphasic system. The partitioning behaviors of GVL and PEA in water: hexane and water: decane systems are further examined over a wide range of compositions. Figure 3.6 illustrates the mole fraction of GVL and PEA in its miscible and immiscible phase in the biphasic system. We notice that among all tested biphasic compositions, the mole fraction of the partitioning compound in its immiscible phase is low. The mole fraction of GVL in aqueous is less than 5%, while the mole fraction of PEA in aqueous is less than 2%. This indicates that in all compositions, hexanes and octanes only show high affinity to PEA while water only showed high affinity to GVL. Also, the ratio of a specie in aqueous and organic activity coefficients can be expressed as a function of phase composition at equilibrium (Equation 3.6).
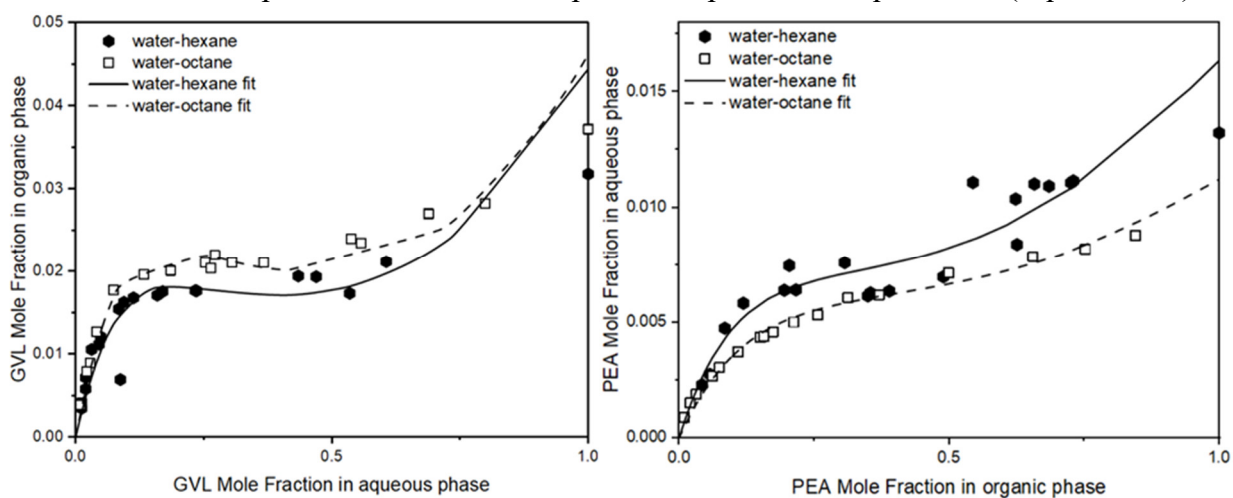
Figure 3.6. Phase composition of Water-Hexane (●) and Water-Octane (○) systems for GVL(a) and PEA(b). Solid line indicates Margules predictions for phase composition in Water-Hexane. Dashed lines indicate Margules Prediction for Water-Octane.

$$\frac{X_{j,org}}{X_{j,aq}} = \frac{\gamma_{j,aq}}{\gamma_{j,org}} \qquad\qquad 3.6$$

For the purpose of modeling activity coefficients in hexane/water system and octane/water system with different compositions, a two parameters Margules thermodynamic model is used in this study. This model is selected for its applicability to describe the phase equilibrium composition in a biphasic system [40]. It allows us to compute thermodynamic activities for partition compounds in either phase and to predict the equilibrium composition of the organic phase at any aqueous-phase composition in different biphasic reactors at equilibrium. The two-parameter Margules model is generally described by the following equation 3.7:

$$ln\gamma_{j,k} = (A_{12_{j,k}} + 2 \cdot (A_{21_{j,k}} - A_{12_{j,k}}) \cdot X_{j,k}) \cdot X^2_{k,k} \qquad\qquad 3.7$$

Here, $\gamma_{j,k}$ is the activity coefficient of compound j in solvent k, $X_{j,k}$ is the mole fraction of compound j in solvent k, $X_{k,k}$ is the mole fraction of solvent k in the solvent k. A_{12} and A_{21} represent two Margules parameters. Since the behavior of the partitioning compound is our primary interest in this study, the Margules activity model is only applied to regress activity coefficients for GVL and PEA in different phases. For example, in the hexane-water biphasic system, the Margules activity model for GVL and PEA can be expressed as equation 3.8-3.11.

Based on the phase equilibrium composition profile which we have previously obtained in water-hexane systems, the Margules parameters for GVL and PEA in this binary system can be regressed.

GVL-water-hexane system:

$$ln\gamma_{gvl,water} = (A_{12_{gvl,water}} + 2 \cdot (A_{21_{gvl,water}} - A_{12_{gvl,water}}) \cdot X_{gvl,water}) \cdot X^2_{water,water} \qquad 3.8$$

$$ln\gamma_{gvl,\ hexane} = (A_{12_{gvl,hexane}} + 2 \cdot (A_{21_{gvl,hexane}} - A_{12_{gvl,hexane}}) \cdot X_{gvl,hexane}) \cdot X^2_{hexane,hexane} \qquad 3.9$$

PEA-water-hexane system:

$$ln\gamma_{pea,hexane} = (A_{12_{pea,hexane}} + 2 \cdot (A_{21_{pea,hexane}} - A_{12_{pea,hexane}}) \cdot X_{pea,hexane}) \cdot X^2_{hexane} \qquad 3.10$$

$$ln\gamma_{pea,water} = (A_{12_{pea,water}} + 2 \cdot (A_{21_{pea,water}} - A_{12_{pea,water}}) \cdot X_{pea,water}) \cdot X^2_{water,water} \qquad 3.11$$

Since the mole fraction of miscible compound in its miscible phase (for example, GVL in water) ranged from infinite dilution to pure solute, this allowed us to regress both Margules parameters for a miscible compound in its miscible phase ($A_{12_{gvl,water}}$ and $A_{21_{gvl,water}}$ in the aqueous phase). However, the mole fraction of miscible compound in its immiscible phase (for example, GVL in hexane) was near zero, and the solvent mole fraction is approaches 100% accordingly. This leads to the results that only A_{12} parameter for the solute in its immiscible phase can be regressed (like $A_{12_{gvl,hexane}}$ in the organic phase). For describing the partition behavior in the immiscible phase, here, we assumed that the second Margules parameter for the solute in its immiscible phase ($A_{21_{gvl,hexane}}$) was 0. Based on this assumption, we manage to regress three Margules parameters in the binary system. These Margules parameters are listed in table 3.2. Figure3.6a and 3.6b show that both in aqueous and organic phase, the phase composition data can be satisfactorily correlated by the three-parameter Margules equations. This proved that this Margules model was sufficient to describe systems where the solute mostly stayed in its miscible phase like GVL in water and rarely appears in its miscible phase like GVL in alkanes. These regressed Margules parameters, along with previous kinetic and thermodynamic data of GVL ring opening reaction, were further applied in the simulation of reaction in the biphasic reactor.

Species	Solvent	A_{12}	A_{21}
GVL	Water	2.436	0.567
GVL	Hexane	3.743	0
GVL	Water	2.586	0.897
GVL	Octane	3.723	0
PEA	Water	4.395	0
PEA	Hexane	1.807	0.5855
PEA	Water	4.698	0
PEA	Octane	1.751	1.027

Table 3.1: Summary of Regressed Margules Parameters for GVL and PEA dissolved in Water-Hexane and Water-Octane binary systems.

3.3.4 Simulation ring opening reaction in biphasic system

In the non-ideal biphasic system, chemical potential, instead of concentration was the driving force behind the observation of different resolution ability, reaction kinetics and mass transfer [41]. Therefore, we develop an activity-based batch reactor model to predict the GVL ring opening in the biphasic system based on equations in table 3.3. This model is designed to describe not only GVL and PEA interconversion but also the partition behavior of GVL and PEA in each phase. The activity coefficient for specie j in solvent k can be calculated by equation 3.12 with the activity coefficient $\gamma_{j,k}$ obtained from the Margules model. In a non-equilibrated condition, the mass transfer on the interfacial boundary is described with equation 3.13. In this study, the mass transfer effect is not specially studied, and we assume the mass transfer is extremely fast and will not affect the reaction rate. The reaction rate is expressed as equation 3.14 considering that GVL ring opening reaction is a first order reversible reaction. The chemical equilibrium of GVL ring opening at a given temperature is estimated by equation 3.15. And finally, the phase equilibrium (equation 3.16) is determined by the condition that chemical potential of one specie is equal in each phase.

Phenomenon	Model	Equation
Activity for reacting species	$a_{j,k} = \gamma_{j,k} \cdot X_{j,k}$	3.12
Mass Transfer	$rm_j = k_c \cdot (a_{j,aq} - a_{j,org})$	3.13
Reaction Kinetics	$r_{j,k} = ka \cdot a_{j,k}$	3.14
Chemical Equilibra	$K_{eq} = \dfrac{a_{pea,k}}{a_{gvl,k}} = \exp(-\dfrac{\Delta H}{RT} + \dfrac{\Delta S}{T})$	3.15
Phase Equilibra	$a_{j,aq} = a_{j,org}$	3.16

Table 3.3: Summary of models describing thermodynamic and kinetic properties that driven by chemical potentials (thermodynamic activities) in the biphasic system.

Combining thermodynamic and kinetic parameters obtained from the GVL ring opening in an acidic aqueous environment with the Margules model for hexane-water biphasic system, a biphasic batch reactor comprised of hexane as organic phase and water as aqueous phase is simulated.
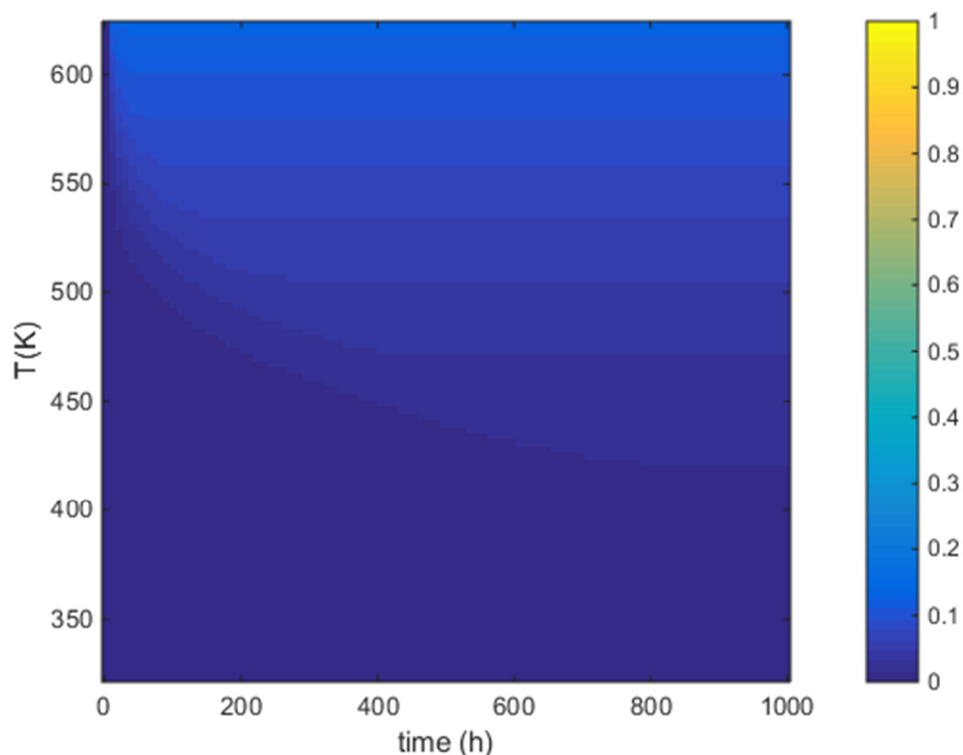
Figure 3.7: Simulated PEA yields obtained in a single aqueous phase batch reactor catalyzed by pH=1 H_2SO_4 as a function of reaction time and reaction temperature.

In figure 3.7, the ratio of organic phase to aqueous phase was set to $1x10^{-5}$, which approximated the reaction condition of mono aqueous phase condition. This figure shows that the total yield of PEA is limited by the highly unfavorable equilibrium of GVL ring opening in aqueous phase. Regardless of side reaction like PEA decarboxylation to butene and CO_2 decreasing PEA yield, the PEA yield is still less than 10% when the reaction temperature was at 600K in monophase condition. This again confirmed that under mono aqueous phase condition, realizing high PEA yield production was unpractical.
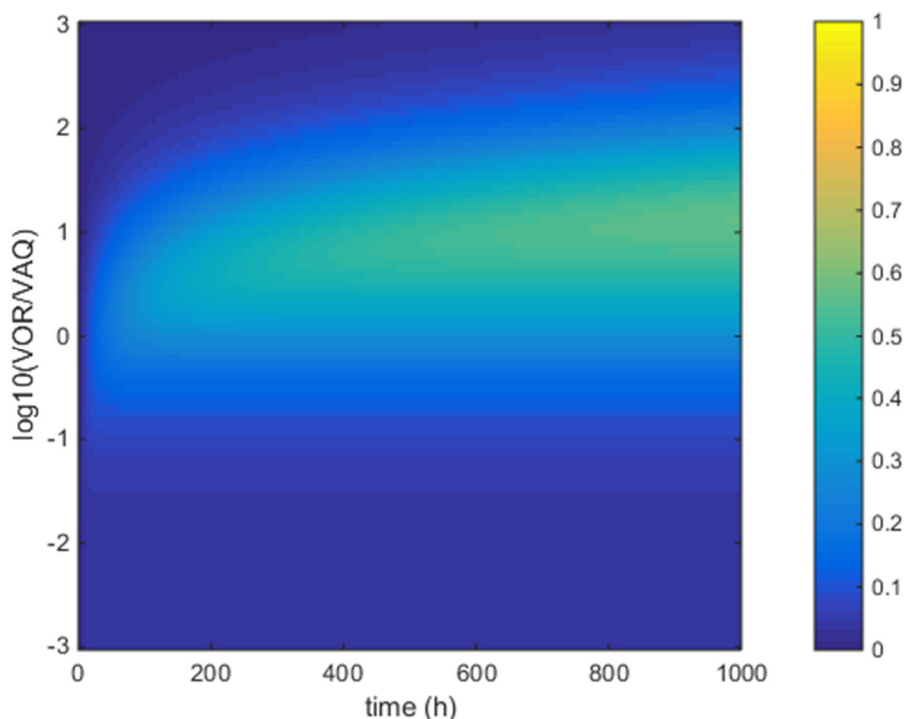
Figure 3.8: Simulated PEA yields obtained in a biphasic batch reactor comprised of an acidic aqueous phase (pH=1) and an organic extracting phase (hexane) as a function of reaction time and Solvent: Water molar ratio at 473K.

When setting the reaction temperature at 473K and introducing the organic phase as the extraction phase, the total PEA yield was improved as shown in figure 3.8. Based on the simulation result, when the organic: aqueous mole ratio was between 10:1 and 100:1, we observed that PEA yield reached 30% in initial 100 hours and could be further improved to 50% when the reaction time extended to 800 hours, which almost doubled the PEA yield in the monophase reactor. However, when the organic to aqueous ratio increased to from 100:1 to 1000:1, the PEA yield decreased to from 50% to 10%.

Figure 3.9 illustrates the impacts of both reaction temperature and organic: aqueous phase ratio on the PEA yields at equilibrium condition. It showed that when reaction time was extended long enough for the GVL ring opening to reach fully equilibrium, in a biphasic where organic to aqueous mole ratio is beyond 100:1 and reaction temperature is beyond 543K, optimized PEA yields of 80% can be achieved. Considering the side reactions at high temperature, realistic solvent

volume requirements and practical reaction time, if one operates the reactor around 473K in a 10:1

NS:NA ratio environment, PEA yields are still able to reach 40% at fully equilibrated condition,

which was acceptable and worth for further application of PEA.
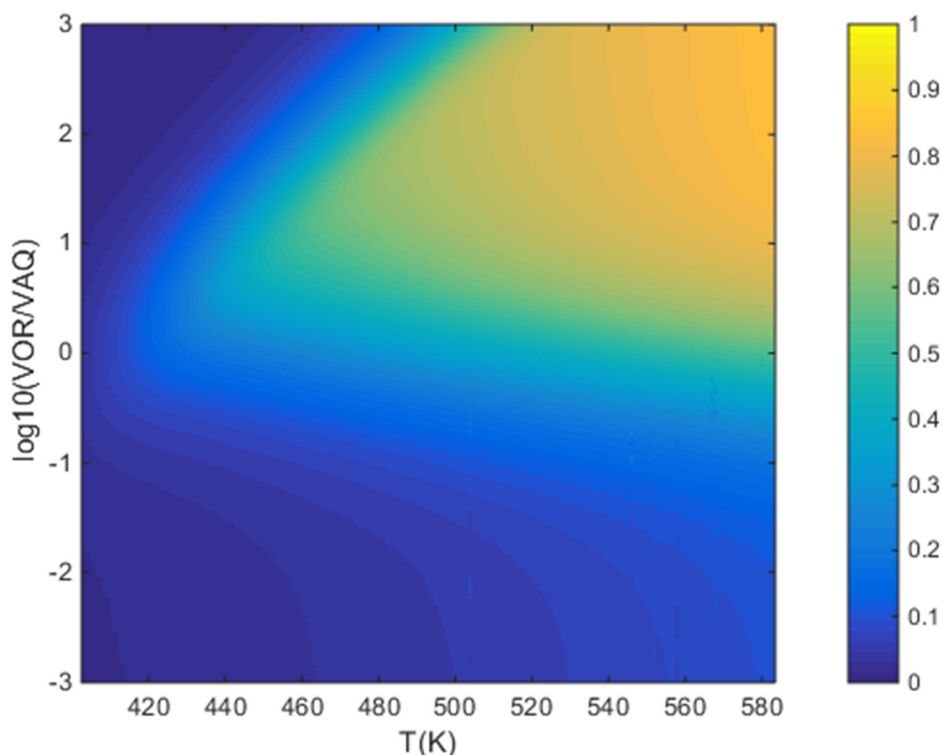
Figure 3.9: Simulated PEA yields obtained in a biphasic batch reactor comprised of an acidic aqueous phase (pH=1) and an organic extracting phase (hexane). Simulations were performed as a function of reaction temperature and Solvent: Water molar ratio for a sufficient time to reach phase and chemical equilibrium.

The reason why the PEA yield in a biphasic reactor was higher than that in a monophase reactor

at certain organic: aqueous mole ratio can be attributed to two factors. Typically, in an aqueous

phase environment, the PEA had high chemical potential since it had low solubility in water, which

hindered the GVL ring opening and limited PEA yield. On the contrary, in a biphasic system, the

selected organic solvent had a higher affinity for PEA, which can reduce the chemical potential of

PEA relative to GVL. These facilitated the formation of PEA and increased the PEA selectivity in

the whole binary system. Moreover, the introduction of organic phase solvent allowed a more in-

time extraction of PEA from the aqueous phase. In this way, the chemical potential of PEA

remained low in the aqueous phase during the whole reaction progress. Thus, the ring opening of GVL was not limited by the thermal equilibrium and GVL could continuously be converted into PEA. However, one downside of increasing organic: aqueous mole ratio was that reaction rate would decrease due to the reduction of GVL chemical potential in aqueous phase. This could increase the reaction time required to reach equilibrium condition. Therefore, in a biphasic system with an organic: aqueous mole ratio higher than 100:1, the time required to achieve the same PEA yields became significantly longer.

3.3.5 Experiment verification in biphasic system

Several experiments were performed in the decane: water biphasic system to verify the simulation results we had previously obtained. The reason why we choose decane instead of hexane and octane is than the low vapor pressure and low density of hexane and octane makes it unreliable to keep them in liquid phase under reaction condition (near 573K, 300 psi). Decane was a more
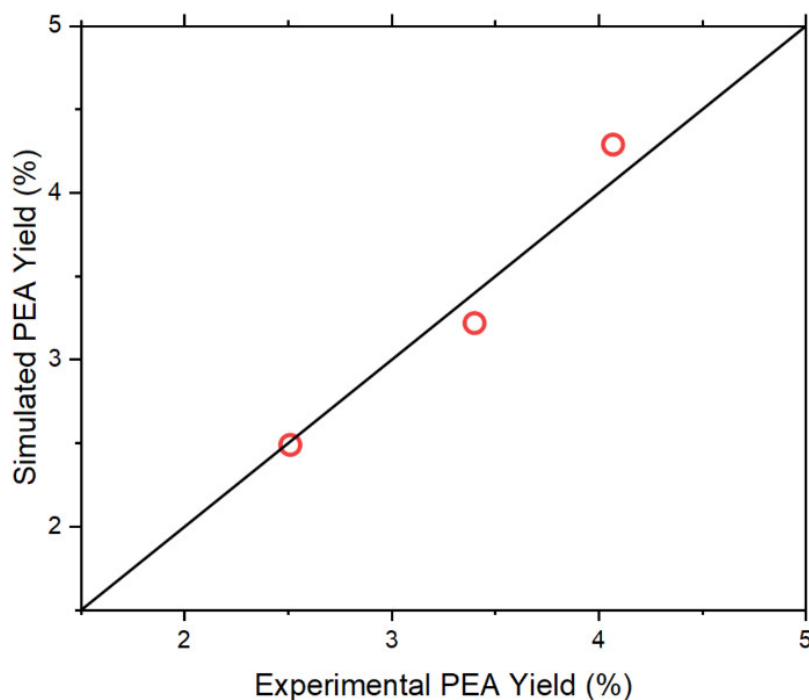
Figure 3.10: Parity Plot for GVL ring opening reaction in single phase condition at 453K, 473K and 496K with initial $C_{gvl} = 10.45$ mol/L.

practical solvent to maintain biphasic condition near operating temperature and pressure. Also, we notice the deference in the distribution of PEA in hexane and octane is negligible (figure 3.6). This indicates that the length of carbon in alkanes may not have a significant influence on the separation ability of GVL and PEA and Margules parameters for straight-chain alkanes were similar, the Margules parameters for decane was set the same as octane`s in the simulation. The yield of PEA was predicted by the biphasic model we described before. Based on the parity plot of figure 3.10, we can see that the model predictions agreed with the experimental results in the biphasic conditions where organic: aqueous mole ratio is low. From figure 3.11, we observed that by increasing the organic phase: aqueous mole ratio from 0 to 0.53, the PEA yields improved from 0.7% to 3.95% at 513K in 21hours. The PEA yield can be further enhanced to 10% when the increasing the organic phase: aqueous phase ratio was increased to 1.08. This result indicated a 10-
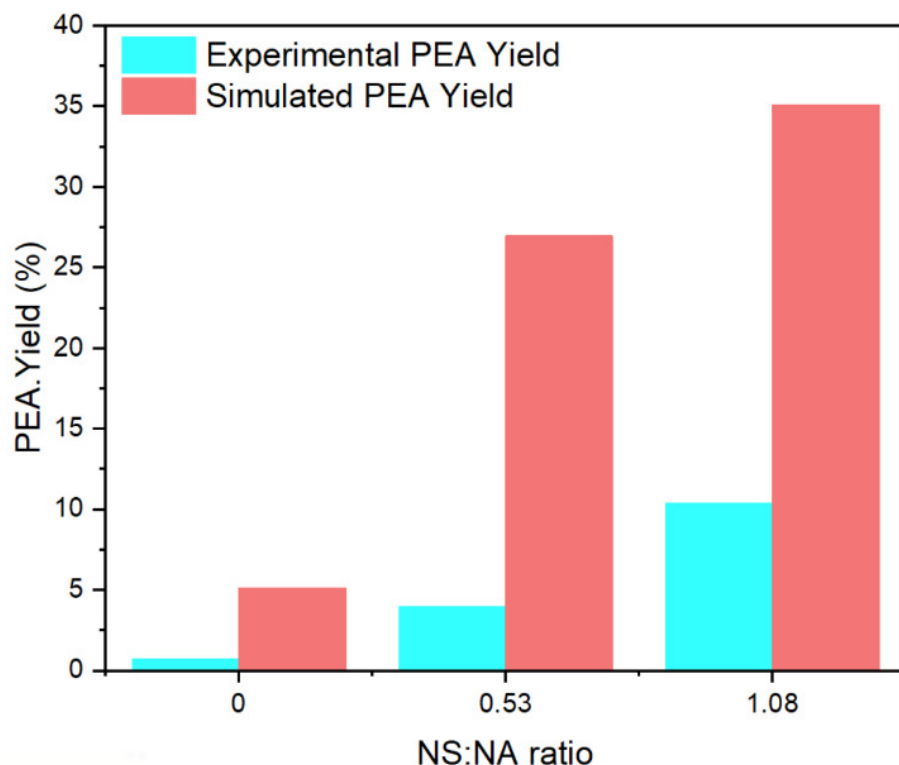
Figure 3.11: Experimental and Simulated GVL ring opening reaction in a decane water system at different NS:NA ratio with initial $C_{gvl} = 0.504$ mol/L.

fold enhancement in PEA yields in hexane: water system compared to the single aqueous phase result. However, the model predicted higher PEA yields in these conditions where the maximum PEA yield can reach 40% in our reaction condition. Several factors may contribute to the disagreements between the actual experiment and model simulations. First, the current experiments still cannot meet the least NS: NA requirement to witness a significant increase in PEA yield. For realizing an ideal hexane/water biphasic environment with a ratio of NS: NA=10, the volume of hexane required was 109 times more than that of water. However, the volume of our cylinder reactor was only 50 mL and the highest NS: NA ratio which we can reach is almost 1. This is far away from the ideal reaction condition for biphasic system to work. Second, side reactions may decrease the PEA yields. According to our experiments, some insoluble blacked residues were formed and 10% of carbon lost in the blank experiment of decane/water system was observed. This may attribute to the polymerization of PEA isomers at high temperature environments [42]. Third, the activity coefficients could be sensitive to temperature and pressure, whereas our model assumes that activity coefficients determined at ambient temperature remain constant between 453 to 493K. A previous study reported that the activity coefficient might have 10% change when the temperature of the solvents increased by 10 K [43]. Fourth, the solubility between alkanes and water may be changed at high temperatures. Usually, the alkanes have low solubility in water. Some report has pointed out that the mutual solubilities of hydrocarbons and water would increase as the temperature rose up [44]. Moreover, the mass transfer may influence the time it takes for the biphasic system to reach thermal equilibrium. Meanwhile, in our simulation, we assume that the mass transfer will not affect the reaction rate. This assumption can add uncertainty to our results. The typical mass transfer coefficient is around 10^{-4} [45]. If we use this number instead of 10^{11} in our previous simulation, the predicted PEA yield will drop to 12% at the

condition where the organic phase: aqueous phase ratio was 1.08. Finally, in the biphasic system, the affinity for PEA instead of separation ability between GVL and PEA may play a significant role in enhancing the yield and selectivity of the reaction. In the binary system, introducing a second phase that has a high affinity for PEA can also lead to a decrease in the total potential energy in the system. We have previously found that ketones and alcohols have a relatively high affinity for PEA. However, these organic compounds cannot be used as organic phases due to the side reactions such as condensation and esterification. The high reactivity between reactant and solvent makes it unreliable to examine such a biphasic system.

3.4 Conclusion

Solution thermodynamics and kinetics are significant in understanding species behavior between multiphase systems. In this study, we have initially estimated the enthalpy, entropy and barrier for GVL ring opening reaction in the liquid phase, which is consistent with simulation results based on the previously obtained gas phase data. Moreover, the solubility and separation ability for GVL and PEA in more than nineteen solvents are studied, and alkane is identified as the potential organic phase in biphasic system considering its best separation capability. A two-parameter Margules Model was further introduced to measure the activity coefficient in the GVL-PEA-water-hexane system and GVL-PEA-water-octane system. This model managed to describe the phase composition in the biphasic system at the ambient temperature and can be considered as a feasible approach to measure the activity coefficient among different solvent systems. After that, an activity-based batch reactor model is developed for predicting the product yield, component distribution in multiphase system and their relationship with temperature and solvent composition. The simulation results indicated that in a biphasic system with an organic phase: aqueous mole ratio more than 2, one can improve PEA yields from less than 10% to more than 70% at 473K at equilibrium condition. Several experiments are performed to verify the actual reaction condition. However, we found that this model is only able to predict the biphasic reactor with low organic phase: aqueous mole ratio. Limited by the sensitivity of activity coefficient to temperature, the high reactivity of PEA, and uncontrollable side reactions at high temperatures, the model failed to predict the PEA yields in real reaction environments. Even though, the idea of increasing total GVL conversion by decreasing PEA potential during GVL ring opening progress, thus breaking the equilibrium limitation, is still valuable for further development of GVL-based conversion technology.

3.5 Supplementary Information

3.5.1 Derivation of PEA concentration in a batch reactor as a function of GVL initial concentration and reaction time

Given that GVL is a first-order reversible reaction in the liquid phase catalyzed by sulfuric acid, we can simplify the reaction as the following equations S3.1:

$$GVL \underset{\text{k-a}}{\overset{\text{ka}}{\rightleftharpoons}} PEA \qquad\qquad \text{S3.1}$$

Where k_a stands for forward reaction rate constant and k_{-a} stands for backward reaction rate constant. The reaction rate, material balances for GVL and PEA can be expressed by equation S3.2, S3.3 and S3.4.

$$r = k_a \cdot C_{GVL} - k_{-a} \cdot C_{PEA} \qquad\qquad \text{S3.2}$$

$$\frac{dC_{GVL}}{dt} = -r = -k_a \cdot C_{GVL} + k_{-a} \cdot C_{PEA} \qquad\qquad \text{S3.3}$$

$$\frac{dC_{PEA}}{dt} = r = +k_a \cdot C_{GVL} - k_{-a} \cdot C_{PEA} \qquad\qquad \text{S3.4}$$

By substitution the mass balance equation: $C_{GVL,0} + C_{PEA,0} = C_{GVL} + C_{PEA}$,where $C_{GVL,0}$ and $C_{PEA,0}$ represent the initial concentration for GVL and PEA in the batch rector, into material balance equation S3.4 and rearrange the result, we can obtain a nonhomogeneous, linear differential equation S3.5 as function of C_{PEA} and reaction time t.

$$\frac{dC_{PEA}}{dt} + (k_a + k_{-a}) \cdot C_{PEA} = k_a \cdot (C_{GVL} + C_{PEA}) \qquad\qquad \text{S3.5}$$

The solution of equation S3.5 can be expressed as a sum of particular solution at where $\frac{dC_{PEA}}{dt} = 0$ and homogeneous solution at where $k_a \cdot (C_{GVL} + C_{PEA}) = 0$. These two solutions can be written as equation S3.6 and S3.7.

$$C_{PEA,p} = \frac{k_a}{k_a + k_{-a}} \cdot (C_{GVL,0} + C_{PEA,0}) \qquad \text{S3.6}$$

$$C_{PEA,h} = a \cdot e^{-(k_a+k_{-a})\cdot t} \qquad \text{S3.7}$$

Therefore, the overall expression for PEA concentration can be demonstrated as the equation S3.8:

$$C_{PEA} = a \cdot e^{-(k_a+k_{-a})\cdot t} + \frac{k_a}{k_a + k_{-a}} \cdot (C_{GVL,0} + C_{PEA,0}) \qquad \text{S3.8}$$

By solving a initial condition where t=0, we can obtain the equation S3.9 as a general expression for PEA concentration in a reaction at any given initial composition and reaction time.

$$C_{PEA} = C_{PEA,0} \cdot e^{-(k_a+k_{-a})\cdot t} + \frac{k_a}{k_a + k_{-a}} \cdot (C_{GVL,0} + C_{PEA,0}) \cdot (1 - e^{-(k_a+k_{-a})\cdot t}) \qquad \text{S3.9}$$

In this study, since $C_{PEA,0} = 0$ and the equilibrium constant K_{eq} can be expressed as $K_{eq} = \frac{k_a}{k_{-a}}$, the equation S3.9 can be simplified into equation S3.10, also known as equation 3.4.

$$C_{PEA} = \frac{K_{eq}}{K_{eq} + 1} \cdot C_{GVL_0} \cdot (1 - e^{-k_a \cdot \left(1 + \frac{1}{K_{eq}}\right) \cdot t}) \qquad \text{S3.10}$$

3.5.2 The summary of solvent properties, partition coefficients and resolution coefficients

Table S3.1 summarizes the phase composition and distribution coefficients for GVL and PEA for all nineteen solvents mentioned in the paper.

Entry	Solvent	$X_{GVL,aq}$	$X_{GVL,org}$	Kd_{GVL}	$X_{PEA,aq}$	$X_{PEA,org}$	Kd_{PEA}	K_R
1	phenol	6.15E-04	8.80E-02	143.30	2.21E-02	9.52E-01	43.18	0.30
2	benzene	5.27E-03	6.23E-02	11.83	1.42E-03	7.83E-02	55.26	4.67
3	2-pentanone	4.38E-03	6.94E-02	15.85	7.42E-04	7.43E-02	100.55	6.35
4	Toluene	7.00E-03	6.12E-02	8.64	1.45E-03	8.81E-02	60.75	7.03
5	ethyl acetate	5.34E-03	7.20E-02	13.49	8.90E-04	9.31E-02	104.58	7.75
6	2-Haptanone	5.41E-03	8.54E-02	15.60	5.94E-04	1.07E-01	181.98	11.66
7	2-octanone	6.44E-03	9.08E-02	14.39	6.83E-04	1.19E-01	175.69	12.21
8	1-hexanol	7.92E-03	6.71E-02	8.47	5.17E-04	9.46E-02	184.08	21.73
9	HDA	1.28E-02	6.17E-02	4.83	1.20E-03	1.42E-01	118.10	24.47
10	1-octanol	1.05E-02	6.89E-02	6.55	7.13E-04	1.18E-01	165.12	25.20
11	MTBE	1.09E-02	5.71E-02	5.30	5.97E-04	9.26E-02	159.03	29.98
12	diethyl ether	8.40E-03	3.73E-02	4.56	5.61E-04	8.26E-02	148.13	32.52
13	propyl ether	1.45E-02	3.32E-02	2.29	1.28E-03	9.64E-02	75.83	33.11
14	decalin	1.83E-02	8.20E-03	0.46	3.36E-03	1.08E-01	32.39	70.51
15	isooctane	1.95E-02	6.52E-03	0.33	3.60E-03	9.07E-02	25.68	76.91
16	hexane	1.87E-02	5.69E-03	0.30	3.06E-03	7.53E-02	24.59	80.68
17	octane	1.88E-02	6.27E-03	0.33	3.27E-03	9.26E-02	28.36	84.81
18	decane	2.02E-02	7.53E-03	0.37	3.73E-03	1.18E-01	31.60	84.81
19	dodecane	2.10E-02	7.74E-03	0.38	3.64E-03	1.22E-01	33.80	88.32

Table S3.1: Summary of phase composition, $K_{d,GVL}$, $K_{d,PEA}$ and K_R for all tested solvent in this study.

3.6 References

1. Bhattacharya, M., Paramati, S. R., Ozturk, I., & Bhattacharya, S. (2016). The effect of renewable energy consumption on economic growth: Evidence from top 38 countries. *Applied Energy*, *162*, 733-741.
2. Perlack, R. D., Eaton, L. M., Turhollow Jr, A. F., Langholtz, M. H., Brandt, C. C., Downing, M. E., ... & Lightle, D. (2011). US billion-ton update: biomass supply for a bioenergy and bioproducts industry.
3. Rogers, J. N., Stokes, B., Dunn, J., Cai, H., Wu, M., Haq, Z., & Baumes, H. (2017). An assessment of the potential products and economic and environmental impacts resulting from a billion ton bioeconomy. *Biofuels, Bioproducts and Biorefining*, *11*(1), 110-128.
4. Perego, C., & Bianchi, D. (2010). Biomass upgrading through acid–base catalysis. *Chemical Engineering Journal*, *161*(3), 314-322.
5. Bridgwater, A. V. (2012). Review of fast pyrolysis of biomass and product upgrading. *Biomass and bioenergy*, *38*, 68-94.
6. Mansilla, H. D., Baeza, J., Urzua, S., Maturana, G., Villaseñor, J., & Durán, N. (1998). Acid-catalysed hydrolysis of rice hull: evaluation of furfural production. *Bioresource technology*, *66*(3), 189-193.
7. Gouveia, L., Graça, S., Sousa, C., Ambrosano, L., Ribeiro, B., Botrel, E. P., ... & Silva, C. M. (2016). Microalgae biomass production using wastewater: treatment and costs: scale-up considerations. *Algal Research*, *16*, 167-176.
8. Liu, Z., Si, B., Li, J., He, J., Zhang, C., Lu, Y., ... & Xing, X. H. (2018). Bioprocess engineering for biohythane production from low-grade waste biomass: technical challenges towards scale up. *Current opinion in biotechnology*, *50*, 25-31.
9. Lee, J. W., Houtman, C. J., Kim, H. Y., Choi, I. G., & Jeffries, T. W. (2011). Scale-up study of oxalic acid pretreatment of agricultural lignocellulosic biomass for the production of bioethanol. *Bioresource technology*, *102*(16), 7451-7456.
10. Kaur, I., & Ni, Y. (2015). A process to produce furfural and acetic acid from pre-hydrolysis liquor of kraft based dissolving pulp process. *Separation and Purification Technology*, *146*, 121-126.
11. Xin, J. Y., Li, S. B., Xu, Y., & Wang, L. L. (2000). Enzymatic resolution of (S)-(+)-Naproxen in a trapped aqueous–organic solvent biphase continuous reactor. *Biotechnology and bioengineering*, *68*(1), 78-83.
12. Weingarten, R., Cho, J., Conner Jr, W. C., & Huber, G. W. (2010). Kinetics of furfural production by dehydration of xylose in a biphasic reactor with microwave heating. *Green Chemistry*, *12*(8), 1423-1429.
13. Kaur, I., & Ni, Y. (2015). A process to produce furfural and acetic acid from pre-hydrolysis liquor of kraft based dissolving pulp process. *Separation and Purification Technology*, *146*, 121-126.
14. Chheda, J. N., Román-Leshkov, Y., & Dumesic, J. A. (2007). Production of 5-hydroxymethylfurfural and furfural by dehydration of biomass-derived mono-and poly-saccharides. *Green Chemistry*, *9*(4), 342-350.

15. Ravikumar, V. R., Schröder, A., Köhler, S., Çetinel, F. A., Schmitt, M., Kondrakov, A., ... & Schmidt-Hansberg, B. (2021). γ-Valerolactone: An Alternative Solvent for Manufacturing of Lithium-Ion Battery Electrodes. *ACS Applied Energy Materials*, *4*(1), 696-703.

16. Obregón, I., Gandarias, I., Ocio, A., García-García, I., de Eulate, N. A., & Arias, P. L. (2017). Structure-activity relationships of Ni-Cu/Al2O3 catalysts for γ-valerolactone conversion to 2-methyltetrahydrofuran. *Applied Catalysis B: Environmental*, *210*, 328-341.

17. Du, X. L., Bi, Q. Y., Liu, Y. M., Cao, Y., He, H. Y., & Fan, K. N. (2012). Tunable copper-catalyzed chemoselective hydrogenolysis of biomass-derived γ-valerolactone into 1, 4-pentanediol or 2-methyltetrahydrofuran. *Green Chemistry*, *14*(4), 935-939.

18. Bond, J. Q., Alonso, D. M., Wang, D., West, R. M., & Dumesic, J. A. (2010). Integrated catalytic conversion of γ-valerolactone to liquid alkenes for transportation fuels. *Science*, *327*(5969), 1110-1114.

19. Serrano-Ruiz, J. C., Braden, D. J., West, R. M., & Dumesic, J. A. (2010). Conversion of cellulose to hydrocarbon fuels by progressive removal of oxygen. *Applied Catalysis B: Environmental*, *100*(1-2), 184-189.

20. Alonso, D. M., Bond, J. Q., Serrano-Ruiz, J. C., & Dumesic, J. A. (2010). Production of liquid hydrocarbon transportation fuels by oligomerization of biomass-derived C 9 alkenes. *Green chemistry*, *12*(6), 992-999.

21. Chan-Thaw, C. E., Marelli, M., Psaro, R., Ravasio, N., & Zaccheria, F. (2013). New generation biofuels: γ-valerolactone into valeric esters in one pot. *RSC advances*, *3*(5), 1302-1306.

22. Lange, J. P., Price, R., Ayoub, P. M., Louis, J., Petrus, L., Clarke, L., & Gosselink, H. (2010). Valeric biofuels: a platform of cellulosic transportation fuels. *Angewandte Chemie International Edition*, *49*(26), 4479-4483.

23. Nobbs, J. D., Zainal, N. Z. B., Tan, J., Drent, E., Stubbs, L. P., Li, C., ... & van Meurs, M. (2016). Bio–based Pentenoic Acids as Intermediates to Higher Value-Added Mono-and Dicarboxylic Acids. ChemistrySelect, 1(3), 539-544.

24. Bond, J. Q., Martin Alonso, D., West, R. M., & Dumesic, J. A. (2010). γ-Valerolactone ring-opening and decarboxylation over SiO2/Al2O3 in the presence of water. *Langmuir*, *26*(21), 16291-16298.

25. Bodor, N., Gabanyi, Z., & Wong, C. K. (1989). A new method for the estimation of partition coefficient. *Journal of the American Chemical Society*, *111*(11), 3783-3786.

26. O'Connor, D. J., & Connolly, J. P. (1980). The effect of concentration of adsorbing solids on the partition coefficient. *Water Research*, *14*(10), 1517-1523.

27. Banerjee, S., Yalkowsky, S. H., & Valvani, C. (1980). Water solubility and octanol/water partition coefficients of organics. Limitations of the solubility-partition coefficient correlation. *Environmental Science & Technology*, *14*(10), 1227-1229.

28. Alboudwarej, H., Akbarzadeh, K., Beck, J., Svrcek, W. Y., & Yarranton, H. W. (2003). Regular solution model for asphaltene precipitation from bitumens and solvents. *AIChE Journal*, *49*(11), 2948-2956.

29. Black, C. (1958). Phase Equilibria in Binary and Multicomponent Systems. Modified van Laar-Type Equation. *Industrial & Engineering Chemistry*, *50*(3), 403-412.

30. Fan, C., & Jafvert, C. T. (1997). Margules equations applied to PAH solubilities in alcohol− water mixtures. *Environmental science & technology*, *31*(12), 3516-3522.

31. Anderson, T. F., & Prausnitz, J. M. (1978). Application of the UNIQUAC equation to calculation of multicomponent phase equilibria. 1. Vapor-liquid equilibria. *Industrial & Engineering Chemistry Process Design and Development*, *17*(4), 552-561.

32. Oence, D. N., & Gu, T. (1996). Liquid-liquid equilibrium of the acetonitrile-water system for protein purification. *Separations Technology*, *6*(4), 261-264.

33. Bond, J. Q., Jungong, C. S., & Chatzidimitriou, A. (2016). Microkinetic analysis of ring opening and decarboxylation of γ-valerolactone over silica alumina. *Journal of Catalysis*, *344*, 640-656.

35. Emel'yanenko, V. N., Kozlova, S. A., Verevkin, S. P., & Roganov, G. N. (2008). Vapour pressures and enthalpies of vapourization of a series of the γ-lactones. *The journal of chemical thermodynamics*, *40*(6), 911-916.

36. Emel'yanenko, V. N., Verevkin, S. P., Burakova, E. N., Roganov, G. N., & Georgieva, M. K. (2008). The thermodynamic properties of 4-pentenoic acid. *Russian Journal of Physical Chemistry A, Focus on Chemistry*, *82*(9), 1521-1526.

37. Wang, G., Liu, X., Yang, B., Si, C., Parvez, A. M., Jang, J., & Ni, Y. (2019). Using green γ-valerolactone/water solvent to decrease lignin heterogeneity by gradient precipitation. *ACS Sustainable Chemistry & Engineering*, *7*(11), 10112-10120.

38. Ahmed, M. A., Lee, J. H., Raja, A. A., & Weon, C. J. (2020). Effects of gamma-valerolactone assisted fractionation of ball-milled pine wood on lignin extraction and its characterization as well as its corresponding cellulose digestion. *Applied Sciences*, *10*(5), 1599.

39. Leonovich, S. A. (2004). Phenol and lactone receptors in the distal sensilla of the Haller's organ in Ixodes ricinus ticks and their possible role in host perception. *Experimental & applied acarology*, *32*(1), 89-102.

40. Zheng, P., Zhang, X., Fang, J., & Shen, W. (2016). Thermodynamic study of mixed surfactants of polyoxyethylene tert-octyl phenyl ether and dodecyltrimethylammonium bromide. *Journal of Chemical & Engineering Data*, *61*(2), 979-986.

41. Schwartz, T. J., & Bond, J. Q. (2017). A thermodynamic and kinetic analysis of solvent-enhanced selectivity in monophasic and biphasic reactor systems. Chemical Communications, 53(58), 8148-8151.

42. Norrish, R. (1966). An equation for the activity coefficients and equilibrium relative humidities of water in confectionery syrups. *International Journal of Food Science & Technology*, *1*(1), 25-39.

43. Tsonopoulos, C., & Wilson, G. M. (1983). High-temperature mutual solubilities of hydrocarbons and water. Part I: Benzene, cyclohexane and n-hexane. *AIChE Journal*, *29*(6), 990-999.

44. Qin, R., Zander, A. K., Semmens, M. J., & Cussler, E. L. (1990). Separating acetic acid from liquids. *Journal of membrane science*, *50*(1), 51-55.

Chapter 4

Optimization of selective pentenoic acids production from ring opening of gamma valerolactone over solid catalysts

4.1 Introduction

On the purpose of reducing greenhouse gas emissions, there are urgent demands to find alternative energy sources [1]. Lignocellulosic biomass is a promising carbon alternative considering its abundance and cost-effectiveness in nature [2]. In recent years, researches have been performed to find valuable biomass-derived intermediates based on the conversion of Lignocellulosic-biomass [3]. Such intermediates can be further converted into a range of valuable commercial products [4]. γ-valerolactone (GVL), one of the novel platform chemicals generated from upgrading of lignocellulose, can be utilized to produce polymer precursors, biofuels, and valuable chemicals
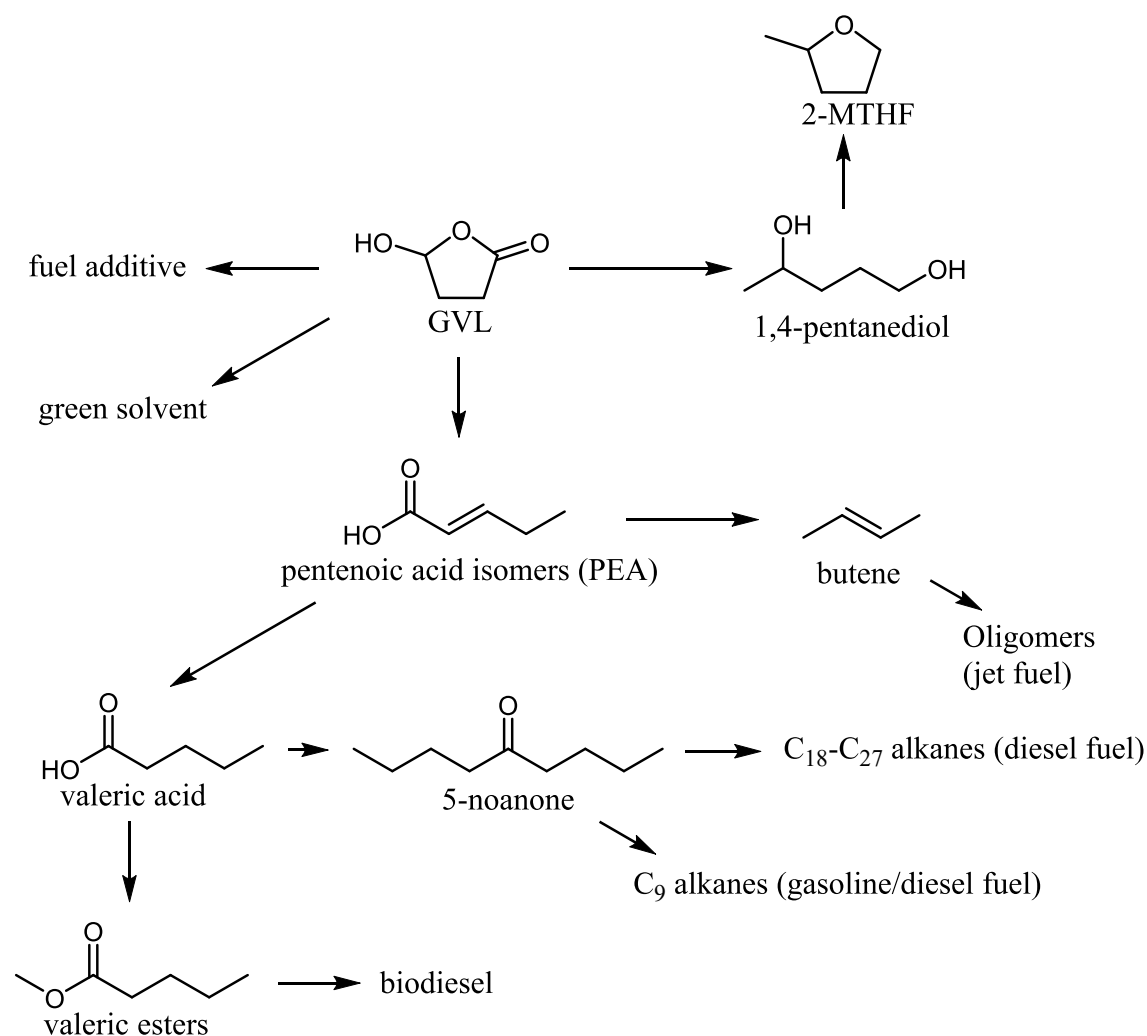
Figure 4.1: Scheme for the potential application of GVL and the role of PEA as the core intermediate.

as illustrated in the scheme 4.1 [5-9]. Among several applications of GVL, we can notice that pentenoic acid (PEA) served as the bridge to produce biodiesels, gasoline and diesel fuels further. However, selective preparation of PEA is challenging. First, GVL ring opening is an endothermic but entropically favorable reaction, which makes the equilibrium not favorable at low temperature environments. Moreover, as temperature increases, the PEA decarboxylation becomes kinetically favorable, offsetting the benefits from improved thermodynamic equilibrium [10]. Thus, it is difficult to find the operation windows for GVL ring opening without further decarboxylation.

Previously, Wang *et al.* have found that for GVL ring opening and decarboxylation over γ-Al_2O_3, which consists of both Brønsted and Lewis acid sites, the overall yield to butene was around 40% with WHSV equals to 0.18 h^{-1} at 648K. Meanwhile, over SiO_2/Al_2O_3, which primarily comprises Lewis acid sites, the overall yield to butene is more than 90% at the same condition, which is two times more than that over γ-Al_2O_3 [11]. Moreover, after introducing Brønsted acid on the γ-Al_2O_3, the butene yield climbed up accordingly. This indicated that Lewis acid sites are less active than Brønsted acid in the PEA decarboxylation reaction. Moreover, Khan *et al.* recently reported that oxocarbenium ions were formed over γ-Al_2O_3 in the presence of a Brønsted acid, facilitating the GVL ring opening on the surface [12]. Therefore, we proposed that selective production of pentenoic acid through ring opening of GVL can be achieved over solid catalysts with Lewis acids sites.

The γ-Al_2O_3, TiO_2, and ZrO_2 are commonly reported as Lewis acid materials and can be used as catalysts support in various reactions [13-18]. In this study, γ-Al_2O_3, TiO_2, and ZrO_2 along with SiO_2/Al_2O_3 are considered as direct catalysts to catalyze ring-opening of GVL. To our understanding, no such applications have been proposed before. The Brønsted acid site-based mechanism and Lewis acid site-based mechanism have been proposed by other groups [19,20].

However, no studies explore the activity of Lewis acid materials in the GVL ring opening. In this work, the various solid acids (silica alumina, gamma alumina, Titanium oxide, and Zirconium oxide) and their performance on GVL ring opening are investigated. To examine the activity of different catalysts, the yield and selectivity of PEA production are measured over a wide range of contact time and temperature in a packed bed reactor. Also, isopropanol and isopropylamine temperature programmed desorption (TPD) as well as pyridine Fourier-transform infrared spectroscopy (FTIR) are applied to determine the Brønsted site and Lewis sites density. Surface area information is collected by adsorption of N_2. Through analyzing variations in yield and selectivity of PEA over various catalysts along with structure characteristics, we try to find the ideal catalyst and best operation condition to realize highly selective PEA production. Also, further explanation for the relationship between catalyst activity on GVL ring opening and different catalyst surface characterizations is discussed.

4.2 Materials and Methods

4.2.1 Materials

Amorphous silica-alumina (ASA, SIAL 3113, Grace-Davison), gamma alumina (γ-Al_2O_3, Strem Chemicals, 97%), titanium dioxide (TiO_2, Acros Organics, Aeroxide® P25), and zirconium oxide anhydrous (ZrO_2, Thermal Fisher) were used as acid catalysts in this study for examining ring opening and decarboxylation of GVL. γ-valerolactone (GVL, >98%, Sigma-Aldrich) was used as reactant in this study and was purified over molecular sieves ((5% w/v, 12–24 mesh, Strem Chemicals)) prior to use. Tran-2-pentenioc acid (PEA, 97%, Acros), 4-Pentenoic acid (97%, Sigma-Aldrich), 3-trans-pentenoic acid, (95%, TCI America), 1-butene (1 % in Helium, Airgas), and propylene (1% in Helium, Airgas) were used as standards for instrument calibration without further purification. Isopropylamine (IPA, 99%, Acros), isopropanol (>99.6%, Acros, ACS reagent), and pyridine (>99.0%, Sigma-Aldrich) were used as probe molecule for acid site titration during TPD and FTIR experiments. They were used as purchased from manufacturers. Deionized water used in preparing GVL solutions, calibration standards, and HPLC mobile phases was prepared in-house by sequential reverse osmosis, UV oxidation, and double ion exchange. He (99.999%, Airgas), N_2 (99.999%, Airgas), and Air (Zero Grade, Airgas) were used in flow systems and chemisorption experiments without extra purification. Air used in calcination process during TPD, FTIR, and catalyst preparation procedure to remove water adsorption was obtained from in-house purge gas generator (Purge gas, CO2-PG14).

4.2.2 Catalysts Preparation

SIAL 3113 (Grace-Davison), γ-Al_2O_3 (Strem Chemicals, 95%), TiO_2 (Acros Organics, Aeroxide® P25), and ZrO_2 (Sigma-Aldrich) were obtained from commercial suppliers. Prior to kinetic studies

in the reactor, all catalysts are calcined in airflow (100 mL/min, 4h, 723K, 3K/min) to remove surface residues from manufacturers.

4.2.3 Surface area and pore size measurements

The surface area of samples was determined by N_2 (99.999%, Airgas) adsorption at 77K in a surface area and porosity analyzer (Micromeritics ASAP 2020). Prior to N_2 dosing, approximately 100 mg of sample was outgassed under vacuum for 4h at 623K. Total surface areas were determined by Brunauer-Emmett-Teller (BET) and t-plot micropore analyses. Pore volumes were characterized by nitrogen cumulation at a relative pressure of 0.995. Pore sizes were estimated by Barrett-Joyner-Halenda (BJH) analysis of the desorption branch of N_2 uptake isotherms [21].

4.2.4 Temperature Programmed Desorption

The Brønsted acid sites and Lewis acid sites are quantified by the temperature programmed desorption of isopropylamine and isopropanol, respectively.

Brønsted acid site densities were determined by isopropylamine (Acros, 99%) temperature programmed desorption (TPD). Typically, 60-80 mg of powered catalysts were added into a 1/2-inch quartz tube between supported by two quartz wool (Grace) end plugs. The whole tube was further placed in an Omega ceramic furnace. The temperature of the furnace was regulated by a process controller (Love, series 16A) and monitored by a type K thermocouple (Omega). All samples were calcined under airflow (50 sccm). The cell was ramped to 723K (5 K/min) and was held at 723 K for 4 hours and subsequently cooled to 432K and purged in dry Helium flow (100 sccm) for more than 90 minutes. The Helium used in TPD experiments was dried over molecular sieves. Catalysts were further dosed in isopropylamine/Helium blend that was prepared by flowing Helium through an IPA saturated chamber. After saturation of IPA on the surface, physisorbed

isopropylamine was removed by applying a high Helium flowrate (400 sccm) for at least 1 hour. The furnace was then ramped to 973K (10 K/min) under Helium, including 1% Ar serving as an internal standard. Chemisorbed isopropylamine was converted into propene and ammonia after ramping. During the whole process, a mass-selective residual gas detector (Stanford Instruments RGA 100) was used to track MS signals of isopropylamine (m/z=44), propylene (m/z=41) and Ar (m/z=40) in the effluent. Evolved propylene was used to calculate Brønsted site density, assuming that one molecule of isopropylamine adsorbs per Brønsted site [22,23].

Total acid site density was determined by isopropanol (Acros, 99.6%, ACS reagent) temperature programmed desorption. All the procedure was the same as previous isopropylamine TPD except for two changes. First, during dosing process, the samples were dosed in isopropanol/Helium blend instead of isopropylamine/Helium blend at 373K instead of isopropylamine at 423K. Second, the scan parameters for MS signal were changed to isopropylamine (m/z=45), propylene (m/z=41) and Argon (m/z=40). Evolved propylene was used to calculate total site density, assuming that one molecule of isopropanol adsorbs per Lewis or Brønsted acid site [24-27].

4.2.5 FTIR spectroscopy

Brønsted acid sites to Lewis acid sites ratio was determined by transmission FTIR spectroscopy (Nicolet 6700 DTGS detector) of adsorbed pyridine on catalysts. Approximately 20 mg of sample was press into a 13mm pellet in a hydraulic press (5 tons force). This allowed us to prepare detectable coverages of surface species and minimize gas-phase interference simultaneously. The pellet further was loaded on a home-built in-situ cell that comprised of a vacuum tee (McMaster-Carr, 1½" OD) with 4 CaF_2 windows to seal the chamber. Two ¼" tubes were welded onto both sides of the vacuum tee body and each one was equipped with a ¼" bellows valve. The setup was adjusted and positioned thus allowing the IR beam to clearly pass through. Two cartridge heaters

(McMaster, 1/8" ×1 ¼") were applied to as heating sources for the cell along with and a type K thermocouple (Omega) and a PID controller (Love Controls, Series 16A) to monitor and control temperatures. Before acid site titration, catalysts were calcined as the pretreatment procedure described in the TPD experimental section. Subsequently, the catalyst pellet was cooled to 423K and purged under a flow of 100 sccm of Helium sccm gas that was dried by a liquid nitrogen trap followed by a moisture trap. The pellet was then dosed with 4 torrs of pyridine (Sigma Aldrich, 99%) that was introduced into system through a stainless-steel tee packed with quartz wool. After the pellet was fully saturated, the cell was purged under a Helium flow of 200 sccm at 423K to remove physiosorbed pyridine. Spectra were collected at 423K and Brønsted to Lewis acid site ratios were determined by the ratio of integrated IR bands at 1545 cm^{-1} and 1455 cm^{-1} respectively with correlation for the appropriate molar extinction coefficients as equation 4.1 illustrated, where *C(BAS, LAS)* represented the concentration of Brønsted acid sites and Lewis acid site on the catalyst surface and *IA (B, L)* represents the integrated absorbance of Brønsted acid sites and Lewis acid site in FTIR spectra respectively. All FTIR spectra involved in this sector are collected at 5-minute intervals until the signal reach steady state [28,29].

$$\frac{C(BAS)}{C(LAS)} = \frac{1.88 * IA(B)}{1.42 * IA(L)}$$

(4.1)

4.2.6 Catalytic activity testing

The investigation of the GVL ring-opening and subsequent decarboxylation over different solid acid catalysts was carried out in an up-flow, packed bed reactor. The setup is illustrated in figure 4.2. We measured the product selectivity, reaction rate, and product yield as a function of contact time (τ) and temperatures. Various mass of catalysts samples was loaded into a ½ inch tubular 316 stainless steel reactors. Two pieces of quartz wools were placed on both sides to hold the bed. The general bed length was 1-2 cm. Upstream and downstream dead volumes were filled with silica
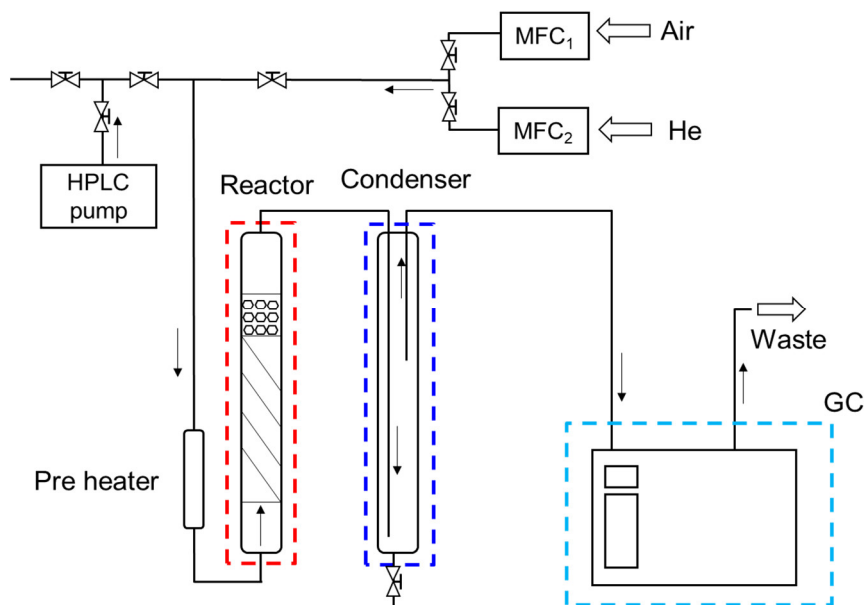
Figure 4.2: Setup of flow reactor for measuring kinetics of GVL ring opening in the aqueous environment.

chips (850-2000 um, 99.9%, Sigma Aldrich). The reactor was further placed in a special-designed

aluminum block which was placed in an insulated furnace (Applied Test System). A back pressure

regulator was used to control the reactor pressure. The reaction temperature was monitored by a

Type K thermocouple (Omega) with its tip right above the catalyst bed. The temperature of the

furnace was controlled by a PID controller (Love Controls, Series 16A). Prior to introducing GVL

feed, the catalysts were calcined in situ under air flow (50 sccm, 4h, 723K, 3K/min) using the same

pretreatment process mentioned before. And then the furnace was cooled down to reaction

temperature in Helium flow (50 sccm). In this study, multiple Brooks mass flow controllers (model

5850S) were used to provide constant gas flow into reactor.

An aqueous solution of GVL (4.04 wt%) in water was introduced to the system with a HPLC pump

(Lab Alliance Series I). The solution was warmed up in the pre heater and contacted with the

catalysis bed at reaction temperature in the reactor. The liquid components in the effluent such as

water, GVL and PEA were condensed in a water-cooling condenser. And liquid samples were

collected and analyzed in a GC-FID (Agilent Technologies, GC 7890A) with an autosampler. The

gas component in the effluent such as butene was further sent to a GC-FID (Agilent Technologies, GC 7890A). Both GCs were equipped with Innowax column and since CO_2 and PEA were produced in a 1:1 molar ratio during GVL decarboxylation, we inferred the CO_2 quantities based on butene quantities. GVL and PEA were calibrated by pre-prepared solution of GVL and PEA with different concentrations. Since each butene isomers share the same carbon and hydrogen numbers, their calibration factors were similar. We used the calibration factor of 2-butene for all butene isomers.

This study focuses on the activity and selectivity of GVL ring opening and decarboxylation over different materials. The discussion will emphasize probing the best condition and catalysts to maximize yield and selectivity of products (PEA and butene) as well as reaction rates of GVL ring opening and subsequent decarboxylation over different catalysts. The product yield and selectivity were defined as equation 4.2 and equation 4.3, respectively where n_j represented the molar quantities of specie j (PEA or butene) in a given amount of time and n_{GVL0} represented the total molar quantity of GVL introducing into the system in the corresponding period.

$$Y_j = \frac{n_j}{n_{GVL0}} \tag{4.2}$$

$$S_j = \frac{n_j}{\sum_i n_i} \tag{4.3}$$

In order to examine the extensive kinetics and intrinsic activity of Lewis acid sites on the catalysts surface, mass normalized reaction rates and acid site-normalized rates were introduced. Equation 4.4 defined mass normalized ring opening rate that was determined by the extensive production

$$R_{RO} = \frac{R_{PEA}}{m_{cat}} \tag{4.4}$$

$$R_{DC} = \frac{R_{Butene}}{m_{cat}} \tag{4.5}$$

$$STY_j = \frac{F_j}{S} = \frac{F_j}{C(acid\ site) \cdot m_{cat}} \tag{4.6}$$

rate of PEA. Equation 4.5 defined mass normalized decarboxylation rate that was determined by the extensive production rate of butene. The acid site-normalized rate (turn-over frequencies, TOF or site time yield, STY) was determined based on the extensive production rate normalized by the total acid sites on the surface of the catalyst, as equation 4.6 illustrated. Where S was the total molar quantity of Lewis acid sites on a catalyst surface, and F_j was the molar flow rate of GVL or PEA. $C(acid\ site)$ demonstrated the Lewis acid site density determined by the isopropanol TPD described before. m_{cat} was the catalysts mass in a reactor.

To investigate the dominant reaction during GVL ring opening and decarboxylation over catalyst surface at different temperatures, we measured product selectivities in various contact time (τ), which was defined by equation 4.7, where $\dot{m}_{GVL}$ denoted the mass flowrate of GVL. This number also equals one over the weight-hourly space velocities (WHSV).

$$\tau = \frac{1}{WHSV} = \frac{m_{cat}}{\dot{m}_{GVL}} \tag{4.7}$$

4.3 Results and Discussion

4.3.1 Catalyst characterization and activity in GVL ring opening and decarboxylation

Typically, SiO_2/Al_2O_3, γ-Al_2O_3, TiO_2, and ZrO_2 are used as supporting materials for some metal catalysts [30-32]. Lewis acid sites were reported as the predominant acid site on γ-Al_2O_3, TiO_2, and ZrO_2. At the same time, both Brønsted acid sites and Lewis acid sites were found on SiO_2/Al_2O_3 [33]. Table 4.1 summarizes the physical properties of catalysts involved in this study. Our observation here was consistent with previous researches. Brønsted acid strength can be defined by the TPD of isopropylamine. Meanwhile, it is much more challenging to determine the Lewis acid strength. However, recent reports have observed that the TPD of isopropanol dehydration reaction can occur on Lewis acid site with E_2 mechanism and on Brønsted acid site with E_1 mechanism [34]. Thus here, we determined the total acid sites by quantifying propene from the isopropanol dehydration RGA. Both isopropylamine TPD and isopropanol TPD profiles were included in the supply information. From table 4.1, we can see that SiO_2/Al_2O_3 had the highest surface area along with the highest Brønsted acid sites and Lewis acids sites density. The Lewis acidity of γ-Al_2O_3 is similar to SiO_2/Al_2O_3 (370.35 and 413.26 μmol/g). However, its Brønsted acidity is much lower comparing to SiO_2/Al_2O_3. Also, an approximate 43 μmol/g of propylene evolved from TiO_2 during isopropylamine TPD, suggesting a small amount of Brønsted acid sites existed on the TiO_2 surface. Finally, no Brønsted acid sites were observed on the ZrO_2

Catalysts	Surface area (m^2/g)	Micropore area (m^2/g)	Pore diameter (Å)	Pore volume (cm^3/g)	Brønsted acid sites (μmol/g)	Lewis acid sites (μmol/g)	BAS:LAS ratio
SIAL 3113	498	0	57	0.71	180.9	413.26	0.46
γ-Al_2O_3	282	18	87	0.61	44.0	370.35	0
TiO_2	107	5	189	0.51	43	100.06	0
ZrO_2	7	5	101	0.01	0	14.48	0

Table 4.1: Summary of physical and chemical properties of solid acids used in this study.

surface. ZrO$_2$ had a significantly small amount of surface area and Lewis acidity. Given the nature of materials, the Brønsted acidity we detected in γ-Al$_2$O$_3$ and TiO$_2$ may not attribute to the surface hydroxyls. Instead, residual impurities with unanticipated Brønsted acid sites were the primary reason behind such observations. First, the surface hydroxyls were reported not to be able to trigger the isopropylamine deamination reaction [35]. Moreover, the FTIR of adsorbed pyridine on γ-Al$_2$O$_3$ and TiO$_2$ showed that pyridinium ion formation was only detected at 1455 cm^{-1} [36]. Lack of adsorbed signal at 1545 cm^{-1} again confirmed our deduction that the Brønsted acidity in the γ-Al$_2$O$_3$ and TiO$_2$ was attributed to the residual impurities. Therefore, in this study, the GVL ring opening over SiO$_2$/Al$_2$O$_3$, γ-Al$_2$O$_3$, TiO$_2$, and ZrO$_2$ was considered only to occur on the Lewis acid site. This mechanism was reported by Dumesic`s group, which has declared a Lewis acid-based decarboxylation pathway and demonstrated the role of Lewis acid site [19].

Figure 4.3 illustrates the initial catalysts screening of GVL ring opening and decarboxylation by measuring the mass normalized rates at a fixed WHSV near 0.8 hr^{-1} at 598K. Of the materials
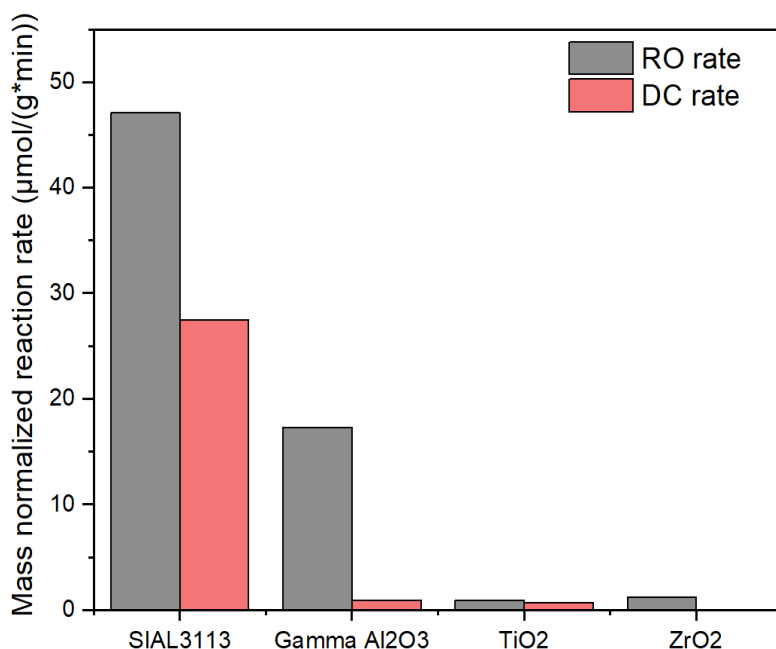
Figure 4.3: Comparison of mass-normalized GVL ring opening rate (RO) and decarboxylation rate (DC) over the solids acids considered in this study. The rates were measured at 598K and 1 bar GVL condition. The weight-hourly space velocities (WHSV) for these reactions were controlled near 0.8 hr^{-1}.

interested in the study, SiO_2/Al_2O_3 had shown the highest activity in GVL ring opening and decarboxylation, realizing 47 μmol/g/min. Meanwhile, the activity for γ-Al_2O_3 was relatively lower in GVL ring opening, but still remarkably higher than the RO rates in TiO_2, and ZrO_2 that were less than 2 μmol/g/min. With regards to GVL decarboxylation, SiO_2/Al_2O_3 was remarkably more active than other materials, with 27 μmol/g/min in DC rate. This measurement was consistent with reported value by Jesse at a similar condition [19]. Both γ-Al_2O_3 and TiO_2 had extremely low activity in decarboxylation at this condition, with a decarboxylation rate less than 1 μmol/g/min. No activity was observed for decarboxylation over ZrO_2. According to these observations, we found that the activity of solid acid catalysts on GVL ring opening and decarboxylation might align with their Lewis acidity and Brønsted acidity. The materials with higher Lewis acid site density such as SiO_2/Al_2O_3 and γ-Al_2O_3 had a relatively high GVL ring opening rate comparing to TiO_2 and ZrO_2 with less Lewis acidity. Meanwhile, γ-Al_2O_3, a material with high Lewis acidity and low Brønsted acidity, only showed activity in GVL ring opening instead of decarboxylation. And its decarboxylation rate was on the same magnitude with TiO_2, whose Lewis acid site density was almost the same with that of γ-Al_2O_3 (44 μmol/g for γ-Al_2O_3 and 43 μmol/g for TiO_2). Last but not least, since no Brønsted acidity was detected over ZrO_2, no decarboxylation behavior was observed as well. But one interesting thing that needed to point out was that ZrO_2 had a significantly lower Lewis acidity comparing to TiO_2 (14.48 μmol/g and 100.06 μmol/g, respectively). However, its ring opening rate was higher than TiO_2. This phenomenon will be explained in the following section. Overall, we proposed that the GVL ring opening may be catalyzed by the Lewis acid site, and the decarboxylation may be catalyzed by the Brønsted acid site in the hydrous environments. SiO_2/Al_2O_3 seems to be the most active catalysts, while γ-Al_2O_3 is a selective catalyst to produce PEA with an acceptable yield. And their activities for GVL ring

opening and decarboxylation are dominantly affected by the strength of Lewis acidity and Brønsted acidity, respectively. In the subsequent sections, we will examine the activity of these catalysts on GVL ring opening and decarboxylation over a wide range of contact time and temperatures to further probe other factors manipulating the selectivity and yield of PEA.

4.3.2 Contact time effects

With the aim of grasping a better understanding of the reactions, the contact time study was performed to examine which reaction was predominant on the catalysts surface when reactants had more time to interact with acid sites in the material. The contact time was controlled by changing the feed flowrate of GVL and the mass of the catalyst bed. Typically, the yields will increase as the contact time increases since there will be sufficient time for reactants to interact with active sites. But it became more complicated in the GVL ring opening and decarboxylation reaction.

Figure 4.4 illustrates the influence of contact time on the yield of PEA and butene over various solid acids at 300°C (573K). At this reaction temperature, SiO_2/Al_2O_3 achieved significantly higher PEA yield in a wide contact time range. The PEA yield over SiO_2/Al_2O_3 increased from 25% to 35% by increasing the contact time from 0.5 hour to 2.5 hour. Meanwhile, SiO_2/Al_2O_3 also showed

Figure 4.4: Influence of contact time on yield of PEA (left) and butene (right) over various solid acids at 300°C.

remarkably higher activity in GVL decarboxylation to form butene. The PEA yield over γ-Al_2O_3, TiO_2, and ZrO_2 were less than 10% but still increasing as contact time increased. At the longest contact time of 2.5 hours, the yield to PEA over γ-Al_2O_3 was around 10.2%, slightly higher than PEA yield over ZrO_2 (7.1%). The lowest PEA yield was measured over TiO_2, which was less than 5%. The yields to butene over γ-Al_2O_3, TiO_2, and ZrO_2 were negligible at 300°C. These observations suggested that at 300°C, the GVL ring opening was still the primary reaction on the catalysts surface and decarboxylation did not influence the selective production of PEA. The highest activity was still observed in SiO_2/Al_2O_3, followed by γ-Al_2O_3, ZrO_2 and TiO_2. This trend was the same as we described in the previous section.

Figure 4.5 illustrates the influence of contact time on yield of PEA and butene over various solid acids at 325°C (573K). The results showed that SiO_2/Al_2O_3 still had a relatively high activity compared to other solid acids at this temperature. However, the PEA yield over SiO_2/Al_2O_3 did not continuously increase as the contact time increased. The PEA yield rose slightly from 35% to 37% when the contact time was extended from 0.5 hours to 1.5 hours. After reaching the maximum PEA yield of 37%, the PEA yield started to decrease to 30% as the contact time reached 2.5 hours.
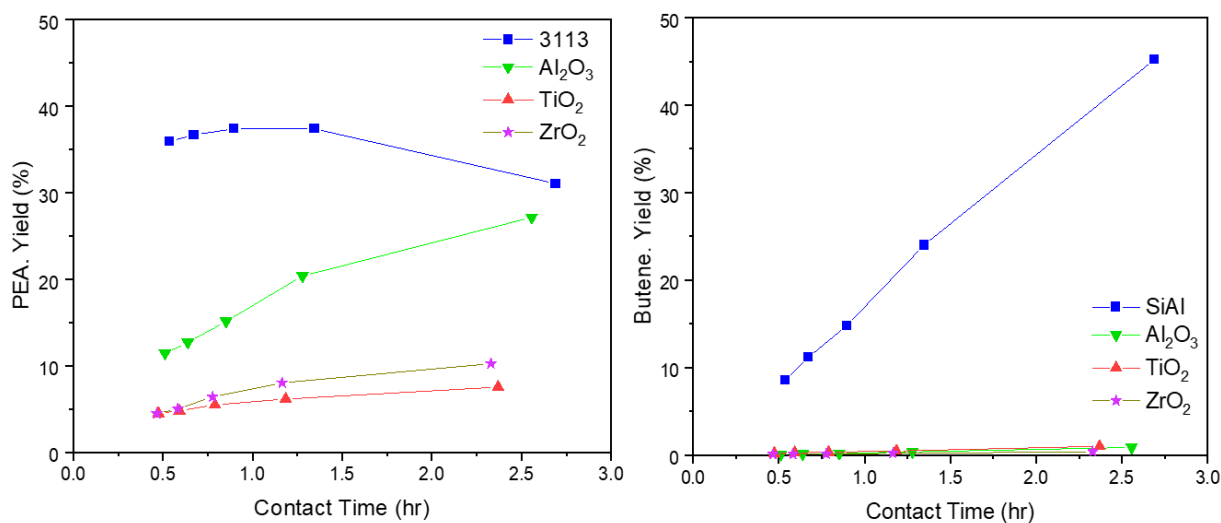
Figure 4.5: Influence of contact time on yield of PEA (left) and butene (right) over various solid acids at 325°C.

At the same time, the butene yield from GVL decarboxylation increased dramatically from 8% to 45%. For other solid acids, the PEA yield over ZrO_2 and TiO_2 increased moderately as contact time increased, but still less than 10%. However, the PEA yield over γ-Al_2O_3 increased significantly with contact time from 11% to 27%, which got a similar PEA production efficiency comparing to SiO_2/Al_2O_3 at this condition. Moreover, except for SiO_2/Al_2O_3, GVL decarboxylation over γ-Al_2O_3, TiO_2, and ZrO_2 was still inappreciable. Therefore, at 325°C, GVL ring opening was still the dominant reaction occurring on the surface of γ-Al_2O_3, TiO_2, and ZrO_2. However, GVL decarboxylation started to surpass the GVL ring opening over SiO_2/Al_2O_3. The longer contact time allowed PEA to have sufficient time to interact with the acid site on the surface and further being converted into butene, making SiO_2/Al_2O_3 a less selective catalyst comparing to γ-Al_2O_3.

The influence of contact time on yield of PEA and butene over various solid acids at 350°C (573K) was demonstrated in figure 4.6. At this reaction condition, the PEA yield over SiO_2/Al_2O_3 showed a similar trend at 325°C. The PEA yields increased in the low contact time region from 32% to 38% and suddenly dropped to 28% at the longest contact time. The butene yields over SiO_2/Al_2O_3 also
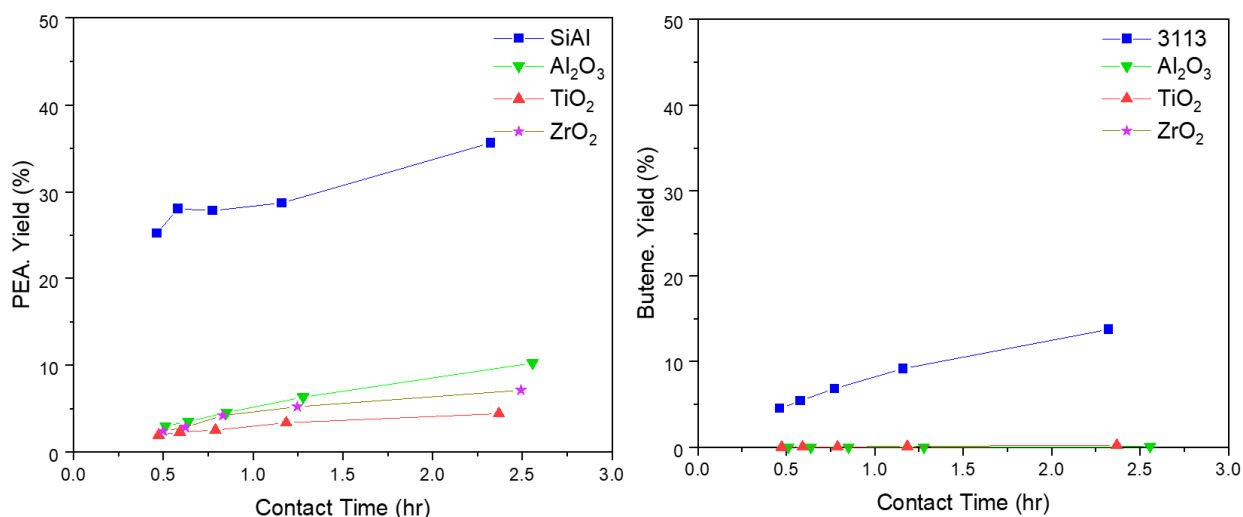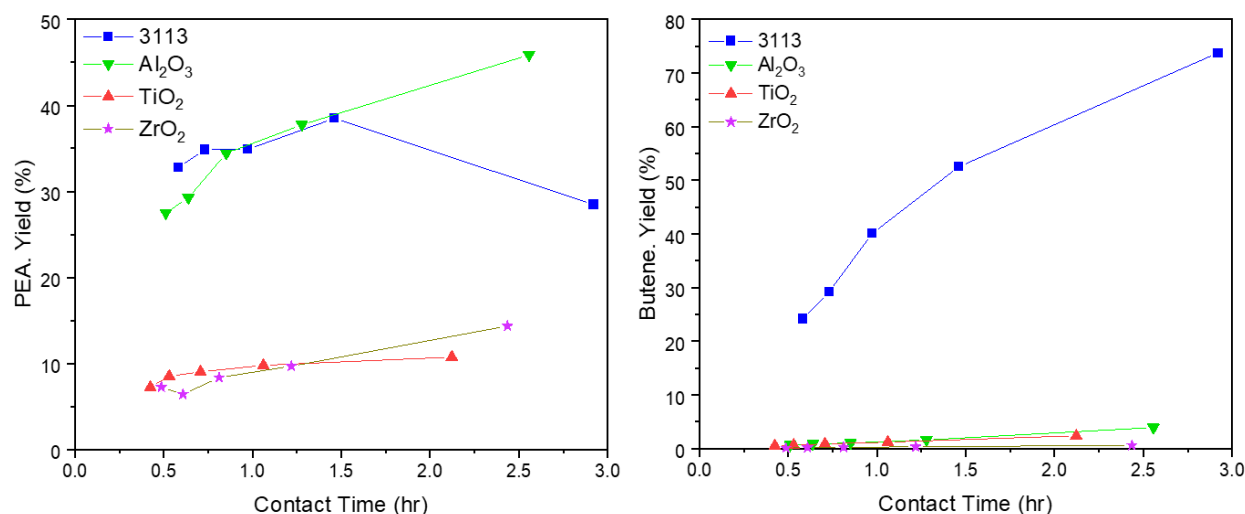

Figure 4.6: Influence of contact time on yield of PEA (left) and butene (right) over various solid acids at 350°C.

increased dramatically from 29% to 70% as contact time increasing. Over γ-Al$_2$O$_3$, the PEA yield did not witness a similar drop as the trend in SiO$_2$/Al$_2$O$_3$. It is worth pointing out that the γ-Al$_2$O$_3$ achieved a maximum PEA yield of 45%, which outmatched the maximum PEA yield of 38% over SiO$_2$/Al$_2$O$_3$ at this point. Meanwhile, the butene yield from GVL decarboxylation over γ-Al$_2$O$_3$ was still less than 5%, therefore making γ-Al$_2$O$_3$ the best catalysts for selective production of PEA at this condition. Moreover, the PEA yield over TiO$_2$, and ZrO$_2$ increased as a function of contact time from 7% to 10% and 7% to 14%, respectively. Simultaneously, the butene yield over TiO$_2$, and ZrO$_2$ remained less than 5%. At 350°C, the reaction rates for both GVL ring opening and decarboxylation increased. However, based on the previous report, GVL decarboxylation was more kinetically favorable at high temperature above 325°C [10]. Thus, as the temperature went up, the surface coverage of PEA was decreased by the subsequent decarboxylation to generate butene. Also, given that SiO$_2$/Al$_2$O$_3$ had the most accessible Brønsted acid sites and Lewis acids sites comparing to other solid acids, it appeared to have more activity in both reactions. However, a moderate amount of the Brønsted acid sites on SiO$_2$/Al$_2$O$_3$ leads to the result that the PEA formed from GVL ring opening was easier to undergo decarboxylation further to create butene. As for γ-Al$_2$O$_3$, it had a similar level of Lewis acid site concentration but less surface area and lower Brønsted acidity comparing to SiO$_2$/Al$_2$O$_3$. This allowed PEA to stay on catalyst surface longer without being further converted into butene, thus realizing a similar PEA yield to S at certain conditions. Although TiO$_2$ had more surface area and Lewis acid site comparing to ZrO$_2$, the PEA yield over TiO$_2$ was less than the PEA yield over ZrO$_2$. This may be attributed to the higher base acid site density and the coordinate effect on the surface of ZrO$_2$ during the deprotonation step during GVL ring opening to form PEA. A group in Japan found that despite fewer Lewis acid sites, ZrO$_2$ showed remarkably higher activity than TiO$_2$ due to a large amount of base site detected on

ZrO$_2$ [17]. The base sites were proposed to assist the deprotonation process with Lewis acid sites. The mechanism for GVL ring opening to form PEA included the initial step of ring opening and the following step of deprotonation. We thought has PEA formation may be benefited from this coordinate effect on ZrO$_2$ as well.

4.3.3 Temperature effects

To further investigate the trend observed above, we extended the temperature and contact time considered in this study. Figure 4.7 illustrates the temperature influence on the yield of PEA yield over SiO$_2$/Al$_2$O$_3$ at various contact times. We found that for SiO$_2$/Al$_2$O$_3$, the PEA yield was limited by intense decarboxylation. As the temperature increased from 260°C to 350°C at contact time below 2 hours, the PEA yield improved from 10% to 40%. Once reach the maximum yield of 40% at where the contact time was near 1.5 hours, the PEA yield started to decrease to 25% as contact time kept increasing. The selectivity shifts from PEA favorable to Butene favorable at this point. The butene yield can reach more than 70% and became the primary product at 350°C with a contact time of 2.7 hours. Thus, the operation window to realize selective production of PEA was really
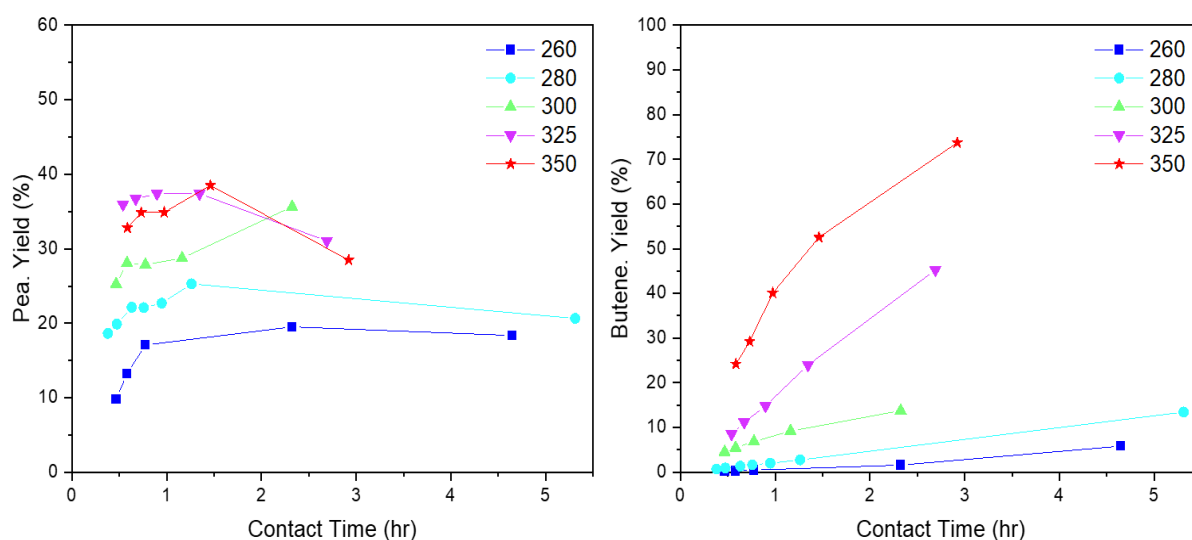
Figure 4.7: Influence of temperature on yield of PEA (left) and butene (right) over SiO$_2$/Al$_2$O$_3$ at various contact time.

narrow. At lower temperature and low contact time, the GVL ring opening reaction and show relatively high selectivity towards PEA. SiO_2/Al_2O_3 has a high Lewis acidity on the surface, contributing to high activity in GVL ring opening when the PEA had no sufficient time to interact on the surface. However, the Brønsted acid sites were reported to have the ability to catalyze PEA decarboxylation [10]. The high Brønsted acidity in SiO_2/Al_2O_3 makes this material favorable for the production of butene instead of Pea in most conditions. The PEA yield over SiO_2/Al_2O_3 thus was limited to 40% in all environments.

Figure 4.8 demonstrates the effect of temperature and contact time on the GVL ring opening and decarboxylation over γ-Al_2O_3. Comparing to S, γ-Al_2O_3 showed a much wider operation window for selective preparation of PEA. Below 375°C, the PEA yield did not show a trend of decline as the contact time increasing. At the operation condition where contact was beyond 3 hours, the PEA yield at 350°C was improved as a factor of 10 higher than that at 275°C. Meanwhile, the butene yield was still below 10%, rendering a reasonable selectivity to produce PEA near this condition. On the one hand, the Lewis acid site density on γ-Al_2O_3 was similar to SiO_2/Al_2O_3 based on our previous measurement. This makes γ-Al_2O_3 can achieve a comparable PEA yield of more than 40% at the maximum operating condition. On the other hand, the low Brønsted acid sites constrain the subsequent decarboxylation of PEA. Thus, γ-Al_2O_3 has shown a remarkably high selectivity comparing to SiO_2/Al_2O_3 at similar reaction environments. However, PEA decarboxylation became more favorable when the reaction temperature was beyond 350°C. At 350°C, the PEA yield maximized at 50% with a contact time near 0.5 hours and started to drop dramatically to 15% when the contact time reached 5 hours. This trend was similar to what we observed in SiO_2/Al_2O_3, indicating that the small amount of Brønsted acidity on the γ-Al_2O_3 surface can still perform a

significant effect on the conversion of GVL and PEA at high temperature regions. But still, γ-Al$_2$O$_3$ has shown the best potential to achieve a selective preparation of PEA in most conditions.
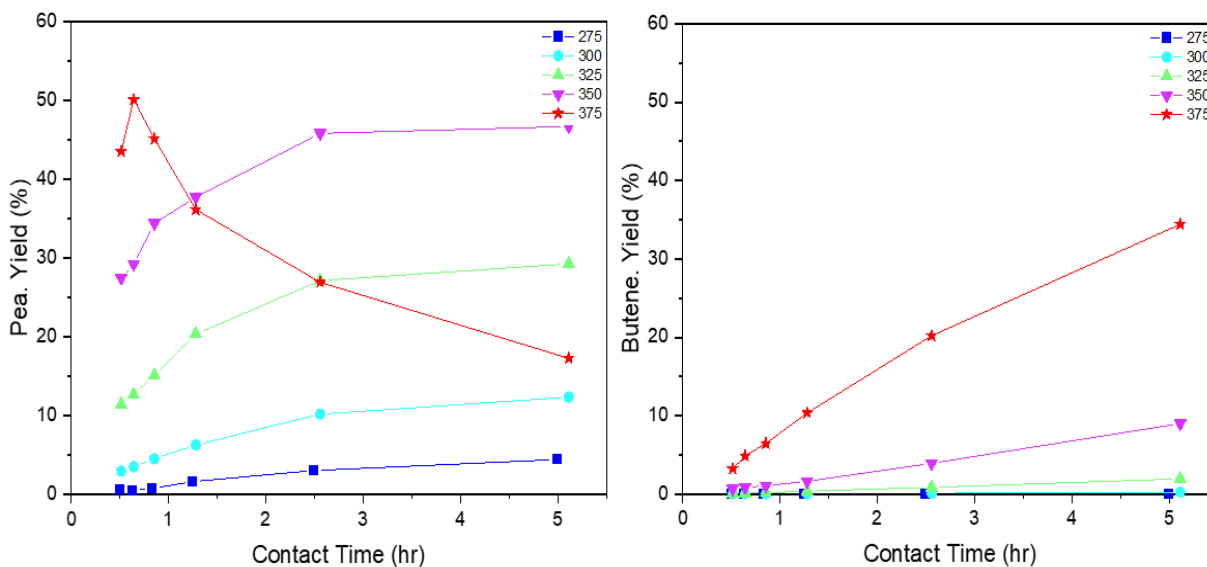
Figure 4.8: Influence of temperature on yield of PEA (left) and butene (right) over γ-Al$_2$O$_3$ at various contact time.

The performance of TiO$_2$ on GVL ring opening and decarboxylation is illustrated in figure 4.9. Different from SiO$_2$/Al$_2$O$_3$ and γ-Al$_2$O$_3$, the PEA yield over T was less promising. First, the PEA yields never surpassed 25% in the environments we tested. This was partially attributed to the lower surface area and lower Lewis acidity of TiO$_2$. The surface area of TiO$_2$ was half comparing
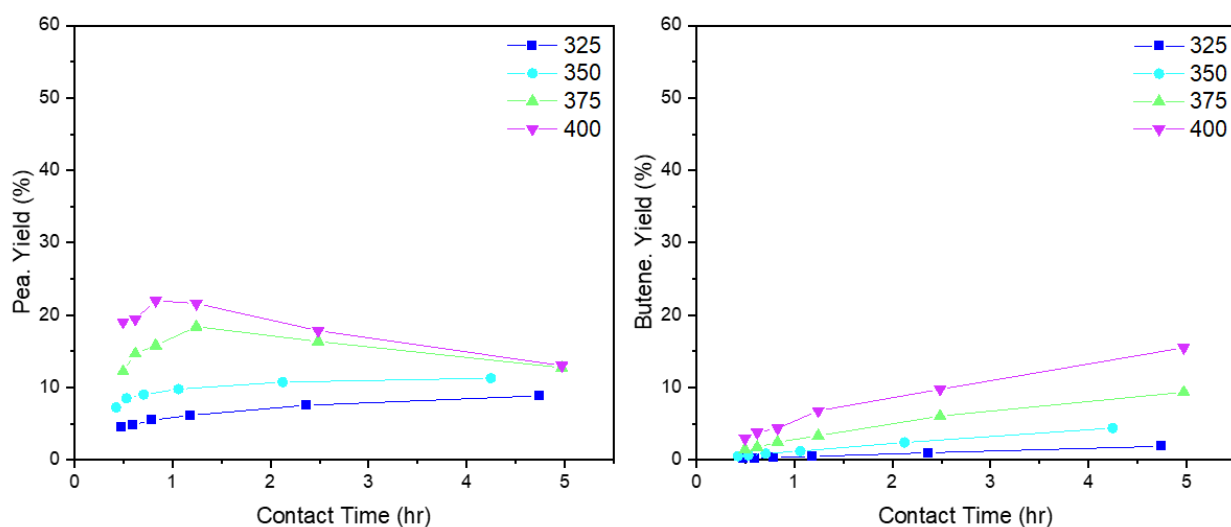
Figure 4.9: Influence of temperature on yield of PEA (left) and butene (right) over TiO$_2$ at various contact time.

to γ-Al$_2$O$_3$ with 282 and 107 m^2/g, respectively, which shared a close trend in the GVL ring opening activity. Moreover, at high temperature region above 375℃, the GVL ring opening became less favorable, and the PEA selectivity dropped as contact time increased. Considering that the Brønsted acid site density was only 50 μmol/g less than Lewis acid sites on the TiO$_2$ surface, the PEA decarboxylation would tend to become the dominant reaction on the surface comparing to GVL ring opening at high temperature regions. Overall, the selectivity and yield to PEA over TiO$_2$ were found to be relatively limited comparing to other materials.

The result for GVL ring opening over ZrO$_2$ is summarized in figure 4.10, and which had shown some really intriguing behaviors. Due to an absence of B sites on the ZrO$_2$ surface, the butene yield was significantly lower than other catalysts. At all tested conditions, the yield to butene never exceed 2%, rending a high selectivity to PEA accordingly. As a result, the PEA yields did not show a turning point as contact time increased, which made it has a wide operation window as well. Low surface area and Lewis acid sites on the solids may lead to low activity in catalytic performance, according to our observations in γ-Al$_2$O$_3$ and TiO$_2$. However, comparing to TiO$_2$, which has a ten times more surface area and Lewis acidity, we surprisingly found that ZrO$_2$ can achieve a similar PEA yield of 20% at 375℃. The inconsistency of activity and surface structure between ZrO$_2$ and TiO$_2$ indicates that the ZrO$_2$ was much more active compared to ZrO$_2$. Similarly, Komanoya *et al*. reported that ZrO$_2$ was more active compared to TiO$_2$ during the deprotonation progress despite less amount of Lewis acid sites and weak Lewis acid strength [17]. Gorte *et al*. also found that in the aqueous condition, the Lewis acid strength follows a trend γ-Al$_2$O$_3$ > ZrO$_2$ > TiO$_2$, which was consistent with our observation here [27]. The high activity in ZrO$_2$ was complex and can be attributed to several factors. One explanation was that the Lewis acid sites were not the primary contributor to the high catalytic performance of ZrO$_2$. Instead, the high concentration of
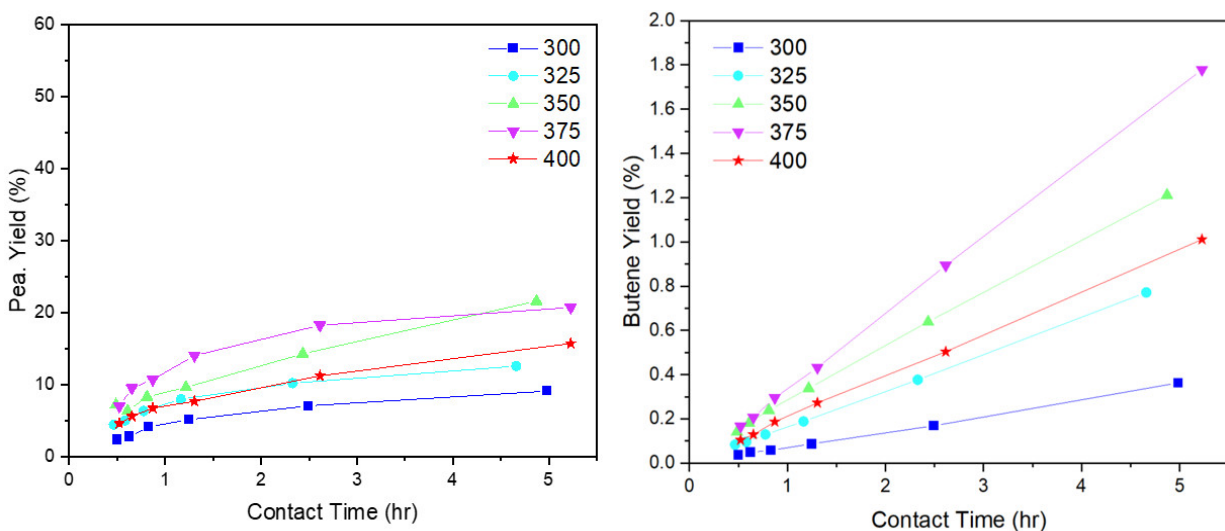
Figure 4.10: Influence of temperature on yield of PEA (left) and butene (right) over ZrO_2 at various contact time.

base sites on ZrO_2 can stabilize the transitional state of intermediates formed on the Lewis acid site, hence improving the overall activity of ZrO_2 [37]. The role of base sites in the GVL ring opening progress was still unclear and worth paying attention to in the future study. Another observation that needed to be pointed out was that at 400°C, the ZrO_2 lose a significant amount of activity comparing to that at 375°C. When the reaction was performed in contact time of 5 hours, both PEA yield and butene yield were less than 15% and 1% respectively, which were even less than the productivity observed in 350°C. This trend of loss in activity as temperature increases was not observed in other catalysts before. We proposed that this may ascribe to the deactivation on the catalyst surface. Since the surface area was trivial on the ZrO_2, the coking effect at high temperature environment may cause a much more obvious deactivation comparing to other materials with higher surface area. The accessible Lewis acid sites on the ZrO_2 may also be decreased as the surface area was influenced by coking. Overall, ZrO_2 has shown high selectivity to PEA but low activity in GVL ring opening due to the low surface area and Lewis acid sites. Also, the stability of ZrO2 was not promising as well. However, the relatively high catalytic performance was still worth further investigating.

4.3.4 Proximity to equilibrium positions

Considering that GVL ring opening to form PEA was a reversible reaction, we try to examine the relationship between the proximity to the thermodynamic equilibrium of GVL ring opening and the PEA selectivity. Reaction quotient, defined as the ratio between the PEA flowrate and GVL flowrate in the effluent, was introduced here to estimate the reaction direction of GVL ring opening. The equilibrium constant was calculated based on the reported enthalpy (44.7 kJ/mol) and entropy (71.9 J/mol/K) value [10]. Figure 4.11 summarizes the PEA selectivity as a function of Q/K with all the temperatures and contact time. From figure 4.11A, we can see that PEA selectivity can be correlated with the reaction position of GVL ring opening. When the reaction temperature was low, the GVL ring opening over SiO_2/Al_2O_3 was still far away from the equilibrium position. Also, reaction rates of GVL ring opening and decarboxylation were both low in this region. In this case, the reaction will be favorable towards the direction of generating PEA over the surface. As the temperature rises, the reaction rates for ring opening and decarboxylation were both increasing. However, with higher conversion of GVL and yield of PEA, the Q/K was also rising sharply. For instance, when the temperature went from 240°C to 280°C, the maximum Q/K increased from 0.55 to 0.9, indicating that the reaction was near equilibrium at this condition due to a higher activity of GVL ring opening. However, as the reaction was approaching equilibrium positions, the PEA selectivity started to decline. This can be attributed to the thermodynamic equilibrium prevented from GVL to further converted into PEA. Meanwhile, the decarboxylation of PEA can give butene and CO_2, leading to a significant increase in entropy in the system. Thus, the PEA always has the tendency to undergo decarboxylation in all reaction conditions. As a result, when the PEA coverage on the surface was near equilibrium position, it will spontaneously be converted into butene on the Brønsted acid sites. This process was still limited by the low reaction rate at low
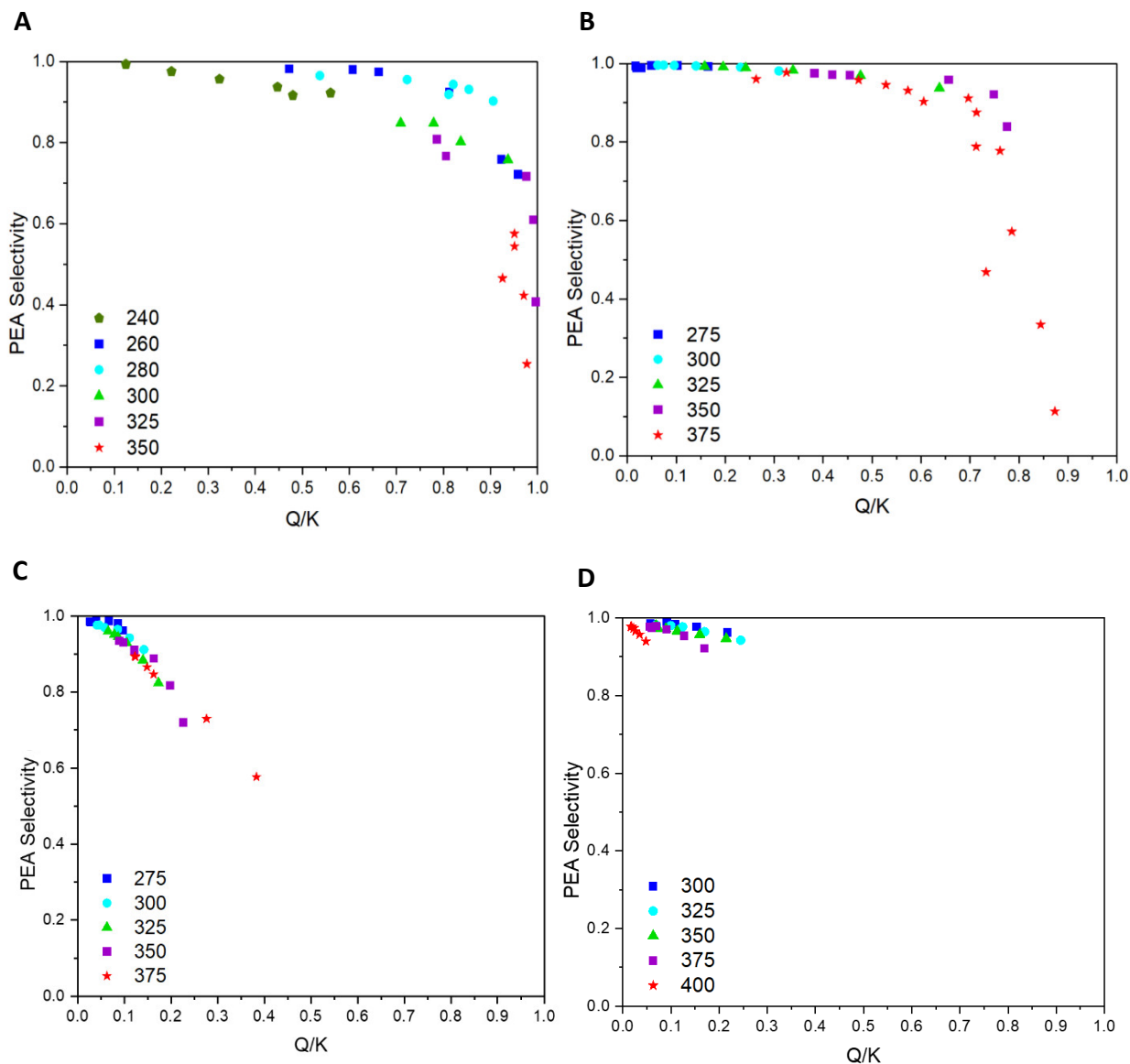
Figure 4.11: PEA selectivity as a function of proximity to equilibrium (Q/K) for GVL ring opening and decarboxylation over SiO_2/Al_2O_3 (A), γ-Al_2O_3 (B), TiO_2 (C), ZrO_2 (D).

temperature conditions. Bond *et al.* had reported an apparent kinetic barrier of 91kJ/mol and 138 kJ/mol for GVL ring opening and PEA decarboxylation, respectively [10]. Based on these values, at 240°C, the GVL site normalized ring opening rate was approximately $0.0114s^{-1}$, 27 times higher than the PEA decarboxylation rate of 0.004 s^{-1}. This gap will be narrowed as the temperature rises up. At 300°C, the ring opening was near 0.106 $s^{-1,}$ and the decarboxylation rate was 0.0126 s^{-1}. The difference has dropped less than a fold of 10. The gap will further reduce to a factor of 2 at 400°C.

Therefore, the temperature increase can not only push the GVL ring opening towards equilibrium, but also make PEA decarboxylation much more favorable, decreasing the total selectivity towards PEA. Furthermore, we can observe that the Q/K were high than 0.7 for temperatures higher than 300°C, suggesting that the GVL ring opening reaction was fast enough to get close to equilibrium in such environments. Besides high reaction rate, the larger surface area and a large amount of accessible Lewis acid sites allowed GVL to converted into PEA, pushing the reaction close to equilibrium as well. However, the large amount of Brønsted acid sites facilitate the PEA decarboxylation process. As a result, the PEA selectivity declined remarkably from 80% to 20% as Q/K raised from 0.8 to 1. This shift indicated that the PEA decarboxylation had replaced the GVL ring opening as the primary reaction on the SiO_2/Al_2O_3 surface, the latter of which was constrained by the thermodynamic equilibrium.

Figure 4.11B has concluded the PEA selectivity changes as Q/K over γ-Al_2O_3. A similar trend was observed comparing to SiO_2/Al_2O_3. PEA selectivity initially remained at a high level above 95% when Q/K was lower than 0.6. And once reaching a peak value at where Q/K equals 0.7, the PEA selectivity starts to drop significantly from 90% to less than 20%. This was still the same limitation from the thermodynamic equilibrium we described before. But different from SiO_2/Al_2O_3, the PEA yield only drop in some long contact time conditions at 375°C. From 275°C to 350°C, the PEA yield maintained more than 90% at a wide range of contact times, suggesting that γ-Al_2O_3 could have a much wider operation window to achieve PEA production at high selectivities. We proposed that such differences were derived from the lower concentration of Lewis acid sites and Brønsted acid sites over γ-Al_2O_3. The lack of Brønsted acid sites constrained the decarboxylation process of PEA. Meanwhile, slightly less of Lewis acid sites can slow down the PEA formation on the surface, which kept the GVL ring opening away from the equilibrium positions.

Figure 4.11C illustrates the trend of PEA selectivity as a function of Q/K over TiO_2. It appeared that when the reaction was away from equilibrium, at a region where Q/K was less than 0.1, the PEA selectivity over TiO_2 can still stay above 90%. However, in contrast to SiO_2/Al_2O_3 and γ-Al_2O_3, which can approach a high Q/K region, the GVL ring opening over TiO_2 never became more than 0.4. And the PEA selectivity dropped sharply from 90% to 60% when Q/K increased from 0.2 to 0.4, owing to a lack of Lewis acid site on the catalyst surface. The Lewis acid site concentration on TiO_2 was only ¼ comparing to that on GA and Si, therefore leaving the PEA production rate at a low extent and also limiting the conversion of GVL. As a result, at temperature below 350℃, the GVL ring opening on the surface was far away from equilibrium positions. However, the Brønsted acid density on TiO_2 was near 43 μmol/g, which was close to that on GA. This amount of Brønsted acidity was sufficient for PEA to undergo decarboxylation to give butene. Both factors resulted in a low PEA selectivity and conversion at all conditions tested in our study, making TiO_2 the least promising for realizing selective production of PEA.

Finally, the PEA selectivity over ZrO_2 across different Q/K is demonstrated in Figure 4.11D. Owing to the extremely low surface area and Lewis acidity, the GVL ring opening was constantly kept in a position far away from equilibrium with the Q/K less than 0.3. Also, bearing in mind that there was almost no Brønsted acid detect on the surface, the PEA did not have the accessible acid sites to be decarboxylated. Thus, the PEA selectivity maintained near 90% for all operating conditions. However, when the temperature increased to 375℃ and 400C, we observed that the reaction quotient was not growing accordingly. Instead, the maximum Q/K drop from 0.3 at 350℃ to 0.2 at 375℃, and went down to 0.05 at 400℃, indicating that the GVL ring opening was unfavorable in this environment. This was in conflict with fact GVL ring opening was an endothermic but entropically favorable reaction. Such kind of reaction generally should have a low

Gibbs free energy and showed a high Q/K at high temperature region. We considered this decline in Q/K and PEA selectivity as a sign of deactivation that we mentioned before. The ZrO_2 may start deactivating near 375°C and completely lost all its active site at 400°C, leading to a considerable drop in the catalytic performance of GVL ring opening.

4.3.5 Examination of apparent kinetics over of solid acids

Aiming at gaining more information about the kinetics in this reaction over various solids, we now examined mass normalized rates for GVL ring opening and decarboxylation at 300°C, 325°C, and 350°C. Here, we defined the ring opening rate and decarboxylation rate as the flowrate of PEA and flowrate of butene divided by the mass of catalysts used in the reaction, respectively. Given that GVL ring opening was a reversible reaction, the most accurate method to determine the ring opening rate should consider the deactivation profile and track to the production rate of PEA at zero time on stream. However, in this study, we would not look deep into the kinetics for GVL ring opening over different materials. Our definition of ring opening rate could be sufficient to generate a brief understanding towards the activity of different solid acids.
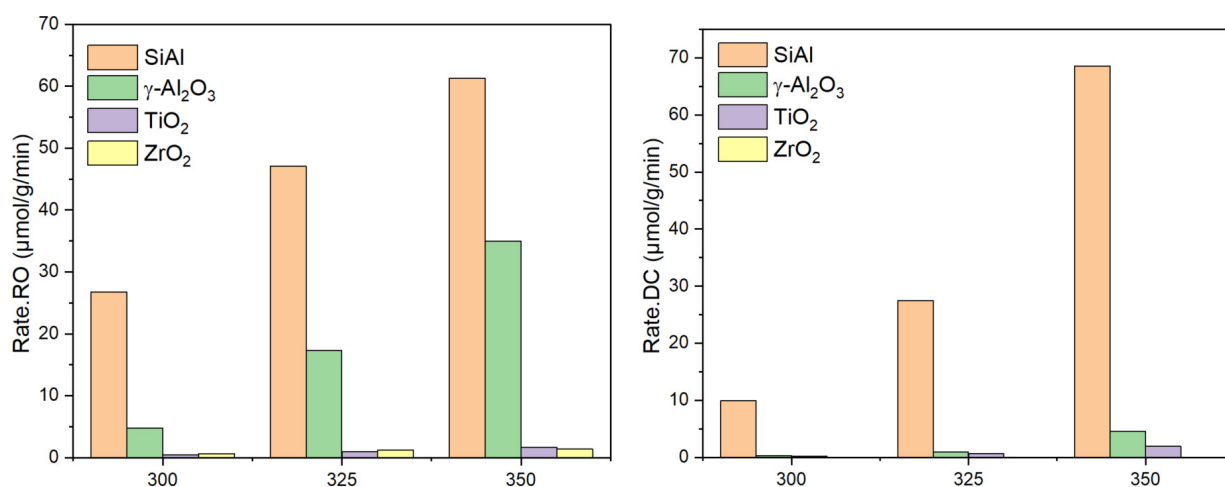
Figure 4.12: Mass-normalized GVL ring opening rate (left) and decarboxylation rate (right) over the solids acids considered in this study at 300°C, 325°C and 350°C. Rates are reported at a fixed weight-hourly space velocity (WHSV) of 0.8 hr^{-1} with GVL feed at 1 bar.

Figure 4.12 illustrates the reaction rate at three different temperatures: 300°C, 325°C, and 350°C. The ring opening rate was higher than the decarboxylation rate near all reaction environments. This was consistent with the report that GVL ring opening had a less apparent barrier comparing to PEA decarboxylation. In addition, we observed the mass normalized rates followed the trend as $SiO_2/Al_2O_3 > \gamma\text{-}Al_2O_3 > TiO_2 \approx ZrO_2$. This trend was consistent with previous observations on the yield of PEA at these conditions. SiO_2/Al_2O_3 showed a significantly high reaction rate in both ring opening and decarboxylation with a least factor of two comparing to other catalysts. Meanwhile, $\gamma\text{-}Al_2O_3$ only showed a high rate in GVL ring opening. The PEA production rate improved from 4.7 µmol/g/min at 300°C to 35 µmol/g/min at 350°C. And the butene production rate was still less than 5 µmol/g/min. This made $\gamma\text{-}Al_2O_3$ a practical catalyst to produce PEA without further decarboxylation. Last but not least, the low production rate over both TiO_2 and ZrO_2 suggested that these two materials were unpromising in this application.

In addition, we tried to examine the Lewis acid site strength based on the normalized the ring opening reaction with the Lewis acids sites detected on the surface, which was also known as the site time yield (STY). The figure 4.13 summarizes the STY of materials of interest here. The STY of ring opening represented how many PEA molecules can be transformed on a single Lewis acids site per minute. Based on our results, the SiO_2/Al_2O_3 had the highest Site time yield among all catalysts in all conditions, indicating that it has the highest Lewis acid strength. The overall Lewis acid strength followed a descending order as $SiO_2/Al_2O_3 > ZrO_2 > \gamma\text{-}Al_2O_3 > TiO_2$ based on the STY measured here. Besides ZrO_2, the trend that $SiO_2/Al_2O_3 > \gamma\text{-}Al_2O_3 > TiO_2$ was consistent with the electronegativity of elements in the solid acids. Normally, the Lewis acid strength has a dependence on electronegativity. The Lewis acid is an electro-pair acceptor, and a higher
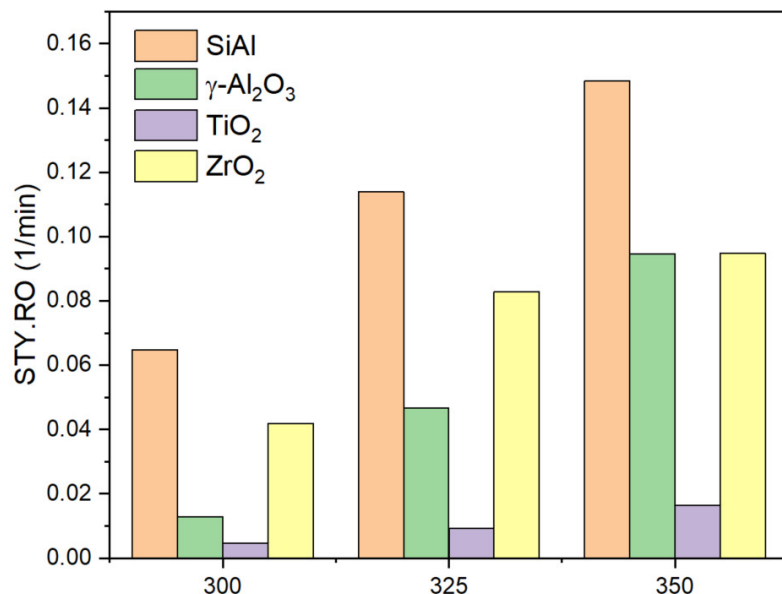
Figure 4.13: Site time yield of solids acids considered in this study at 300°C, 325°C and 350°C. Rates are reported at a fixed weight-hourly space velocity (WHSV) of 0.8 hr^{-1} with GVL feed at 1 bar.

electronegativity of the central atom involved in a reaction was associated with a stronger ability to accept electrons from the reactant, indicating a stronger acidity. Based on Pauling`s scale, the electronegativity of solids acids we studied here followed a trend of Si (1.90) > Al (1.61) > Ti (1.54) > Zr (1.33). Except ZrO_2, the Pauling electronegativities of Si (1.90) > Al (1.61) > Ti (1.54) agreed with our observation of decreasing Lewis acid strength as SiO_2/Al_2O_3 > γ-Al_2O_3 > TiO_2. However, Zr (1.33), with the lowest electronegativity, represented an inconsistent high strength of Lewis acid strength. The Lewis acid strength of ZrO_2 was between SiO_2/Al_2O_3 and γ-Al_2O_3 at 300°C and 325°C. This may be attributed to the high amount of base sites in the ZrO_2. As mentioned before, the large amounts of base sites on the ZrO_2 surface can assist with the Lewis acid site to stabilize the intermediate`s transitional state energy [17]. The role of base site in the GVL ring opening was still unclear and requires future study. Last but not least, the increase of STY over ZrO_2 was slowed down at 350°C, identical to the activity of γ-Al_2O_3 at this point. This may indicate the start of deactivation and poison of Lewis acid sites on the ZrO_2 surface.

4.3.6 Catalytic stability of solid acids

In the last section, we examined the deactivation of solid acids we used in the reactor. High PEA yield and Selectivity were not the only standards for a promising catalyst. The stability under reaction conditions also needed to be considered. After finishing the contact time and temperature study, we collected the used catalysts from the reactor tube and characterized these spent samples with BET analysis, FTIR spectra of pyridine, and temperature programmed desorption of isopropanol and isopropylamine to examine the change in surface area, Brønsted and Lewis acidity.

Based on the color of samples recovered from the reactor, all solid acids turned into black or brown solids from the original white powder, suggesting that coking may be the primary factor here contributing to deactivation. To investigate the changes in surface area and the regenerability of the catalysts, we initially carried out the BET analysis on the used samples without calcination and with calcination. Figure 4.14 summarizes the change in surface area at different conditions. Post-reacted catalysts represented the catalysts recovered from reactors without any further treatment. Post calcined catalysts represented the spent catalysts that further calcined in airflow at 450°C for 4 hours to remove the carbon residue on the surface of the catalyst. Table 4.2 summarizes the surface area loss after the reaction and calcination normalized the original surface area prior to reaction. It can be seen that all catalysts were found to lose a certain amount of surface area after finishing activity test. And the surface area can be partially restored after removing the carbon residue on the surface. The deactivation over TiO_2 was most severe, and it lost almost 80% of surface area after reaction. This explained our previous observation of low activity in TiO_2. After regeneration, 30% of the surface was recovered, still leaving an irreversible loss of surface area at 52% comparing to the fresh TiO_2. SiO_2/Al_2O_3 and γ-Al_2O_3 lost a similar amount of surface area
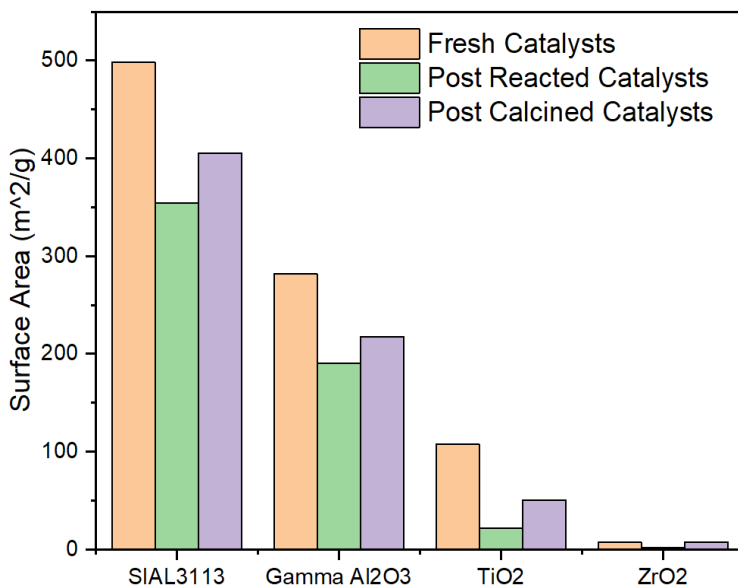
Figure 4.14: Surface area comparison as fresh catalysts, post reaction catalysts and post calcined catalysts based on the BET measurement in the ASAP.

Sample	Coking effects	Irreversible deactivation Effects
SiAl 3113	28.87%	18.62%
γAl_2O_3	32.36%	22.81%
TiO_2	79.95%	52.82%
ZrO_2	46.27%	-0.07%

Table 4.2: Calculation of surface area change comparing to the fresh status of the solid acids considered in this study.

after reaction, at around 30%. And 10% surface was regenerated after calcination for both materials.

The surface area on ZrO_2 was lost 46% initially but fully restored to the original status after calcination. This may attribute to a small surface area for ZrO_2 at fresh status (7 m^2/g). A low surface area made it easier to deactivate on the ZrO_2 surface, but the cooking area was also the least comparing to other large surface area materials. As a result, ZrO_2 has shown the best regenerability among these solid acids.

A recovery of surface area cannot totally guarantee the regeneration of activity of catalysts on GVL ring opening. The Brønsted and Lewis acids sites density were further examined and concluded in figure 4.15. All samples were calcined in airflow at 450°C for 4 hours after recovered

from the bed. From figure 4.15, it was apparent that SiO_2/Al_2O_3 lost the most active sites on the surface. After reaction and calcination, almost 250 μmol/g of Brønsted acid site and 100 μmol/g of Lewis acid sites were deactivated, which covered 49.82% of original Brønsted acidity and 60% of original Lewis acidity, respectively. γ-Al_2O_3 appears to be more stable than SiO_2/Al_2O_3 during GVL ring opening reaction. Only 27% of Lewis acid sites and 55% of Brønsted acid sites were lost after the reaction. The deactivation on the catalyst surface appears to be correlated with the acid site's performance and independent with surface area. For instance, SiO_2/Al_2O_3 has the most active Lewis acid site and the largest amount of site counts, leading to high GVL conversion and ring opening rates. Accordingly, its deactivation was most significant compared to other materials. Meanwhile, γ-Al_2O_3 has a relatively smaller surface area and acid strength, which showed a lower
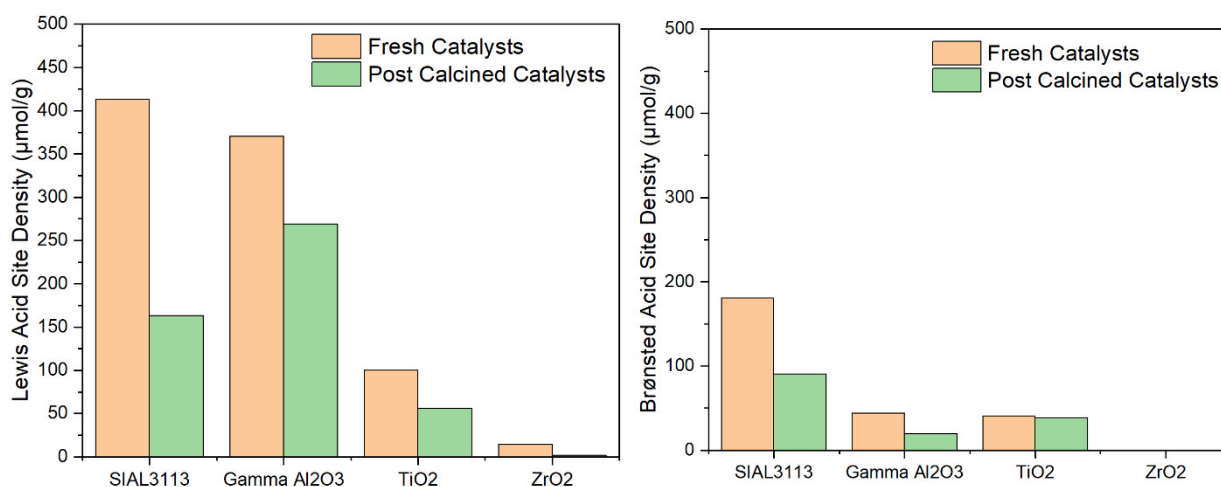
Figure 4.15: Comparison of Lewis (left) and Brønsted (right) acids sites density post reaction catalysts and post calcined catalysts based on temperature programmed desorption of isopropanol and isopropylamine.

Catalysts	Surface area (m^2/g)	Micropore area (m^2/g)	Pore diameter (Å)	Pore volume (cm^3/g)	Brønsted acid sites Loss	Lewis acid sites Loss	Surface area Loss
SIAL 3113	498	0	57	0.71	49.82%	60.51%	18.62%
γ-Al_2O_3	282	18	87	0.61	55.01%	27.36%	22.81%
TiO_2	107	5	189	0.51	5.44%	43.93%	52.82%
ZrO_2	7	5	101	0.01	N/A	89.50%	-0.07%

Table 4.3: Summary of deactivation and relevant physicochemical properties of tested solid acids.

activity in GVL ring opening than SiO_2/Al_2O_3. As a result, the loss of Brønsted and Lewis acids sites was both lower than the loss observed over SiO_2/Al_2O_3. This trend can be further extended to TiO_2, which has the most insufficient activity in GVL ring opening, lost only approximately 50 μmol/g of Lewis acid and a negligible amount of Brønsted acid sites. Overall, the high strength of Lewis acid sites will result in a high level of deactivation on the catalyst surface. Additionally, the higher density of Lewis acid sites will alleviate this effect by providing more accessible active sites for reaction. A larger surface area will also improve reactivity by decreasing the influence of coking on the surface. The irreversible deactivation observed here may attribute to the change of surface structure on these solid acids. As for ZrO_2, even though the surface area can be restored after calcination, 89.5% of Lewis acid sites on its surface were deactivated. This explained our observation at 375°C and 400°C that the ZrO_2 lost its activity in GVL ring opening. This suggested that the deactivation in Brønsted and Lewis acid site may not relate to the change in surface area. After calcination, the restoration of surface area cannot guarantee the activity will be recovered as well. Overall, considering the stability and regenerability of catalysts, γ-Al_2O_3 appeared to be the most promising material for GVL ring opening.

4.4 Conclusion

In the study, we have demonstrated that Lewis acid catalysts can be applied in the GVL ring opening reaction to selectively produce PEA in the aqueous environment. While previous reports have illustrated the application of Brønsted acidic catalysts and the role of Brønsted acid sites in the GVL decarboxylation. The catalytic performance of GVL ring opening and PEA decarboxylation has been compared over SiO_2/Al_2O_3, γ-Al_2O_3, TiO_2, and ZrO_2 which have different Brønsted and Lewis acid compositions. Based on our observations, it seems that Lewis acid site contribute significantly to the GVL ring opening while Brønsted acid site contribute more to PEA decarboxylation. Contact time and temperature can influence the yield and selectivity of PEA. But the real factor influences both parameters is the proximity to equilibrium. For instance, when the GVL ring opening is far away from equilibrium, the selectivity will be more favorable to PEA. When the GVL ring opening is close to equilibrium, the selectivity will shift towards butene. Thus, it is worth pointing out that when examining activity of catalysts over reversible reactions, contact time and conversion should not the only factors considered when comparing activities. Instead, the proximity of reaction to equilibrium may influence significantly on product distribution. Furthermore, a certain extent of deactivations has been observed based on the characterization of changes in surface area, Brønsted and Lewis acidity. Coking is the primary factor contributing to deactivation. However, the catalysts cannot be fully regenerated after calcination. Also, the recovery in the surface area does not indicate the regeneration in catalysts activity. Deactivation of catalysts seems to be associated with Lewis acidity, and the coking formation was more affected by surface area. This suggested that the catalysts with high surface area and acidity site density will show a high overall activity and more severe deactivation during a reaction.

Based on the solid acids investigated here, γ-Al_2O_3 is most promising in most operation conditions to be used as catalysts for selective preparation of PEA from GVL ring opening considering its high activity, high selectivity, and high regenerability. SiO_2/Al_2O_3 has also shown high activity in GVL ring opening. But the high activity in PEA decarboxylation makes it hard to control the selectivity more favorable to PEA. Given low surface area and Lewis acid site counts, TiO_2 was unpractical for this application. ZrO_2 has shown a high selectivity in PEA due to a lack of Brønsted acid site on the surface. However, it also exhibits relatively high activity in the Lewis acid site, which is opposed to the electronegativity of materials. This material has shown some interesting properties during our study and remains to be further investigated. For here, we propose that material with abundant Lewis acid sites and large surface area may be best for selective preparation of PEA from GVL ring opening.

4.5 Supplementary information

Figure S4.1 and S4.2 showed the desorption profile to Temperature programmed desorption of isopropanol and isopropylamine, respectively, which were used to measure the total acid site and Brønsted acid site density on the surface of fresh solid catalysts mentioned in this study.
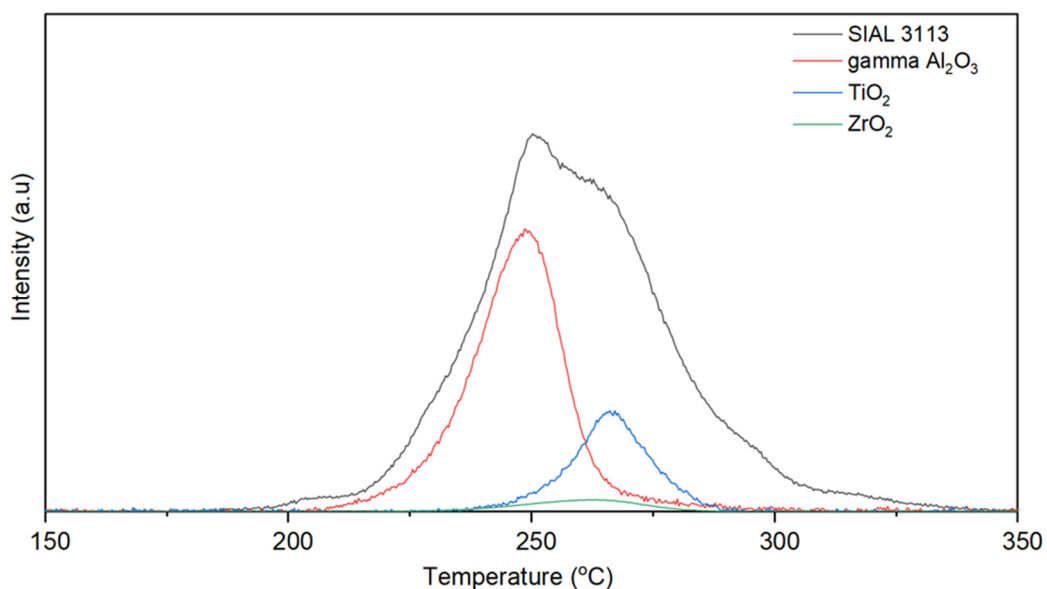
Figure S4.1: Temperature Programmed Desorption of Isopropanol for solid acids considered in the study. The peaks correspond to the propene (m/z=41) emitted on the catalysts surface were used to quantify the total acid strength.
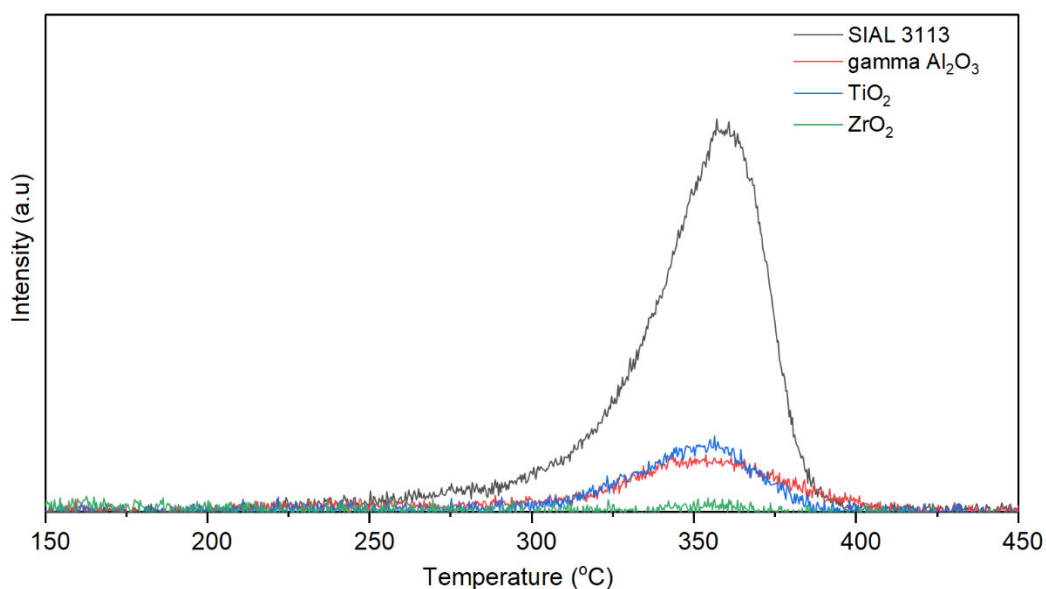
Figure S4.2: Temperature Programmed Desorption of Isopropylamine for solid acids considered in the study. The peaks correspond to the propene (m/z=41) emitted on the catalysts surface were used to quantify the Lewis acid strength.

Figure S4.3 illustrated the FTIR spectra of pyridine adsorption over SiO_2/Al_2O_3 to measure the Brønsted Acid to Lewis acid site ratio, where Brønsted and Lewis acid site ratios were determined by the integrated IR bands at 1545 cm^{-1} and 1455 cm^{-1}, respectively.
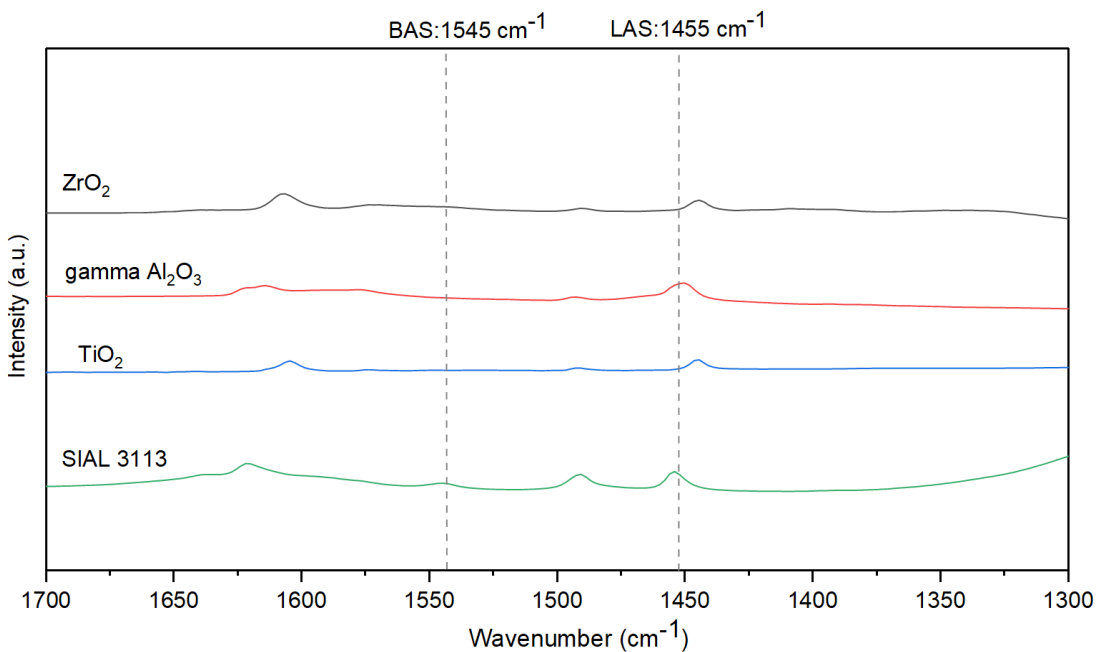
Figure S4.3: FTIR spectra of pyridine adsorption over materials of interest in this study. IR band is narrowed between 1300-1700 cm^{-1} to specify the BAS and LAS adsorption.
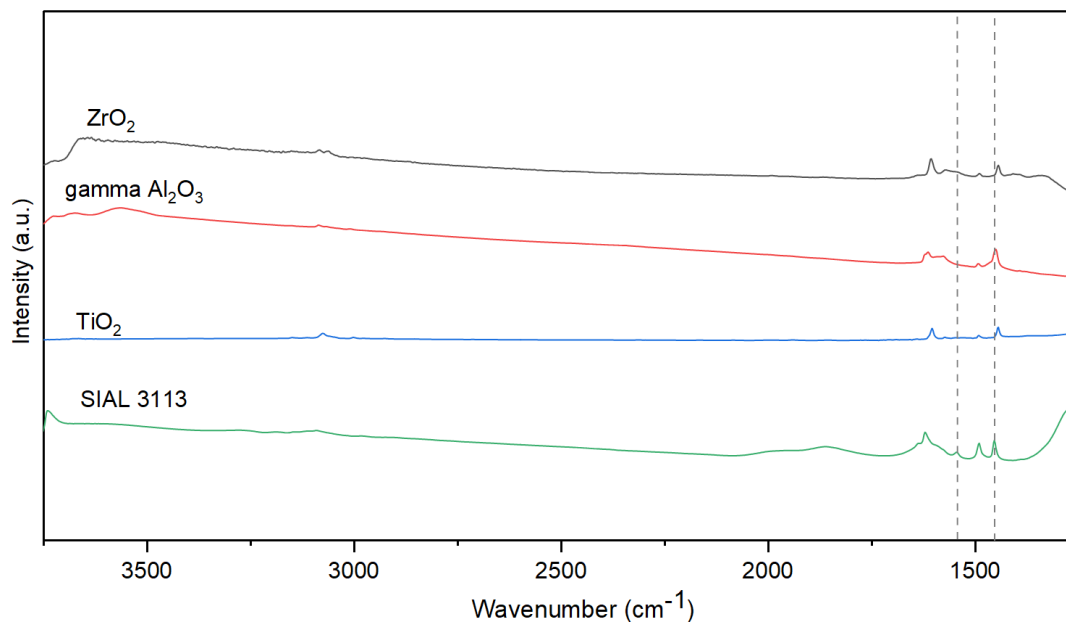
Figure S4.4: Complete FTIR spectra of pyridine adsorption over SiO_2/Al_2O_3, γ-Al_2O_3, TiO_2, and ZrO_2 at fresh status prior to reaction.
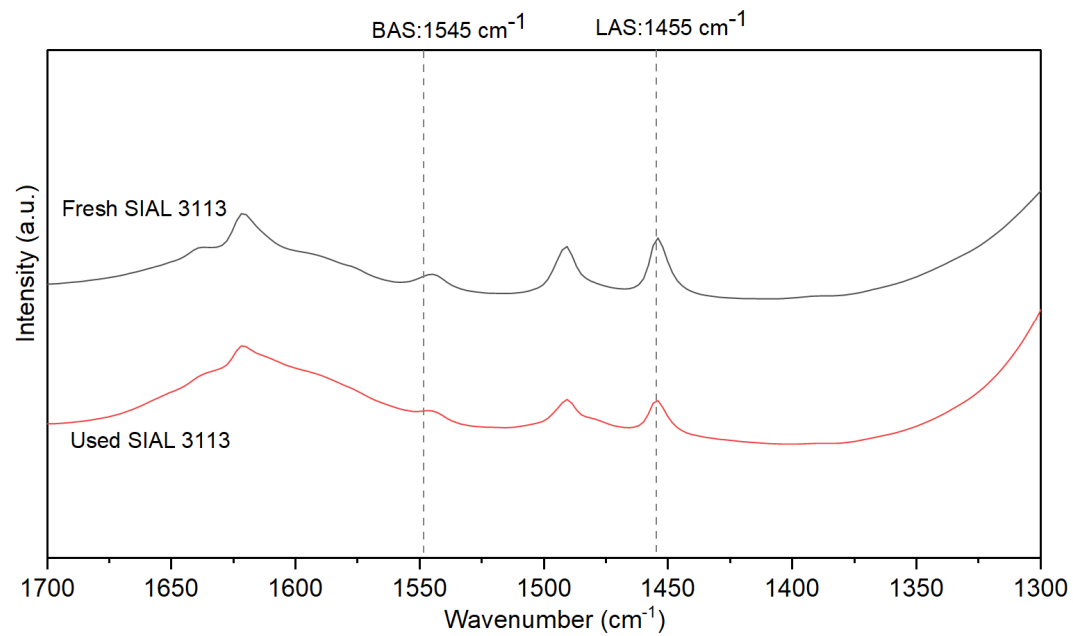
Figure S4.5: FTIR spectra of pyridine adsorption over SiO_2/Al_2O_3 before and after reaction.

4.6 References

1.   Demirbas, A. (2005). Potential applications of renewable energy sources, biomass combustion problems in boiler power systems and combustion related environmental issues. Progress in energy and combustion science, 31(2), 171-192.
2.   Knauf, M., & Moniruzzaman, M. (2004). Lignocellulosic biomass processing: a perspective. International sugar journal, 106(1263), 147-150.
3.   Nor, N. M., Lau, L. C., Lee, K. T., & Mohamed, A. R. (2013). Synthesis of activated carbon from lignocellulosic biomass and its applications in air pollution control—a review. *Journal of Environmental Chemical Engineering*, *1*(4), 658-666.
4.   Kuila, A., & Sharma, V. (Eds.). (2017). *Lignocellulosic biomass production and industrial applications*. John Wiley & Sons.
5.   Tabasso, S., Grillo, G., Carnaroglio, D., Calcio Gaudino, E., & Cravotto, G. (2016). Microwave-assisted γ-valerolactone production for biomass lignin extraction: a cascade protocol. Molecules, 21(4), 413.
6..   Ravikumar, V. R., Schröder, A., Köhler, S., Çetinel, F. A., Schmitt, M., Kondrakov, A., ... & Schmidt-Hansberg, B. (2021). γ-Valerolactone: An Alternative Solvent for Manufacturing of Lithium-Ion Battery Electrodes. ACS Applied Energy Materials, 4(1), 696-703.
7..   Obregón, I., Gandarias, I., Ocio, A., García-García, I., de Eulate, N. A., & Arias, P. L. (2017). Structure-activity relationships of Ni-Cu/Al2O3 catalysts for γ-valerolactone conversion to 2-methyltetrahydrofuran. Applied Catalysis B: Environmental, 210, 328-341.
8.   Du, X. L., Bi, Q. Y., Liu, Y. M., Cao, Y., He, H. Y., & Fan, K. N. (2012). Tunable copper-catalyzed chemoselective hydrogenolysis of biomass-derived γ-valerolactone into 1, 4-pentanediol or 2-methyltetrahydrofuran. Green Chemistry, 14(4), 935-939.
9.   Bond, J. Q., Alonso, D. M., Wang, D., West, R. M., & Dumesic, J. A. (2010). Integrated catalytic conversion of γ-valerolactone to liquid alkenes for transportation fuels. Science, 327(5969), 1110-1114.
10.   Bond, J. Q., Jungong, C. S., & Chatzidimitriou, A. (2016). Microkinetic analysis of ring opening and decarboxylation of γ-valerolactone over silica alumina. *Journal of Catalysis*, *344*, 640-656.
11.   Wang, D., Hakim, S. H., Alonso, D. M., & Dumesic, J. A. (2013). A highly selective route to linear alpha olefins from biomass-derived lactones and unsaturated acids. *Chemical Communications*, *49*(63), 7040-7042.
12.   Khan, T. S., Gupta, S., Bandodkar, P., Alam, M. I., & Haider, M. A. (2018). On the role of oxocarbenium ions formed in Brønsted acidic condition on γ-Al2O3 surface in the ring-opening of γ-valerolactone. *Applied Catalysis A: General*, *560*, 66-72.
13.   Harima, Y., Fujita, T., Kano, Y., Imae, I., Komaguchi, K., Ooyama, Y., & Ohshita, J. (2013). Lewis-acid sites of TiO2 surface for adsorption of organic dye having pyridyl group as anchoring unit. *The Journal of Physical Chemistry C*, *117*(32), 16364-16370.
14.   Kumar, V. V., Naresh, G., Sudhakar, M., Tardio, J., Bhargava, S. K., & Venugopal, A. (2015). Role of Brønsted and Lewis acid sites on Ni/TiO2 catalyst for vapour phase

hydrogenation of levulinic acid: Kinetic and mechanistic study. *Applied Catalysis A: General*, *505*, 217-223.

15. Riseman, S. M., Massoth, F. E., Dhar, G. M., & Eyring, E. M. (1982). Fourier transform infrared photoacoustic spectroscopy of pyridine adsorbed on silica-alumina and. gamma.-alumina. *The Journal of Physical Chemistry*, *86*(10), 1760-1763.

16. Peri, J. B. (1968). Effect of fluoride on surface" acid" sites on. gamma.-alumina and silica-alumina. *The Journal of Physical Chemistry*, *72*(8), 2917-2925.

17. Komanoya, T., Nakajima, K., Kitano, M., & Hara, M. (2015). Synergistic catalysis by Lewis acid and base sites on ZrO2 for Meerwein–Ponndorf–Verley reduction. *The Journal of Physical Chemistry C*, *119*(47), 26540-26546.

18. Zaki, M. I., Hasan, M. A., & Pasupulety, L. (2001). Surface reactions of acetone on Al2O3, TiO2, ZrO2, and CeO2: IR spectroscopic assessment of impacts of the surface acid− base properties. *Langmuir*, *17*(3), 768-774.

19. Bond, J. Q., Martin Alonso, D., West, R. M., & Dumesic, J. A. (2010). γ-Valerolactone ring-opening and decarboxylation over SiO2/Al2O3 in the presence of water. *Langmuir*, *26*(21), 16291-16298.

20. Marranca, J. T., Koenig, G., & Neurock, M. (2014). *Theoretical Insights into the Conversion of y-Valerolactone to Butene Over y-Alumina* (Doctoral dissertation, Thesis, University of Virginia).

21. Liu, J., Nan, Y., Huang, X., Bond, J. Q., & Tavlarides, L. L. (2018). Continuous esterification of oleic acid to ethyl oleate under sub/supercritical conditions over γ-Al2O3. *Applied Catalysis B: Environmental*, *232*, 155-163.

22. Farneth, W., & Gorte, R. (1995). Methods for characterizing zeolite acidity. *Chemical reviews*, *95*(3), 615-635.

23. Palkhiwala, A., & Gorte, R. (1999). Characterization of H-FER and H-TON using temperature-programmed desorption of alkylamines. *Catalysis letters*, *57*(1), 19-23.

24. Srinivasan, S., Narayanan, C., Biaglow, A., Gorte, R., & Datye, A. (1995). The role of sodium and structure on the catalytic behavior of alumina: I. Isopropanol dehydration activity. *Applied Catalysis A: General*, *132*(2), 271-287.

25. Ji, Y., Lawal, A., Nyholm, A., Gorte, R. J., & Abdelrahman, O. A. (2020). Dehydra-decyclization of tetrahydrofurans to diene monomers over metal oxides. *Catalysis Science & Technology*, *10*(17), 5903-5912.

26. Nash, C. P., Ramanathan, A., Ruddy, D. A., Behl, M., Gjersing, E., Griffin, M., ... & Hensley, J. E. (2016). Mixed alcohol dehydration over Brønsted and Lewis acidic catalysts. *Applied Catalysis A: General*, *510*, 110-124.

27. Kostestkyy, P., Yu, J., Gorte, R. J., & Mpourmpakis, G. (2014). Structure–activity relationships on metal-oxides: alcohol dehydration. *Catalysis Science & Technology*, *4*(11), 3861-3869.

28. Emeis, C. (1993). Determination of integrated molar extinction coefficients for infrared absorption bands of pyridine adsorbed on solid acid catalysts. *Journal of Catalysis*, *141*(2), 347-354.

29. Zaker, A., Guerra, P., Wang, Y., Tompsett, G. A., Huang, X., Bond, J. Q., & Timko, M. T. (2018). Evidence of heterogeneous catalytic activity of ZSM-5 in supercritical water for dodecane cracking. *Catalysis Today*, *317*, 2-11.

30. Yan, T., Liu, Q., Wang, S., Xu, G., Wu, M., Chen, J., & Li, J. (2020). Promoter rather than Inhibitor: Phosphorus Incorporation Accelerates the Activity of V2O5–WO3/TiO2 Catalyst for Selective Catalytic Reduction of NO x by NH3. ACS Catalysis, 10(4), 2747-2753.

31. Dagle, V. L., Flake, M. D., Lemmon, T. L., Lopez, J. S., Kovarik, L., & Dagle, R. A. (2018). Effect of the SiO2 support on the catalytic performance of Ag/ZrO2/SiO2 catalysts for the single-bed production of butadiene from ethanol. Applied Catalysis B: Environmental, 236, 576-587.

32. Laurent, E., & Delmon, B. (1994). Study of the hydrodeoxygenation of carbonyl, car☐ ylic and guaiacyl groups over sulfided CoMo/γ-Al2O3 and NiMo/γ-Al2O3 catalyst: II. Influence of water, ammonia and hydrogen sulfide. Applied Catalysis A: General, 109(1), 97-115.

33. Pieta, I. S., Ishaq, M., Wells, R. P. K., & Anderson, J. A. (2010). Quantitative determination of acid sites on silica–alumina. Applied Catalysis A: General, 390(1-2), 127-134.

34. Rivard, J. (2001). Kinetics of the catalytic dehydration of 2-propanol in an aqueous medium.

35. Roy, S., Mpourmpakis, G., Hong, D. Y., Vlachos, D. G., Bhan, A., & Gorte, R. J. (2012). Mechanistic study of alcohol dehydration on γ-Al2O3. Acs Catalysis, 2(9), 1846-1853.

36. Chen, G., Li, S., Jiao, F., & Yuan, Q. (2007). Catalytic dehydration of bioethanol to ethylene over TiO2/γ-Al2O3 catalysts in microchannel reactors. Catalysis Today, 125(1-2), 111-119.

37. Tanabe, K., & Yamaguchi, T. (1994). Acid-base bifunctional catalysis by ZrO2 and its mixed oxides. Catalysis Today, 20(2), 185-197.

Chapter 5

An examination of catalytic decarboxylation of γ-valerolactone over various zeolites

catalysts

5.1 Introduction

Short chain alkenes are the fundamental intermediates for producing valuable chemicals [1-4]. They are traditionally obtained from the catalytic cracking of long-chain hydrocarbons in natural gas and petroleum chemicals [5]. Butene is one of such light alkenes that can be used to produce transportation fuels or other building block chemicals such as propene [6-8]. Currently, the primary strategy to produce butene is fluid-catalytic creaking and steam cracking of liquid feed [9]. However, such approaches require fractional distillation to separate butene from other products. This process is not economical and energy-consuming. Thus, finding an alternative strategy to produce butene is demanding. Interest in using lignocellulose as an alternative source of industrial carbon has intensified in recent years [10]. And butene is found to be obtained from a series of conversion of biomass derivatives. Through hydrolysis and continuous hydrogenation, γ-valerolactone (GVL) can be produced with a high conversion from lignocellulosic biomass [11]. Butene can be further synthesized from ring-opening reaction and decarboxylation of GVL over solid acid catalysts, as figure 5.1 illustrated.

Previous reports have proved that GVL decarboxylation can have on both the Brønsted acid site and Lewis acid site [12,13]. But there are differences in the activities on these active sites. Dumesic
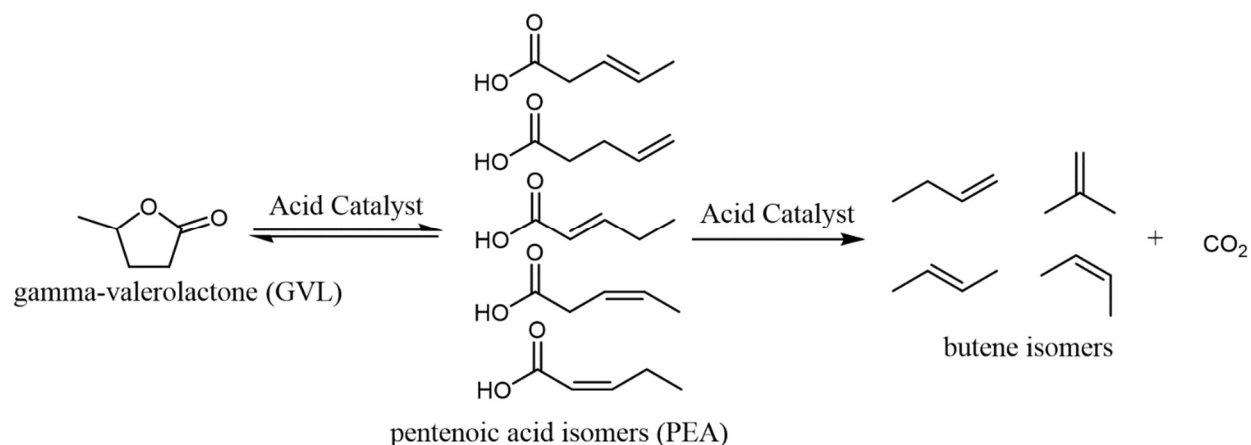
Figure 5.1: The scheme for GVL ring opening and decarboxylation to produce butene isomers over solid acid catalysts.

has shown that in the presence of water, GVL decarboxylation over γ-Al$_2$O$_3$, a Lewis acid stie abundant material, is less effective. By introducing Brønsted acid site on the catalyst surface, the butene yield can be significantly improved. However, strong deactivation is also observed as reaction time increases, hindering the long-term production of butene.

To investigate fundamental factors contributing to the activity and influencing catalysts stability, in this study, zeolites with different frameworks (MFI, FAU, BEA, FER, and MOR) are considered. Zeolites are microporous aluminosilicate with specific crystal structures. They are usually considered as Brønsted acid catalysts for isomerization, cracking, and hydrocarbon synthesis [14-21]. Aiming at a better understanding in structure and activity of zeolite catalysts for GVL decarboxylation, physical properties and acid sites distribution in MFI, FAU, BEA, FER and MOR are thoroughly characterized. Moreover, extensive kinetic data on GVL ring opening and decarboxylation over these zeolites are collected. By comparing variations in elementary kinetic parameters over various zeolites, the link between reactivity in GVL/PEA interconversion and decarboxylation and catalyst structure will be examined. Finally, the stability and regenerability of zeolites are also tested. The fundamental factors controlling the deactivation and stability of GVL decarboxylation over zeolites will be elucidated.

5.2 Materials and Methods

5.2.1 Materials

Zeolites with different frameworks (type MFI, framework type MOR, framework type, framework type BEA, framework type FER, framework type FAU) and amorphous silica-alumina were used as acid catalysts for testing GVL ring opening and decarboxylation. γ-valerolactone (GVL, >98%, Sigma-Aldrich) was used as a primary reactant in this study and was purified over molecular sieves ((5% w/v, 12–24 mesh, Strem Chemicals)) prior to use in the reactor. Tran-2-pentenioc acid (PEA, 97%, Acros), 4-Pentenoic acid (97%, Sigma-Aldrich), 3-trans-pentenoic acid, (95%, TCI America), 1-butene (1 % in Helium, Airgas), and propylene (1% in Helium, Airgas) were used as standards for instrument calibration as provided by commercial suppliers. Isopropylamine (IPA, 99%, Acros) and pyridine (>99.0%, Sigma-Aldrich) were used as probe molecules for acid site titration during TPD and FTIR experiments. They were used without further purification. Deionized water used in preparing GVL solutions, calibration standards, and HPLC mobile phases was prepared in-house by sequential reverse osmosis, UV oxidation, and double ion exchange. Helium (99.999%, Airgas), N_2 (99.999%, Airgas), and Air (Zero Grade, Airgas) were used in flow systems and chemisorption experiments without extra purification. Air used in calcination process during TPD, FTIR and catalyst preparation procedure to remove water adsorption was obtained from in-house purge gas generator (Purge gas, CO2-PG14).

4.2.2 Catalysts Preparation

Amorphous silica-alumina sample, SIAL 3113, was supplied from Grace-Davison. Prior to being packed in the reactor, ASA catalyst was calcined in airflow (100 mL/min, 4h, 723K, 3K/min) to

remove surface residues from manufacturers. In this study, this sample was referred as ASA or SIAL 3113.

Six H-ZSM-5 (framework type MFI) samples with various compositions of Silica to Aluminum ratio were considered. The lowest silicon content sample had a Si: Al ratio of 23:1. The highest silicon sample had a Si: Al ratio of 500:1. The Si: Al ratio of other MFI samples are listed in table 5.1. In this study, an H-ZSM-5 (MFI structure) with a Si: Al ratio of 23:1 will be referred as MFI 23:1. Four other zeolites samples with different framework types (MOR, FAU, BEA, FER) were also considered here. MOR, FAU, BEA, and FER stand for zeolite Mordenite, zeolite Y (Faujasite), zeolite Beta, and zeolite Ferrierite. These samples were provided by Alfa Aesar and came either

Entry	Name	Code in this paper	Si:Al
1	Zeolite ZSM-5, ammonium, 23:1	MFI 23:1	23:1
2	Zeolite ZSM-5, ammonium, 30:1	MFI 30:1	30:1
3	Zeolite ZSM-5, ammonium, 50:1	MFI 50:1	50:1
4	Zeolite ZSM-5, ammonium, 80:1	MFI 80:1	80:1
5	Zeolite ZSM-5, ammonium, 200:1	MFI 200:1	200:1
6	Zeolite ZSM-5, ammonium, 500:1	MFI 500:1	500:1
7	Zeolite Mordenite	MOR	20:1
8	Zeolite Y (Faujasite)	FAU	12:1
9	Zeolite β (Beta)	BEA	25:1
10	Zeolite Ferrierite	FER	20:1
11	Amorphous silica-alumina	ASA (SIAL 311)	5:1

Table 5.1: Chemical composition of silica alumina and zeolites samples considered in this study.

in an H$^+$ or ammonium form. Thus, except MOR, all zeolites were dried and calcined ex situ in airflow (100 mL/min, 4h, 723K, 3K/min) before packing into the reactor. For MOR, after being calcined at 723K for 4 hours, the color of zeolite power turned yellow from white, indicating incomplete calcination caused by organic residue. Therefore, the MOR was calcined in 773K for 8 hours in airflow for complete calcination. Table 4.1 illustrated the silicon and aluminum content of all materials.

5.2.3 Surface area and pore size measurements

The surface areas of ASA samples were determined by N$_2$ (99.999%, Airgas) adsorption at 77K in a surface area and porosity analyzer (Micromeritics ASAP 2020). Prior to N$_2$ dosing, approximately 100 mg of sample was outgassed under vacuum for 4h at 623K. Total surface areas were determined by Brunauer-Emmett-Teller (BET) and t-plot micropore analyses. The thickness equation model for the t-plot calculation was Harkins and Jura. The relative pressure range considered in the BET calculation was 0.05 to 0.35 saturation, and the thickness range of nitrogen multilayer considered in the t-plot was 3 to 5 Angstroms [22]. Pore volumes were characterized by nitrogen cumulation at a relative pressure of 0.995. Pore sizes were estimated by Barrett-Joyner-Halenda (BJH) analysis of the desorption branch of N$_2$ uptake isotherms [23].

For the zeolites, microporous materials, the isotherms were collected under a low-pressure incremental dosing mode, using 1-3 cm^3/g sample STP of nitrogen per isotherm point, covering relative pressure ranges from 10e-8 to 0.995 saturation. The microporosity was verified by the presence of the inflection curve at the low-pressure range of the isotherms [23]. The micro-pore size distributions and median pore widths were obtained with the Horvath-Kawazoe model modified with the Saito-Foley method for cylindrical pore geometry at the relative pressure range of 10^{-8} to 10^{-1}, and interaction parameter of 1.68×10^{43} erg.cm4. The BET surface areas were

calculated at the same pressure range as the mesoporous materials, and the t-plot micropore areas and volumes were calculated with the linear range of the thickness curve immediately after the inflection curve (typically 3.5 – 5 Angstroms). The total pore volumes of the zeolite samples were also characterized by nitrogen cumulation at a relative pressure of 0.995.

5.2.4 Temperature Programmed Desorption

Zeolites are normally treated as Brønsted acid catalysts. The Brønsted acid sites concentration in zeolites and ASA sample were determined by isopropylamine (Acros, 99%) temperature programmed desorption (TPD). Typically, 60-80 mg of powered catalysts was added into a 1/2-inch quartz tube supported by two quartz wool (Grace) end plugs. The whole tube was further placed in an Omega ceramic furnace. The temperature of the furnace was regulated by a process controller (Love, series 16A) and monitored by a type K thermocouple (Omega). All samples were calcined under airflow (50 sccm). The cell was ramped to 723K (5 K/min) and was held at 723 K for 4 hours and subsequently cooled to 423K and purged in dry Helium flow (100 sccm) for more than 90 minutes. The Helium used in TPD experiments was dried over molecular sieves. Catalysts were further dosed in isopropylamine/Helium blend that was prepared by flowing Helium through an IPA saturated chamber. After saturation of IPA on the surface, physisorbed isopropylamine was removed by applying a high Helium flowrate (400 sccm) for at least 1 hour. The furnace was then ramped to 973K (10 K/min) under Helium, including 1% Ar serving as an internal standard. Chemisorbed isopropylamine was converted into propene and ammonia after ramping. During the whole process, a mass-selective residual gas detector (Stanford Instruments RGA 100) was used to track MS signals of isopropylamine (m/z=44), propylene (m/z=41), and Ar (m/z=40) in the effluent. Evolved propylene was used to calculate Brønsted site density, assuming that one molecule of isopropylamine adsorbs per Brønsted site [24,25].

5.2.5 FTIR spectroscopy

The ratios between Brønsted acid sites and Lewis acid sites were determined by transmission FTIR spectroscopy (Nicolet 6700 DTGS detector) of adsorbed pyridine on catalysts. Approximately 20 mg of sample was press into a 13mm pellet in a hydraulic press (5 tons force). This allowed us to prepare detectable coverages of surface species and minimize gas-phase interference simultaneously. The pellet further was loaded on a home-built in-situ cell that comprised of a vacuum tee (McMaster-Carr, 1½" OD) with 4 CaF_2 windows to seal the chamber. Two ¼" tubes were welded onto both sides of the vacuum tee body and each one was equipped with a ¼" bellows valve. The setup was adjusted and positioned thus allowing the IR beam to clearly pass through. Two cartridge heaters (McMaster, 1/8" ×1 ¼") were applied as heating sources for the cell along with and a type K thermocouple (Omega) and a PID controller (Love Controls, Series 16A) to monitor and control temperature. Before acid site titration, catalysts were calcined as the pretreatment procedure described in the TPD experimental section. Subsequently, the catalyst pellet was cooled to 423K and purged under a flow of 100 sccm of Helium sccm gas that was dried by a liquid nitrogen trap followed by a moisture trap. The pellet was then dosed with 4 torrs of pyridine (Sigma Aldrich, 99%) that was introduced into the system through a stainless-steel tee packed with quartz wool. After the pellet was fully saturated, the cell was purged under a Helium flow of 200 sccm at 423K to remove physisorbed pyridine. Spectra were collected at 423K, and Brønsted to Lewis acid site ratios were calculated by the ratio of integrated IR bands at 1545 cm^{-1} and 1455 cm^{-1}, respectively with correlation for the appropriate molar extinction coefficients as equation 4.1 illustrated, where C(BAS, LAS) represented the concentration of Brønsted acid sites and Lewis acid site on the catalyst surface and IA(B, L) represents the integrated absorbance of

Brønsted acid sites and Lewis acid site in FTIR spectra respectively. All FTIR spectra involved in this sector are collected at 5-minute intervals until the signal reached steady state [26,27].

$$\frac{C(BAS)}{C(LAS)} = \frac{1.88 * IA(B)}{1.42 * IA(L)}$$

(5.1)

5.2.6 Catalytic activity testing

As figure 5.2 illustrates, the reaction system was composed of four major components: a specially designed countercurrent vaporizer to provide a stable GVL/He or PEA/He flow in the gas phase, a packed bed reactor held in a high temperature furnace to evaluate the catalytic performance, a water trap to condense and separate the liquid product when backflush method was applied in GC, an online GC to analyze gas phase composition. All components including two six port valves were heat traced and held at high temperature (150°C) to keep every product from condensing.

An up-flow packed bed reactor was applied in this study to analyze the gas phase reaction products. Catalysts were diluted with sieved silica (40-90 um) and further loaded into a half-inch 316
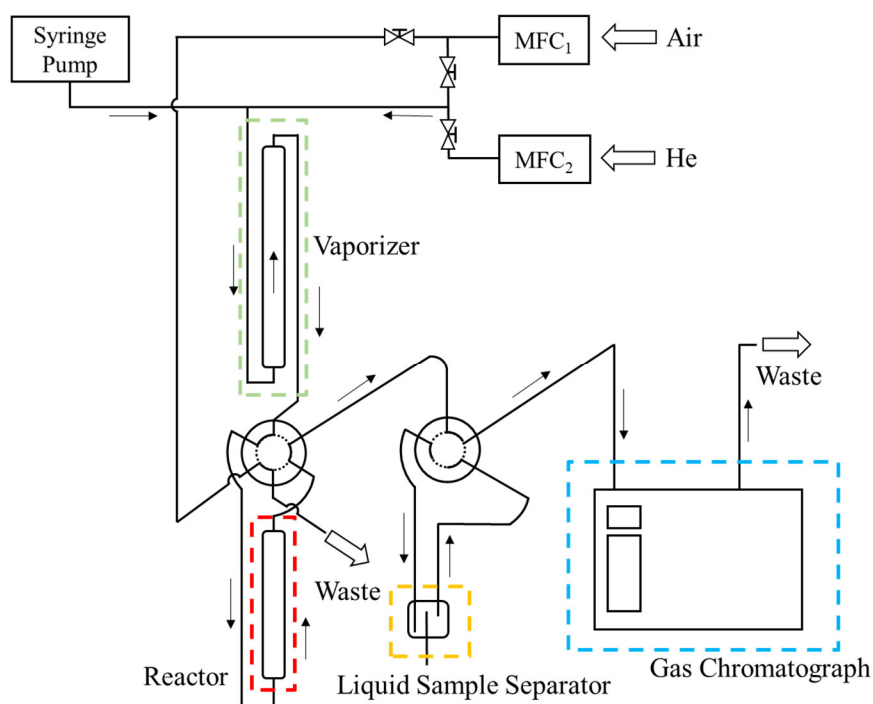
Figure 5.2: Setup of flow reactor for measuring kinetics of GVL ring opening in the gas phase environment.

stainless steel tube to prevent the considerable change in pressure across the bd. Two pieces of quartz wools were placed on both sides to hold the bed. Upstream and downstream dead volumes were filled with silica chips (850-2000 um). The reactor was mounted in a special-designed aluminum block which was placed in an insulated furnace (Applied Test System). The temperature of the furnace, as well as the vaporizer, bypass, two six port valves were controlled and monitored by several PID temperature controllers (Love controller, series 16A) with a type K thermal. An extra type K thermal couple was placed right above the catalyst bed to monitor the actual reaction temperature when the reaction occurred. The fresh catalysts were calcined in situ overnight at 723K in flowing air for 4 hours (3K/min, hold for 4h) before being exposed to reactant mixtures.

By using a syringe pump (Cole-Parmer, model 110), liquid reactants (γ-valerolactone and trans-2 pentenoic acid) were introduced into the reactor system through a peek capillary tube. The liquid reactants were further mixed with a helium flow stream, the flow of which was controlled by a mass flow controller (Brooks, model 5850S). The temperature of the vaporizer was set at 150°C in order to thoroughly vaporize the liquid GVL and PEA. Before reactants exposing to catalysts, the reactor was bypassed, and the gas mixture was redirected to GC (Agilent Technologies, GC 7890A) for 30 minutes until the GVL and Helium were thoroughly mixed. When the concentration of GVL/PEA was steady, the mixture flow was switched back to the catalysts bed. After the reaction, the composition of gas products was quantified by GC with a HP-INNOWAX column. To keep the catalyst bed regenerates to its initial state, the reactor was calcined after every activity test (100 mL/min, 4h, 723K, 3K/min). . The time of this operation is defined as zero time on stream in the following experiments since catalysts are characterized in their initial conditions.

Figure 5.3 illustrates the operation of the packed bed reactor used in this work where "a" represented one compound passing through the catalyst bed (GVL, PEA, butene or CO_2). Based on the mass balance in the PBR, we can derive the rate of reaction as equation 5.2. When the

$$-r = \frac{dF_a}{dW} \tag{5.2}$$

$$-r = \frac{\Delta F_a}{\Delta W} \tag{5.3}$$
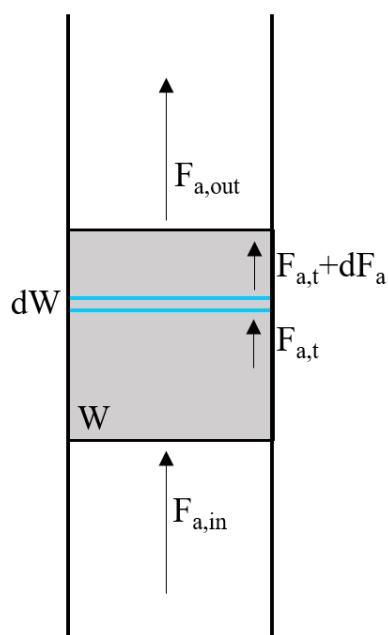
Figure 5.3: A differential catalyst segment dW across the whole catalyst bed where the flowrate of specie a changes by a differential amount dFa.

conversion of specie a is maintained below 5%, the PBR can be considered as being operated under differential conditions. Therefore, equation 5.2 is simplified to equation 5.3. In this way, the rate of reaction can be determined directly when the mass of the catalysts bed was known.

To examine the extensive kinetics and intrinsic activity of Brønsted acid sites over various acid materials, the GVL conversions were controlled under 5% for all studies. Moreover, mass normalized reaction rates and acid site-normalized rates were introduced to facilitate our understanding of reaction. Equation 5.4 defined mass normalized decarboxylation rate that was

determined by the extensive production rate of butene . The acid site-normalized rate (turn-over frequencies, TOF or site time yield, STY) was determined based on the extensive production rate normalized by the total acid sites on the catalysts surface, as equation 4.6 illustrated. Where S was the total molar quantity of Lewis acid sites in on a catalyst surface, and F_j was the molar flow rate of GVL or PEA. $C(acid\ site)$ demonstrated the Lewis acid site density determined by the isopropanol TPD described before. m_{cat} was the catalysts mass in a reactor. Rates of reaction in this study have been corrected to zero time on stream with a modified first-order model. This model will be mentioned later.

$$r_{DC} = \frac{R_{Butene}}{m_{cat}}$$
(5.4)

$$TOF_j = \frac{F_j}{S} = \frac{F_j}{C(acid\ site) \cdot m_{cat}}$$
(5.5)

5.3 Result and Discussion

5.3.1 Characterization of Materials

Table 5.2 summarizes the physical and chemical characteristics collected from N_2 adsorption, isopropylamine temperature program desorption, and pyridine FTIR for the materials of interest in this study. Complete FTIR spectra were provided in the supplementary information. The surface areas are determined with the BET method. Based on BET results, MFI structure zeolites were found to have a similar surface area between 350-380 m^2/g. The MOR and FER zeolites also had a close surface area at 395 and 363 m^2/g, respectively. Similarly, high surface areas were detected in FAU and BEA zeolites. FAU zeolite showed the highest surface area of 669 m^2/g, while BEA showed the second highest surface area of 554 m^2/g. Both materials had at least 200 m^2/g more surface area compared to MFI, MOR, and FER zeolites. ASA sample was found to have a surface area of 610 m^2/g, which was close to that of FAU.

The properties of the microporous structure were determined by the HK analysis for zeolites and BJH analysis for the ASA sample, respectively. The micropore area for MFI zeolites ranged from 222 m²/g to 305 m²/g, covering 60-70% of the total surface area. Typically, the micropore areas

Catalysts	Bet surface area (m²/g)	Micropore area (m²/g)	Pore diameter (A)	Pore volume (cm³/g)	Brønsted sites (μmol/g/cat)	B:L ratio	Lewis sites (μmol/g/cat)
MFI Structure							
MFI 23:1	355.3769	241.0335	5.271	0.222169	1118	12.7	88
MFI 30:1	353.554	248.1221	5.408	0.272383	693	9.6	72
MFI 50:1	366.9874	228.6274	5.375	0.273374	358	5.3	68
MFI 80:1	385.712	305.3218	5.461	0.258955	327	6.5	50
MFI 200:1	354.0778	222.2481	5.513	0.210851	66	1.9	35
MFI 500:1	357.8402	228.6092	5.434	0.213315	29	1.2	24
Other Structure							
MOR (20:1)	395.0576	196.22	5.752	0.280731	1123	2.5	449
FAU (12:1)	669.156	567.1412	7.431	0.48272	633	2.2	288
BEA (25:1)	554.4564	352.299	6.534	0.828762	834	1.5	556
FER (20:1)	363.6704	322.9915	5.144	0.216602	539	1.2	449
ASA							
SIAL 3113	610	0	42	0.81	164	0.5	328
SIAL 3901	420	0	45	0.61	82	0.5	164

Table 5.2: Summary of physical and chemical properties of materials considered in this study. The information of SIAL 3901 is collected from previous publication [28].

for MFI zeolites with different silicon content should be the same. For here, we considered such variations in physical properties across MFI zeolites were from uncertainty in measurement. The BEA and FER zeolites had slightly more surface than MFI zeolites. The highest micropore area was observed in FAU with 567 m^2/g, and the lowest micropore area was detected in MOR. No micropore was found in ASA samples. This agrees with the fact that ASA is mesoporous material. Meanwhile, MFI, BEA, FER, FAU, MOR zeolites are microporous materials. Moreover, MFI, MOR, FER had a similar pore diameter between 5.1 and 5.7 Å, which was lower than the pore diameter of FAU and BEA, with 7.4 and 6.5 Å, respectively. Although there was no significant difference in pore diameter and pore size in most zeolite samples, pore volumes were found to vary a lot across different materials. BEA zeolites had the highest pore volume of 0.82 cm^3/g, almost 3 times more than that in MFI zeolites and 2 times more than that in FAU zeolite. The average pore volume for MFI and FAU samples were approximately 0.25 cm^3/g and 0.48 cm^3/g, respectively. MOR and FER had a similar surface area with MFI samples. Overall, MFI, MOR, and FER zeolites have shown similar physical structure properties. The surface area, microporous surface area, pore diameter, and pore volume were relatively higher in FAU and BEA zeolites. ASA sample does not exhibit any sign of microporous property.

Table 5.2 also demonstrates the acid site distribution in these solid acids. The Brønsted acid site density was determined by isopropylamine TPD, and Brønsted to Lewis acid sites ratio was determined by pyridine FTIR. Lewis acid site was calculated by BAS density dividing the BAS: LAS ratio. There was a significant difference observed among all materials. For MFI samples, the Brønsted acid concentration increased as Si: Al ratio decreased. The highest Brønsted acid site density was detected in MFI 23:1 with 1118 μmol/g, which is 50 times more than the acid site density in MFI 500:1 with 29 μmol/g. Brønsted acid site density changed in the following order:

MFI 23:1 > MFI 30:1 > MFI 50:1 > MFI 80:1 > MFI 200:1 > MFI 500:1

Furthermore, the BAS: LAS ratio also follows the same trend. And as a result, the Lewis acid site density also changed in the order:

MFI 23:1 > MFI 30:1 > MFI 50:1 > MFI 80:1 > MFI 200:1 > MFI 500:1

This decreasing trend of Brønsted acid site density, Lewis acid site density, and BAS: LAS ratio in MFI zeolites as the Si: Al ratio increasing was not coincident. Jiang *et al*. reported that over BEA zeolites, the number of Brønsted acid sites and Lewis acid sites as well as BAS: LAS ratio decreased with increasing initial Si: Al ratio [29]. This phenomenon can be explained that when the silicon is replaced by aluminum in the zeolite framework (shown as a decrease in Si: Al ratio), a cation is required to satisfy the aluminum tetrahedron. And this cation is commonly occupied by a proton. As a result, this proton serves as a Brønsted acid site, thus exhibiting the trend that the Brønsted acid concentration increases as Si: Al ratio decreases. As for the Lewis sites, Abraham *et al*, reported that the relative intensity of the octahedral Al resonance decreases as the Si: Al ratio increases, resulting in a decreasing trend in the Lewis acid site density [30].

For other structure zeolites, the acid site densities were higher than that in MFI structures. MOR zeolites had the highest Brønsted and Lewis acid site densities with 1123 and 747 μmol/g, respectively. BEA zeolites had relatively high Brønsted and Lewis acid site densities as well. Both were detected more than 700 μmol/g. FAU and FER zeolites had a similar Brønsted acid sites level of MFI 30:1 with around 600 μmol/g. Their Lewis site densities were less than MOR and BEA but still much higher comparing to MFI zeolites. One thing needed to be mentioned here is that the Lewis acidity in zeolites was majorly ascribed to the extra-framework aluminum and irregularities in the alumina framework. Based on the information from the supplier, the Si: Al ratio for MOR,

FAU, BEA, and FER were around 20:1, which was closed to MFI 23:1. And we can see that the relationship between acid site density and Si: Al ratio still fitted here.

As a summary for this section, we found that for all types of zeolites consider in this study, the micropore surface area covers 60-70% of total surface area with a pore diameter less than 7 Å. BEA has the largest pore volume, while FAU has the highest acid site density. There were no clear relationships between the acidity of materials and surface area or pore volume. However, a trend between acidity and Si: Al ratio is observed. Across MFI, FAU, MOR, BEA, and FER zeolites, the higher Si:Al ratio leads to lower Brønsted and Lewis acid site densities in the material.

5.3.2 Surface Structure and initial screening of GVL decarboxylation

Figure 5.4 illustrates a representative plot of the decarboxylation profile of GVL as a function of time on stream. The first 10 minutes was the initial transient period where the reactant diffused into the micropores and interacts with active sites. Between 10 minutes and the next 3-4 hours, the

$$r = (R_0 - R_{ss}) \cdot e^{-k1 \cdot t} + R_{ss} \cdot e^{-k2 \cdot t} \tag{5.6}$$
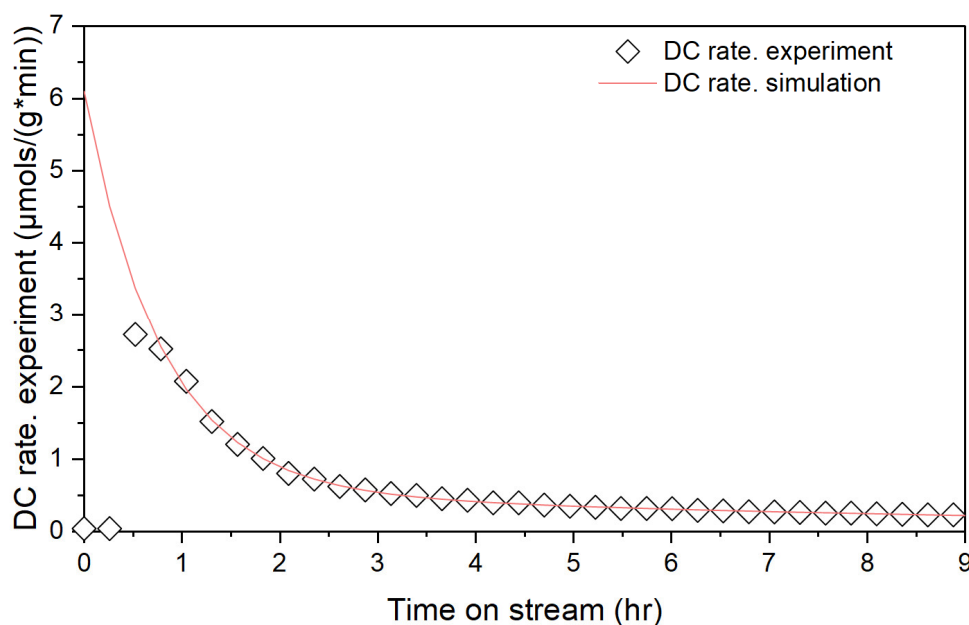
Figure 5.4: The rate of decarboxylation (butene) at a 198°C with a GVL partial pressure of 10 mbar. Solid dots represent the experimental data, and the line shows the regression of modified deactivation model.

butene can be observed and quantified to calculate the decarboxylation rate. A severe deactivation was observed during this period. For instance, at 198°C with a GVL partial pressure of 10 mbar, the decarboxylation rate decreased from 2.7 μmol/g/min to 0.2 μmol/g/min, losing almost 93% of the initial activity. After 4 hours, the catalyst became relatively stable with a mild deactivation. Comparing to previously reported GVL ring opening over ASA samples [28], the deactivation process was much more intense over zeolite samples, making it difficult to estimate the reaction rate at zero time on stream, which was defined as turnover frequency (TOF) of one material. To investigate the intrinsic activity of Brønsted acid sites in various zeolites, estimation of TOF is essential. Here, we proposed a modified first-order deactivation model to capture the rapid deactivation profile. The model was described as equation 5.6, where R_0 represented the initial rate of GVL decarboxylation and R_{ss} represented the reaction rate at the steady state after deactivation. Meanwhile, k_1 and k_2 denoted the deactivation constant at the initial condition and steady state and can be used to estimate the rate of deactivation. These parameters were obtained by minimizing the sum of squares error regression between experimental data and simulated results. The solid line in the figure represents the simulated results, showing a good agreement with experimental rates.

The estimated mass normalized initial rates for zeolites considered in the study is summarized in figure 5.5. Of the solid acids considered here, the activity of zeolite catalysts shows a higher initial activity comparing to ASA samples. MFI zeolites had the overall highest activity in GVL ring opening comparing to other structure zeolites with an average DC rate of 4.1 μmol/g/min. And the activity of MFI zeolites showed a trend of increasing as the Si: Al ratio decreasing. The highest DC rate was found in MFI 23:1 followed by MFI 30:1, achieving 10.7 and 6.6 μmol/g/min, respectively. MFI 50:1 and MFI 80:1 also had relatively high activity, approximately 3 times more
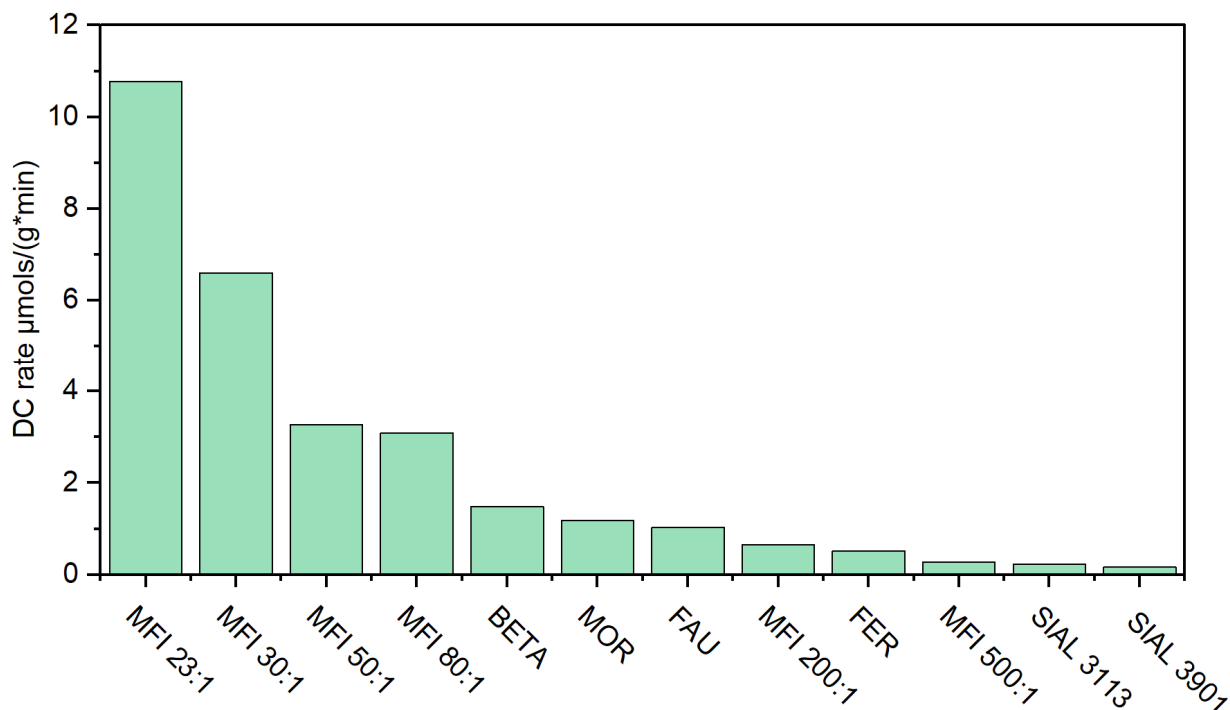
Figure 5.5: Comparison of mass normalized rates of GVL decarboxylation over various solid acids considered in this study. Reaction environments were controlled at 198°C and 10 mbar with Helium as balance gas.

active comparing to BEA, MOR, FAU and FER. MFI 200:1 and MFI 500:1 are found to be less active among tested samples. Concerning other structures, MOR, BEA, and FER represent a similar level of activity in GVL decarboxylation with 1.1 μmol/g/min. FAU has the lowest activity in GVL decarboxylation with 0.5 μmol/g/min.

Table 5.3 summarizes the physicochemical properties of zeolites and measured mass normalized rates of GVL decarboxylation at 198°C. From which we can see that across MFI samples, the increasing trend in DC rate was consistent with the rising concentration in Brønsted acid site concentrations. No clear relationship was observed between the initial decarboxylation rate and physical properties such as surface area, micropore area, pore diameter, and pore volume in MFI zeolites. For instance, MFI 23:1, which had a smaller pore volume and moderate micropore area, has the highest activity in GVL decarboxylation due to the highest Brønsted acid site density. However, this trend cannot be extended to other structure zeolites. The Brønsted acid sites in MOR

zeolite was similar to MFI 23:1, but the DC rate was 1.2 μmol/g/min, which was ten times less than the DC rate in MFI 23:1 (10.8 μmol/g/min). FAU zeolite had a double surface area and micropore area and similar acidity comparing to MFI 30:1. But the DC rate was ten times smaller. FER zeolite also had a Brønsted acid site density of 539 μmol/g/min, which doubled that of MFI 80:1. But the activity of FER zeolite was only half of the activity of MFI 80:1. The most surprising results were found in BEA zeolite, which has the highest pore volume with 0.83 cm^3/g, but its activity is only μmol/g/min. These inconsistencies indicated that the activity of zeolite is

Catalysts	Bet surface area (m^2/g)	Micropore area (m^2/g)	Pore diameter (A)	Pore volume (cm^3/g)	Brønsted sites (μmol/g/cat)	Lewis sites (μmol/g/cat)	DC rate (μmol/g/min)
MFI Structure							
MFI 23:1	355.3769	241.0335	5.271	0.222169	1118	88	10.77565667
MFI 30:1	353.554	248.1221	5.408	0.272383	693	72	6.60198
MFI 50:1	366.9874	228.6274	5.375	0.273374	358	68	3.274506667
MFI 80:1	385.712	305.3218	5.461	0.258955	327	50	3.08252
MFI 200:1	354.0778	222.2481	5.513	0.210851	66	35	0.65186
MFI 500:1	357.8402	228.6092	5.434	0.213315	29	24	0.271391667
Other Structure							
MOR (20:1)	395.0576	196.22	5.752	0.280731	1123	449	1.173535
FAU (12:1)	669.156	567.1412	7.431	0.48272	633	288	0.520066667
BEA (25:1)	554.4564	352.299	6.534	0.828762	834	556	1.032845
FER (20:1)	363.6704	322.9915	5.144	0.216602	539	449	1.48452
ASA							
SIAL 3113	610	0	42	0.81	164	328	0.235886667
SIAL 3901	420	0	45	0.61	82	164	0.158123333

Table 5.3: Summary of measured mass normalized decarboxylation rate and primary structure characteristics of solid acids considered in this study.

independent to the micropore area, pore diameter, and pore volume. Moreover, the Lewis acid site density in MOR, FAU, BEA, and FER zeolites were higher than that in MFI zeolites. For instance, MOR zeolites had ten times more Lewis acidity than MFI 30:1. However, the DC rate of MOR is five times less comparing to MFI 30:1. Previous research has demonstrated that either Brønsted or Lewis acid site is capable of catalyzing GVL decarboxylation [13]. But no clear relationship and contributions were identified. Here, we proposed that GVL decarboxylation in zeolite materials should primarily attribute to the Brønsted acidity instead of Lewis acidity. The apparent activity for GVL decarboxylation seems to be related with Brønsted acid sites only. The more Brønsted acid site will lead to a high activity for the materials. But the intrinsic activity of Brønsted acid site and its correlation with the local structure is still unclear and will be explained in the follow sections.

5.3.3 The activity of GVL decarboxylation over zeolites

To probe the intrinsic activity of Brønsted acid site in zeolite framework, we further look into the relationship between initial decarboxylation rate and Brønsted acid site density in different zeolites. Based on the critical molar volumes, the kinetic diameter of GVL is between 5 and 6 Å. This is close to the pore diameter of the zeolite sample considered in this study, which were also mostly around 5.5 Å. Therefore, diffusion limitation may be observed and interfere with the initial rate estimation when transport limitation is controlling the rate determining step comparing to elementary reactions in the catalyst. Here, Koros-Nowak criteria was introduced to evaluate the kinetic control during GVL decarboxylation over MFI zeolites [31]. Koros-Nowak criteria can be used to examine whether the observed kinetic data is free from mass or heat transport limitation based on the slope of plotting the reaction rate against site density on a log scale. A slope near 1 suggests the system is kinetically controlled. A slope more than 1 suggests the system is under

Figure 5.6: (a) Correlation of Koros-Nowark criteria for MFI framework zeolites to illustrate the kinetic control during GVL decarboxylation at 198℃. (b) Illustration of the relationship between mass-normalized decarboxylation rates and Brønsted acid sites over MFI samples with different aluminum content at 198℃ and 10mbar GVL with Helium as balance △

heat transport limitations, and a slope less than 1 suggests the system is under mass transport limitation. Figure 5.6a illustrates the decarboxylation rate in MFI at 198℃ as a function of Brønsted acid site density of different MFI samples on a log scale. The linear regress of this data set showed a slop of 1.008 with a R^2 of 0.997, suggesting the GVL decarboxylation under such environments were strictly under kinetic control, and the decarboxylation rates over zeolites exhibit a first order dependence on the Brønsted acid site density. Therefore, the rate we measured can be used to reflect the intrinsic activity of the Brønsted acid site in zeolites. Figure 5.6b demonstrates the linear relationship between DC rates and Brønsted acid site density. The slope of 0.57 hr^{-1} indicates the average turnover frequency of MFI zeolites. Moreover, the zero intercept implies that in the MFI zeolites, no decarboxylation activity will be detected if there is no Brønsted acid site in the material. Therefore, we can prove that Brønsted acid site is essential for GVL decarboxylation. Also, this further proved our previous proposal that the GVL decarboxylation is independent with Lewis acid sites in the MFI zeolites.

To examine the strength of Brønsted acid site at other reaction conditions, we extend our activity to a wide range of temperatures. Previous, Aimee *et al* reported that under 350°C, the GVL decarboxylation would be limited by the transportation phenomena. In this study, to avoid transportation limitation, the temperature we considered is from 178°C to 258°C, and the results are demonstrated in Figure 5.7. The regression of temperature data set at 178°C, 198°C and 218°C showed a slope of 1.02, 1.00 and 1.01 respectively, indicating in such conditions, the GVL ring opening was strictly under kinetic control. As temperature rises to 238 °C, the slope decreases to 0.7221, exhibiting a sign of transportation limitation. Considering the microporous properties of zeolites, the internal diffusion may be the rate determining step at high temperature regions, thus influencing the decrease in the reaction rate measured. Meanwhile, at low temperature regions, the reaction shift towards kinetic control. Overall, the Brønsted acid site was the primary active site

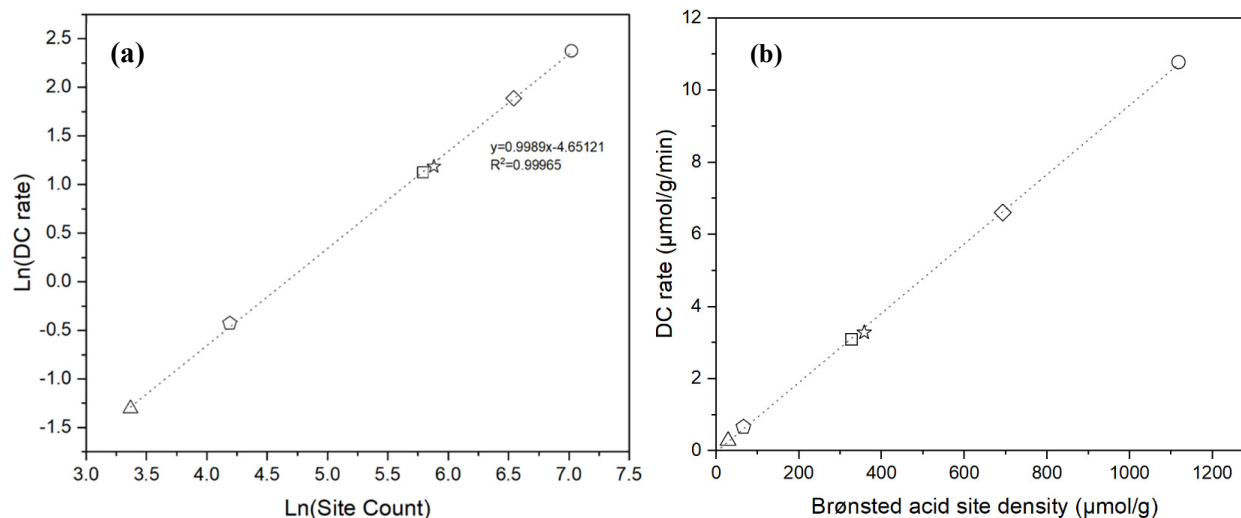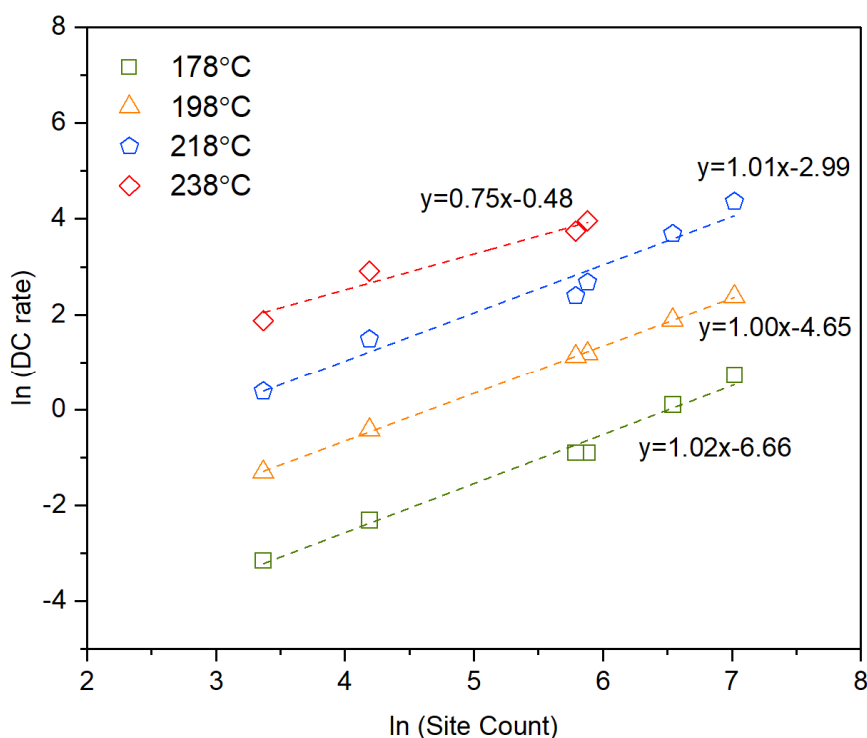Figure 5.7: Correlation of Koros-Nowark criteria for MFI framework zeolites to illustrate the kinetic control during GVL decarboxylation at 178°C, 198°C, 218°C and 238°C at 10 mbar GVL with Helium as balance gas.

Figure 5.8: Comparison of initial turnover frequencies of GVL decarboxylation over various solid acids considered in this study. Reaction environments were controlled at 198°C and 10 mbar with Helium as balance gas. All rates were collected under kinetic control as previously demonstrated.

for GVL ring opening over MFI structure zeolite. The intrinsic activity of the Brønsted acid site across MFI framework zeolites were identical, independent with Brønsted acid site density.

Given that we do not have other structure zeolite with different Si: Al ratio, Koros-Nowak test cannot be implemented here to examine extent of kinetic control here. Based on the results from last section, we assumed that the decarboxylation rate for FAU, FER, BEA and MOR at 198°C were under kinetic control and can be used to reflect the intrinsic acidity of Brønsted acid stie in such materials. Figure 5.8 summarizes the initial turnover frequencies of GVL decarboxylation at 198°C over solid acid we considered. We found that MFI samples show an average TOF of 0.57 hr^{-1}, five times more than the activity of Brønsted acid site in other solid acids. BEA, FAU, MOR, and FER zeolites had a similar TOF around 0.1 hr^{-1}, which is closed to the activity of Brønsted acid site in the ASA samples. Considering the structural information, the Brønsted acid site density in BEA, FAU, MOR and FER are much higher comparing to MFI 200:1 and MFI 500:1. But their

TOF of GVL decarboxylation is significantly lower. This indicates that zeolites framework has a remarkable influence on the strength of Brønsted acid site and a significantly high activity for GVL ring opening is observed on MFI zeolite.

5.3.4 The kinetic effects of various acid site strength

To further probe the unique activity in MFI structure, figure 5.9 demonstrates the Arrhenius plots made for six zeolite catalysts: MFI 23:1, MFI 50:1, FAU, FER, BEA, and MOR zeolites. Arrhenius plots for other MFI zeolites are similar to MFI 23:1 and MFI 50:1. Thus they are omitted here. For MFI samples, the kinetic control at this temperature region is guaranteed by the Koros-Norwalk test mention in the previous sector. Meanwhile, Arrhenius plots for FAU, FER, BEA and MOR zeolites show an excellent linear relationship between TOF of GVL decarboxylation temperature,
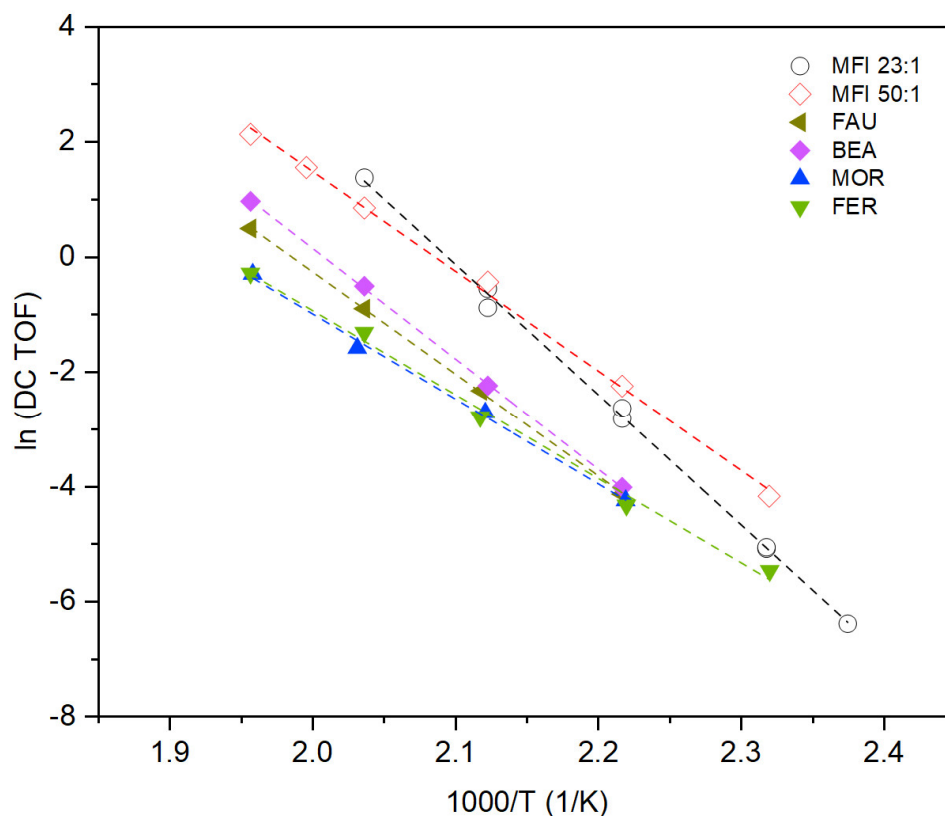
Figure 5.9: Arrhenius plots illustrating the temperature dependence of GVL decarboxylation over MFI 23:1, MFI 50:1, FAU, BEA, MOR, and FER. The unit of DC turnover frequency is hr^{-1}. Other MFI with different aluminum content had a similar relation like MFI 23:1 and MFI 50:1, thus we did not plot here.
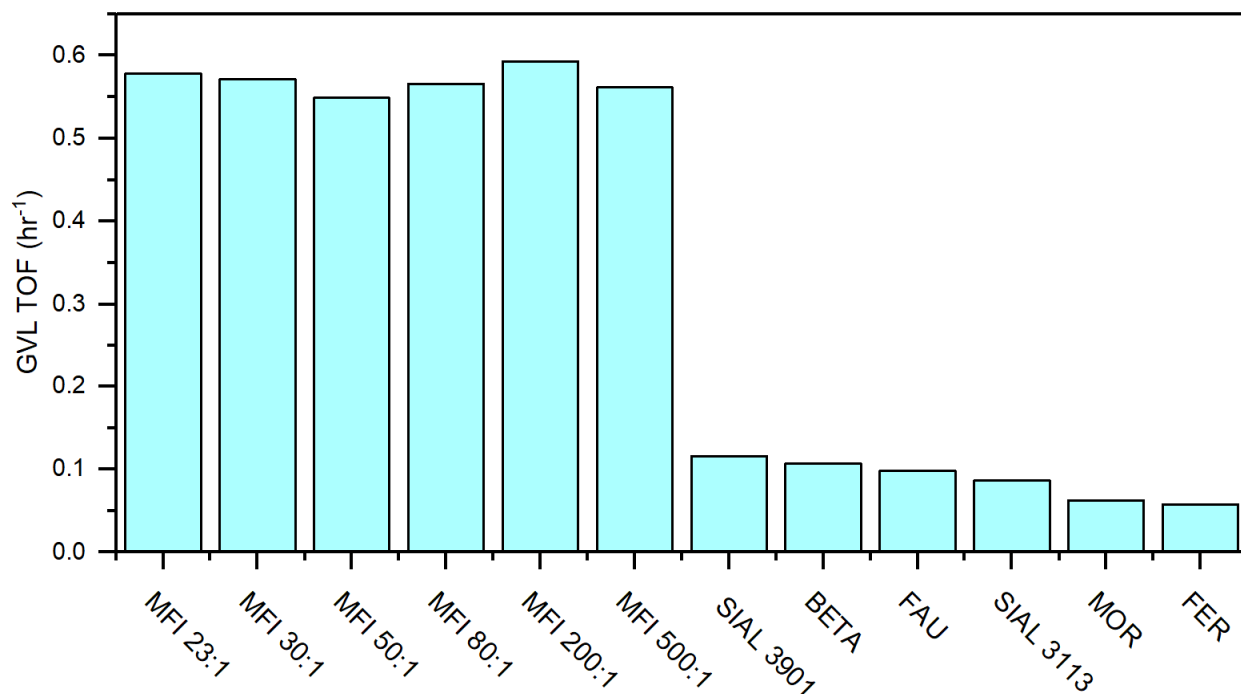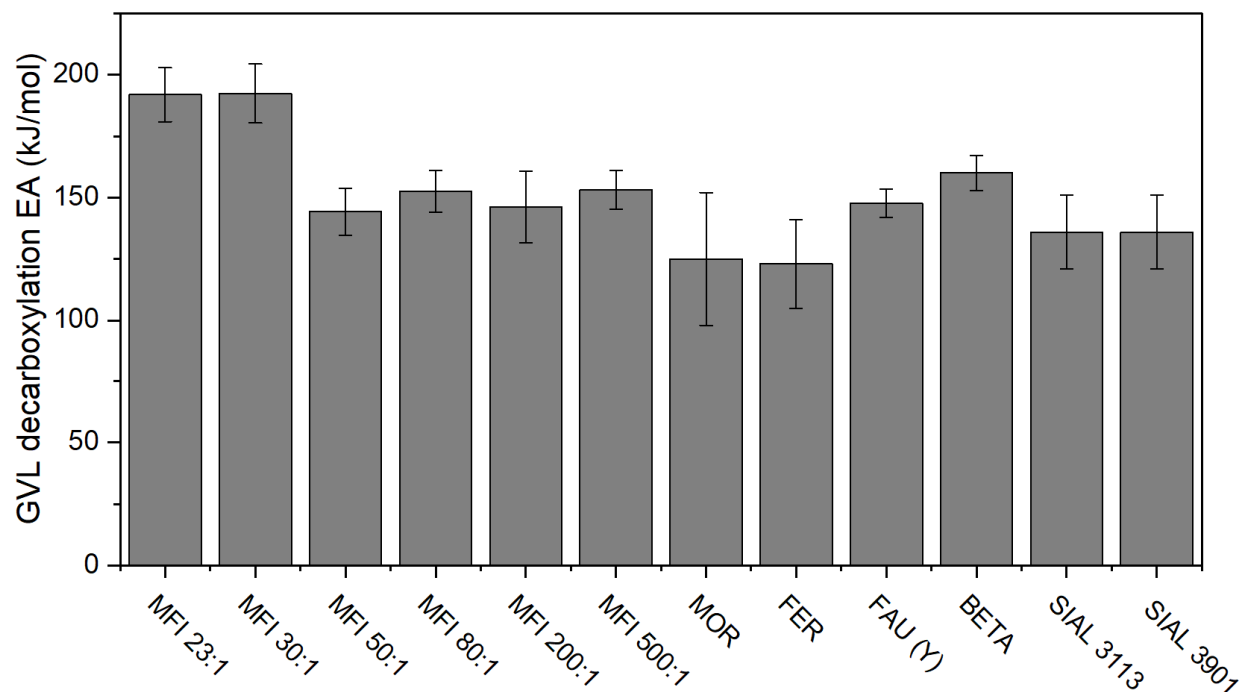
Figure 5.10: Comparison of apparent barrier of GVL decarboxylation over various solid acids considered in this study. Reaction environments were controlled at 10 mbar with Helium as balance gas.

Catalyst	A (hr^{-1})	GVL decarboxylation EA (kJ/mol)	CI	DC TOF (hr^{-1}) at 198°C
MFI 23:1	7.8E+20	191.9	11	0.5783
MFI 30:1	2.4E+21	192.4	12	0.5716
MFI 50:1	5.0E+16	144.3	9.6	0.5488
MFI 80:1	4.4E+16	152.5	8.5	0.5656
MFI 200:1	1.3E+16	146.2	14.5	0.5926
MFI 500:1	5.4E+16	153.2	7.9	0.5615
MOR	2.9E+12	125	27	0.0627
FER	2.1E+12	123	18	0.058
FAU (Y)	2.2E+15	147.8	5.8	0.0979
BETA	6.1E+16	160	7	0.1068
SIAL 3113	7.8E+20	136	15	0.0863
SIAL 3901	2.4E+21	136	15	0.1157

Table 5.4: Summary of Arrhenius parameters regressed for various solid acid considered in this study. Initial turnover frequencies were collected under kinetic control and 198°C and 10 mbar with Helium as balance gas.

suggesting that the reaction rate obtained here were also under kinetic control. This result again supports our observation has Brønsted acid sites in MFI zeolites had a remarkable higher activity comparing to that in FAU, FER, BEA and MOR.

The apparent barriers are summarized in figure 5.10 and pre-exponential factors, TOFs, and decarboxylation barrier are also concluded in the table 5.4. The kinetic parameters presented here are all apparent features and results from a combination of effects from several elementary reactions. No microkinetic modeling is covered in this study. This topic will be resolved in future work. Figure 5.10 shows that MFI 23:1 and MFI 30:1 had the highest decarboxylation barrier of 191.9 and 192.4 kJ/mol, respectively, which does not follow the trend that they have the highest intrinsic activity of Brønsted acid site. This may attribute to the diffuse limitation at high temperatures due to the high concentration of Brønsted acid site in these MFI zeolites. Other MFI zeolites, such as MFI 50:1, MFI 80:1, MFI 200:1 and MFI 400:1 had an almost identical decarboxylation barrier around 146 kJ/mol. This result agrees with the reported value of 138 kJ/mol [32]. The decarboxylation barrier for FAU zeolites (147.8 kJ/mol) was close to that of MFI zeolites with high Si: Al ratio. BEA zeolites had an almost 15 kJ/mol higher decarboxylation barrier of 160 kJ/mol. As for MOR zeolites and FER zeolites, the decarboxylation barriers are 20 kJ/mol lower than the average barrier in MFI zeolites, with 125 and 123 kJ/mol. Considering the uncertainty in the measurement of barrier, except for MFI with low aluminum content (23:1 and 30:1), we can say that MFI, FAU, MOR, BEA and FER zeolites have a similar apparent decarboxylation barrier around 140-150 kJ/mol.

This result is consistent with the deprotonation energy of these materials. According to several reports [33-36], the intrinsic strength of Brønsted acid site in zeolite is commonly determined by the deprotonation energy (DPE), which represents the energy required to cleave the O-H bond.

DPE values cannot be measurement from experiments but can be acquired through periodic density functional theory models. Jones *et al* from Iglesia`s group further found that the deprotonation energy is insensitive to framework structure or proton location of zeolites. The deprotonation energies for MFI, BEA, MOR, FAU, and FER zeolites are indistinguishable around 1201 ± 11 kJ/mol after correction [33]. Thus, the reaction barrier for zeolites with different frameworks is supposed to be similar, which agrees with our observation.

Figure 5.11 illustrates the desorption profile of propene during the isopropylamine TPD. Besides the Brønsted acid site density which was calculated based on the area of the propene peak, the desorption temperature of propene can also be used to evaluate the strength of the acid site. In the TPD technique, the peak at the low temperature region is commonly ascribed to a weak acid site. In contrast, the peak at high temperature indicates a strong acid site [37-41]. Based on our IPA-TPD results, MFI 23:1 has the highest desorption peak temperature of 400°C. And the FAU has the lowest desorption peak of 360°C. Most propene desorption temperature falls in the range
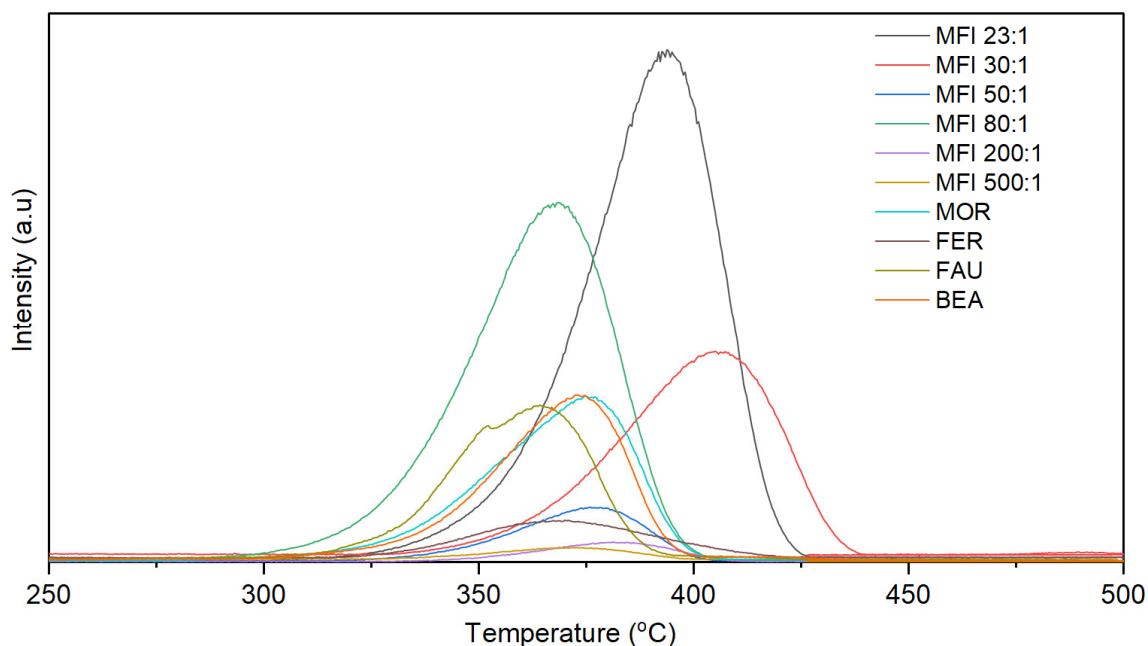
Figure 5.11: Temperature programmed desorption of isopropylamine analysis of Brønsted acidity over the solid acids considered in this study. The peaks correspond to the propene (m/z=41) emitted on the catalysts surface were used to quantify the Brønsted acid strength.

between 360 and 370℃, which is an insignificant difference, supporting our idea that the Brønsted acid site strength should be similar.

Figure 5.12 & 13 illustrates the FTIR spectra of pyridine of zeolites with different framework structure. The peak shows the pyridine adsorption after saturating and purging catalyst surface with pyridine as probe molecule. The peak at 1545 cm^{-1} attribute to Brønsted acid site due to the formation of the pryridinuim ion, while the peaks at 1455 cm^{-1} ascribe to Lewis acid site due to XXX. The size of the peak can be used to quantify the density of acid site, and the wavenumber can be used to indicate the strength of acid site. Normally, the peak at smaller wavenumber represents a weaker interaction between pyridine and surface site, indicating a weaker Lewis sites [42-44]. According to the spectra we collected, there is still no significant variation being observed near 1545 cm. This again supports our deduction that the strength of Brønsted acid site between zeolites should be independent with the framework of zeolites.
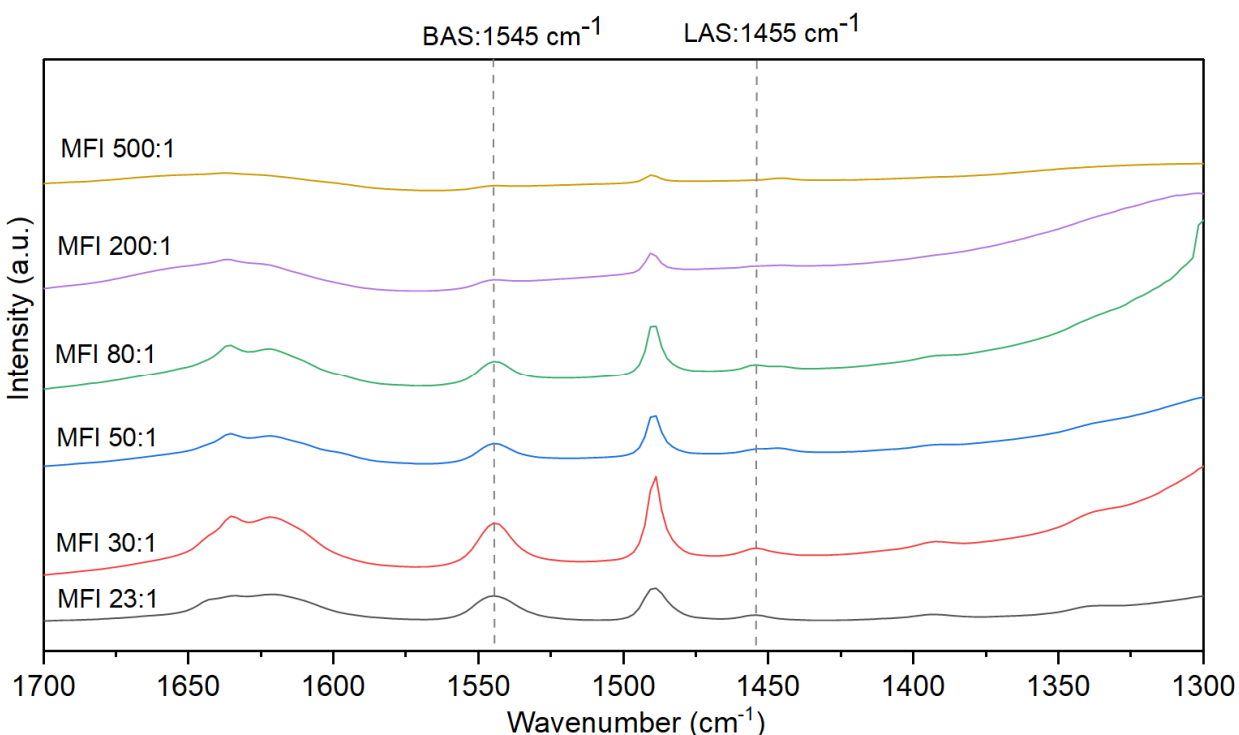
Figure 5.12: FTIR spectra of pyridine adsorption over MFI framework zeolite with different aluminum content between 1300 cm^{-1} and 1700 cm^{-1}.
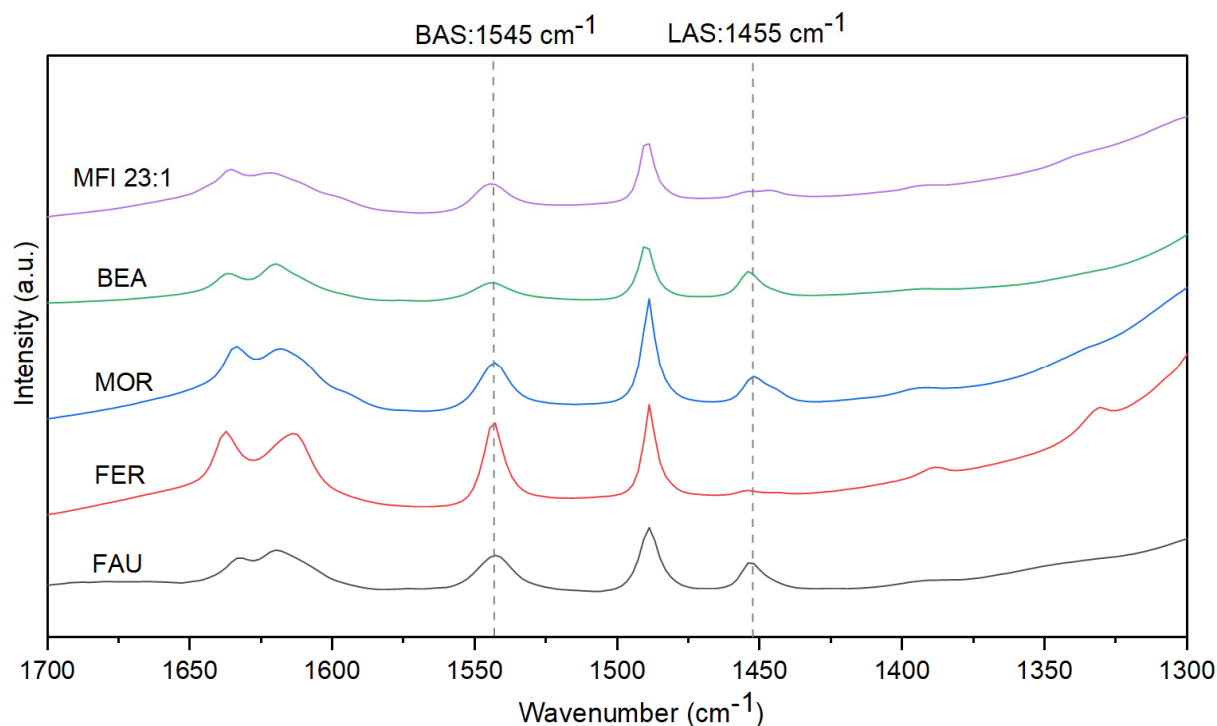
Figure 5.13: FTIR spectra of pyridine adsorption over zeolites with different framework: MFI, BEA, MOR, FER and FAU between 1300 cm^{-1} and 1700 cm^{-1}.

Even though the barrier is controlled by the deprotonation energy of zeolites and the strength of Brønsted acid site is similar, the decarboxylation activity cannot be reflected by the either characteristics. MFI 23:1 and MFI 30:1 have the highest barriers above 190 kJ/mol, but their TOFs are similar to other MFI zeolites with 0.57 hr-1. Moreover, MOR and FER zeolites have the lowest barrier around 120 kJ/mol, but their TOFs are smallest comparing to other zeolites with higher barriers. FAU and BEA zeolites have a similar barrier with MFI zeolites. In contrast, their TOFs are five times less than TOFs of MFI zeolites. These inconsistencies support our idea that the intrinsic activity of zeolites is not correlated with apparent barrier of GVL decarboxylation. Instead, the difference in TOFs can be partially related to the magnitude of pre-exponential factor. The pre-exponential factors of MOR and FER zeolites are four orders less than that of MFI zeolites. However, pre-exponential factor requires future microkinetic modeling to have a rigorous explanation. Here, the effect is still unclear.

In this study, we propose two possible explanations for the high turnover frequency observed in MFI zeolite. First, the location of the Brønsted acid site in the MFI structure may influence the intrinsic activity of GVL decarboxylation. Zeolite's framework is comprised of different tetrahedral sites (T sites), which determines the Al or proton location in the channel. The deprotonation energy is proved to be sensitive to the Al and proton positions, influencing the activity of acid site in zeolites. MFI zeolite has 12 types of T sites, which is the most compared to other framework zeolites considered in this study. BEA zeolite has 8 T sites, while both FER and MOR zeolites have 4 T sites. Only 1 T site was observed in FAU zeolite. The high GVL decarboxylation turnover rates may attribute to the unique T sites only existed in the MFI framework. Furthermore, the confinement effect may also increase the activity of GVL decarboxylation in MFI zeolite. Due to the microporous property of zeolites, reactants may face a confinement effect when diffusing across the channel. The confinement effect does not have an influence on the Brønsted acid strength. Instead, it may increase the turnover rate by stabilizing the ion-pair transition states or adsorbed intermediates [45]. Carr *et al*. has reported that the confinement effects in BEA zeolites improve the turnover rate of methanol dehydration by stabilizing the transitional state of intermediates [46]. Also, a recent report announced that the strongest confinement effect observed the pore size of zeolite fits adsorbate. In our situation, MFI zeolite has a relatively small pore diameter and pore volumes. Also the diameter of GVL is most similar to the pore diameter of MFI zeolites at 5.5 A. The confinement effects in MFI zeolite should be the strongest, increasing the turnover rate of GVL decarboxylation. The rigorous proof of these assumptions still requires further microkinetic modeling.

5.3.5 Stability of zeolites

As previously illustrated, the deactivation of GVL decarboxylation is severe and 70% of initial activity was lost in the first 30 minutes. It is necessary to examine the factor contributing most to the deactivation and the extent of regeneration of zeolites. Figure 5.14 demonstrates the activity of MFI zeolites considered in this study as a function of time on steam. The activity of GVL decarboxylation, a, is defined as the instant decarboxylation rates normalized by the initial decarboxylation rate at zero time on stream. Over MFI samples, the deactivation of GVL decarboxylation is consistent with the change of Si:Al ratio. For instance, MFI 23:1 lost 80% of original activity in the first 30 minutes and 95% after reaching a steady state. As Si: Al ratio increases from 23:1 to 50:1, the deactivation became slightly milder. MFI 50:1 lost 50% of original activity in the first 30 minutes. But after reaching steady state, it still lost almost 80% of original activity. MFI 500:1 is found to have the least deactivation. Only 20% activity is lost in the initial
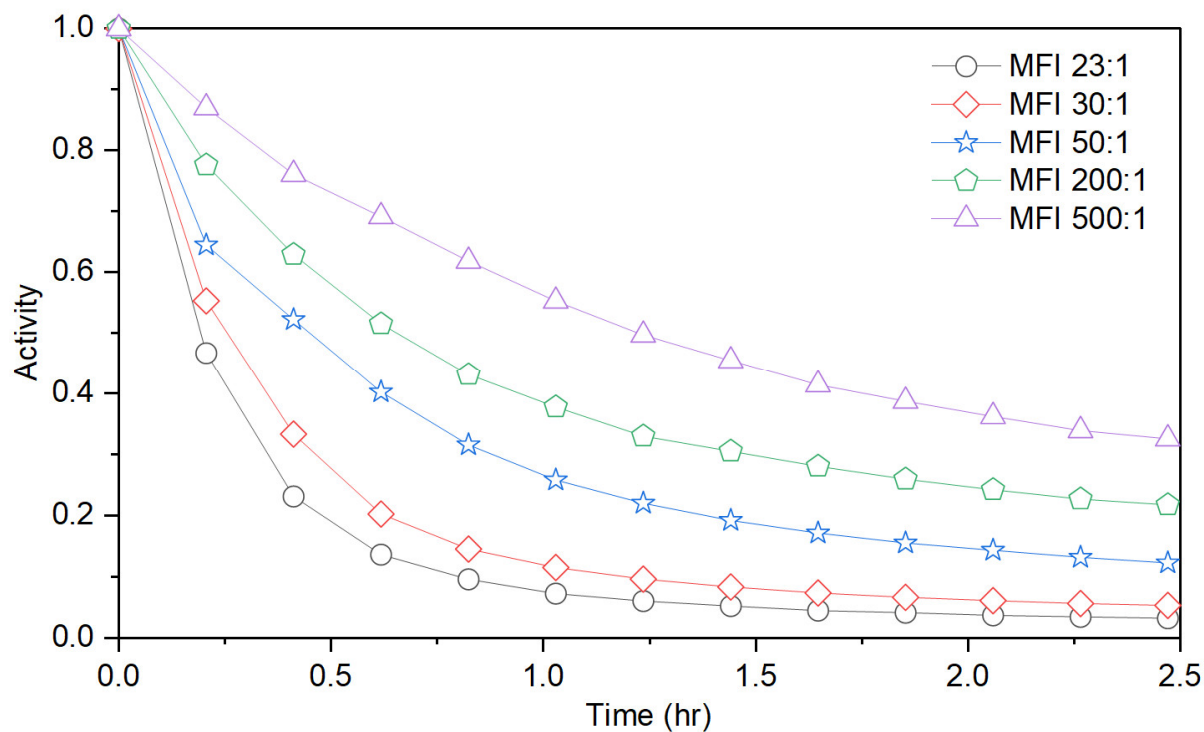

Figure 5.14: Deactivation profile of MFI framework zeolites with different aluminum content as function of time on stream at 198°C and 10 mbar GVL with Helium as balance gas.

30 minutes, and 60% activity is lost after reaching a steady state. The catalysts stability follows the following trend: MFI 23:1 > MFI 30:1 > MFI 50:1 > MFI 80:1 > MFI 200:1 > MFI 500:1. Considering the similar physical structure of MFI zeolites, the deactivation seems to be independent with pore diameter, pore volume and microporous surface area. The only factor influences the deactivation of the MFI catalyst is Brønsted acid site density, which is the result of changes of the Si: Al ratio. The shape of zeolites turned from white powder to brown or dark residues, indicating coking is the primary reason for deactivation. A higher Brønsted acid site density does not influence the turnover rate of GVL decarboxylation on active sites, but it leads to an increase in the production rate of PEA and butene. Thus, more molecules can be observed in the channel of zeolites with higher Brønsted acid site density, resulting in a higher possibility of coking and correspondent deactivation.

Figure 5.15 illustrates the deactivation of other framework zeolites as a function of time on stream. All zeolites with different frameworks exhibited a strong deactivation over time with at least 48% loss of initial activity after reaching a steady state. MFI 23:1 zeolite was found to have the most rapid deactivation. Its activity lost 66% in the first 30 minutes and 96% after 3 hours. FER zeolites had a relatively high deactivation with 34% in the first 30 minutes. MOR and BEA zeolites have a moderate deactivation around 25% lost in activity. The least deactivation was observed in FAU zeolite, which only lost 10% activity in first 30 minutes and 48% after 3 hours. These observations suggest that pore diameter and micropore area instead of surface acidity seem to influence most on the stability of zeolites. For example, FAU zeolites has the largest pore diameter of 7.4A and the largest micropore area of 669 m^2/g with the lowest GVL decarboxylation rate, and accordingly, it has the slowest deactivation comparing to other materials. BEA zeolite has the highest pore
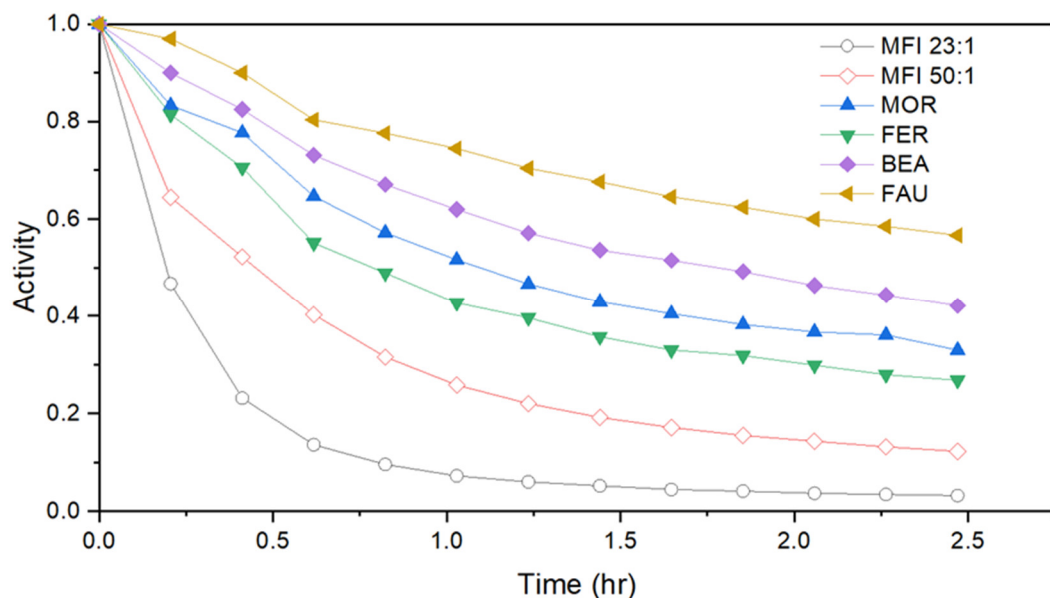
Figure 5.15: Deactivation profile of different framework zeolites MFI, FAU, BEA, FER, and MOR as function of time on stream at 198°C and 10 mbar GVL with Helium as balance gas.

Catalysts	Bet surface area (m²/g)	Micropore area (m²/g)	Pore diameter (A)	Pore volume (cm³/g)	Brønsted sites (μmol/g/cat)	Lewis sites (μmol/g/cat)	DC rate (μmol/g/min)	Activity lost in 30 minutes	Activity lost in 120 minutes
MFI 23:1	355.3769	241.0335	5.271	0.222169	1118	88	10.77565667	66.70%	96%
MOR	395.0576	196.22	5.752	0.280731	1123	449	1.173535	22.30%	69.60%
FAU	669.156	567.1412	7.431	0.48272	633	288	0.520066667	10%	48.30%
BEA	554.4564	352.299	6.534	0.828762	834	556	1.032845	27.50%	62.60%
FER	363.6704	322.9915	5.144	0.216602	539	449	1.48452	34.40%	76.00%

Table 5.5: Summary of activity lost for zeolites with different frameworks and relevant physicochemical properties.

volume of 0.82 cm/g, double that in FAU. However, its activation was twice faster than the latter, suggesting that pore volume should not be the dominant factor that controls the deactivation. Also, the Brønsted acid site in MOR and BEA are close that in MFI 23:1, but their deactivation rates were 3 times slower than deactivation of MFI 23:1. This again supports our idea that acidity should be the most significant factor contributing to deactivation. The explanation of such trend is that when coking is occurring in the zeolites with more pore diameter and micropore area, there are most accessible entrances and channels for reactant and product the transport through. The materials with lower pore diameter tend to block much easier comparing to materials with higher pore diameter. Especially considering that the diameter of GVL molecule is around 5.5A, which

is close to the pore diameter of MFI zeolites and only slightly less than that of FAU. Thus, a small extent of coking in the channel will block the movement of GVL molecule across the zeolites to reach active sites. The trapped reactant and product molecule in the channel will further aggregate the deactivation.

Finally, to test whether zeolites can be regenerated after removing the coking formation on the catalyst surface, five catalytic cycles were performed with in-situ calcination in airflow at 450C for 4 hours. Figure 5.16 demonstrates the catalytic activity of MFI 30:1 as a function of time on stream at 198°C in each catalytic cycle. The results showed that the MFI 30:1 can be completely regenerated following each calcination procedure. The initial GVL decarboxylation rate for zero time on stream was found to be indistinguishable to that of fresh catalysts after first regeneration circle. Even after 5 cycles of regeneration, no significant difference was found in the activity of
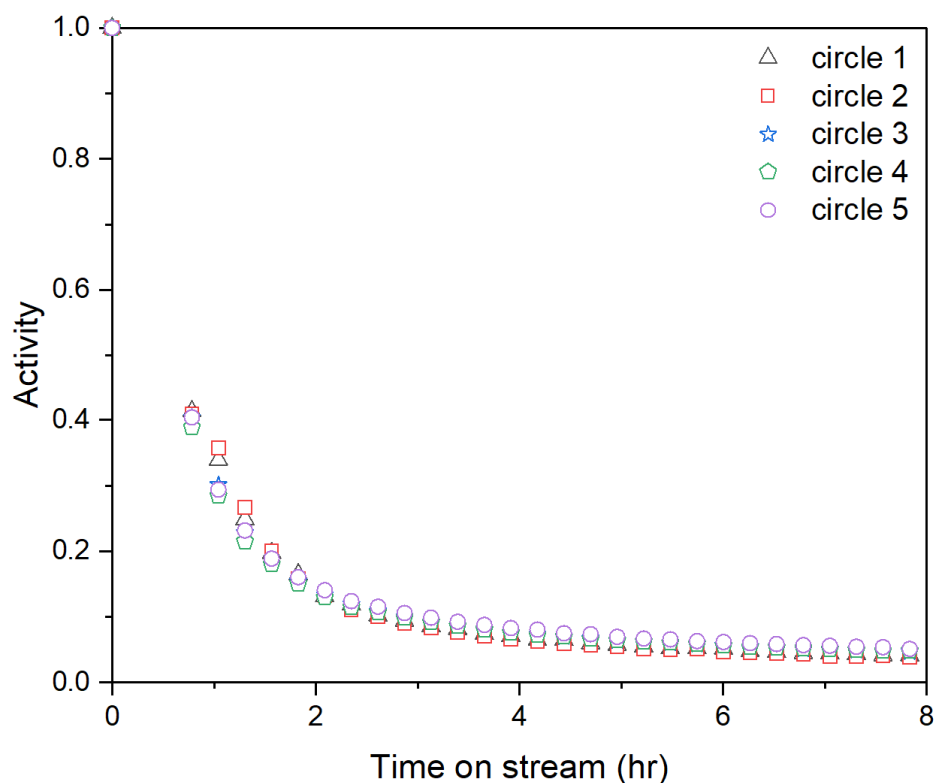

Figure 5.16: Deactivation profile of MFI 30:1 with time on stream on a fresh sample of zeolite 30:1, followed by multiple calcination circles at 450°C in airflow. The reaction condition was controlled at 198°C and 10 mbar GVL with Helium as balance gas.

MFI 30:1. This observation was consistent with our deduction that coking was the primary factor for deactivation. And this result also supported our previous measurement of decarboxylation rate was under kinetic control, free from the influence of catalyst deactivation and regeneration.

5.4 Conclusion

In this study, a wide range of zeolites with different framework is well characterized. MFI framework zeolite has a small micropore area, pore diameter and pore volume comparing to other frameworks. The Brønsted acid site density, Lewis acid site density and BAS: LAS ratio increase as the aluminum content decreases in zeolites. MFI zeolites show a slight Lewis acidity. Meanwhile, MOR, FAU, BEA and FER zeolites have a relatively high Lewis acidity. GVL decarboxylation is primarily catalyzed over Brønsted acid site. Lewis acid site has a trivial contribution to the GVL decarboxylation in the gas phase. MFI zeolites have the highest activity in GVL decarboxylation. However, the apparent barriers did not reflect the intrinsic activity of a Brønsted acid site. For example, MFI 23:1 had a higher barrier comparing to MFI 50:1 but their turnover rates of GVL decarboxylation are indistinguishable. The identical deprotonation energy of Brønsted acid in different frameworks, the similar desorption temperature of propene peak during IPA TPD and the same interaction frequency of adsorbed pyridine during FTIR all suggest that the Brønsted acid strength in zeolites with different framework should be identical. Therefore, other factors may contribute to the high intrinsic activity of MFI framework zeolites. Here, we proposed that the confinement effect and the local environment of Brønsted acid site in the MFI zeolites may influence the intrinsic decarboxylation activity. Further microkinetic modeling is essential for rigorously interpreting our observation.

Moreover, GVL decarboxylation undergoes severe deactivation over all types of zeolites. Although MFI zeolites has the highest activity in reaction, it also suffers from the most rapid

deactivation. Pore diameter and microporous area are the most significant factors influencing deactivation. Generally, a large pore diameter and large microporous area can relieve the extent of deactivation. However, a large pore diameter decreases the confinement effect, which may decrease the intrinsic activity of solid acids. Also, a large micropore area can lead to transport limitation at high temperatures. Additionally, Brønsted acid density also partially contribute to the deactivation. Furthermore, the deactivation of zeolites can mostly ascribe to coking formation. Although the zeolites lost at least 50% of initial activity after reaching a steady state, this deactivation is reversible, and zeolites can be fully regenerated by calcination.

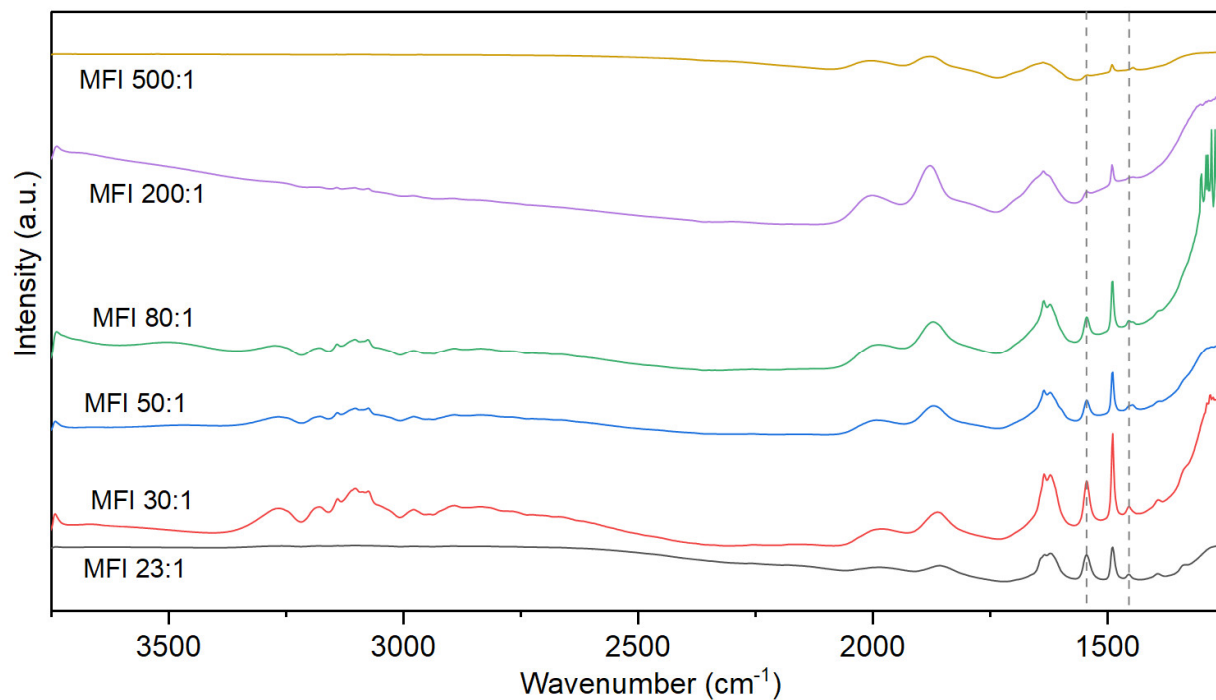## 5.5 Supplementary information

Figure S5.1: Complete FTIR spectra of pyridine adsorption over MFI framework zeolite with different aluminum content.
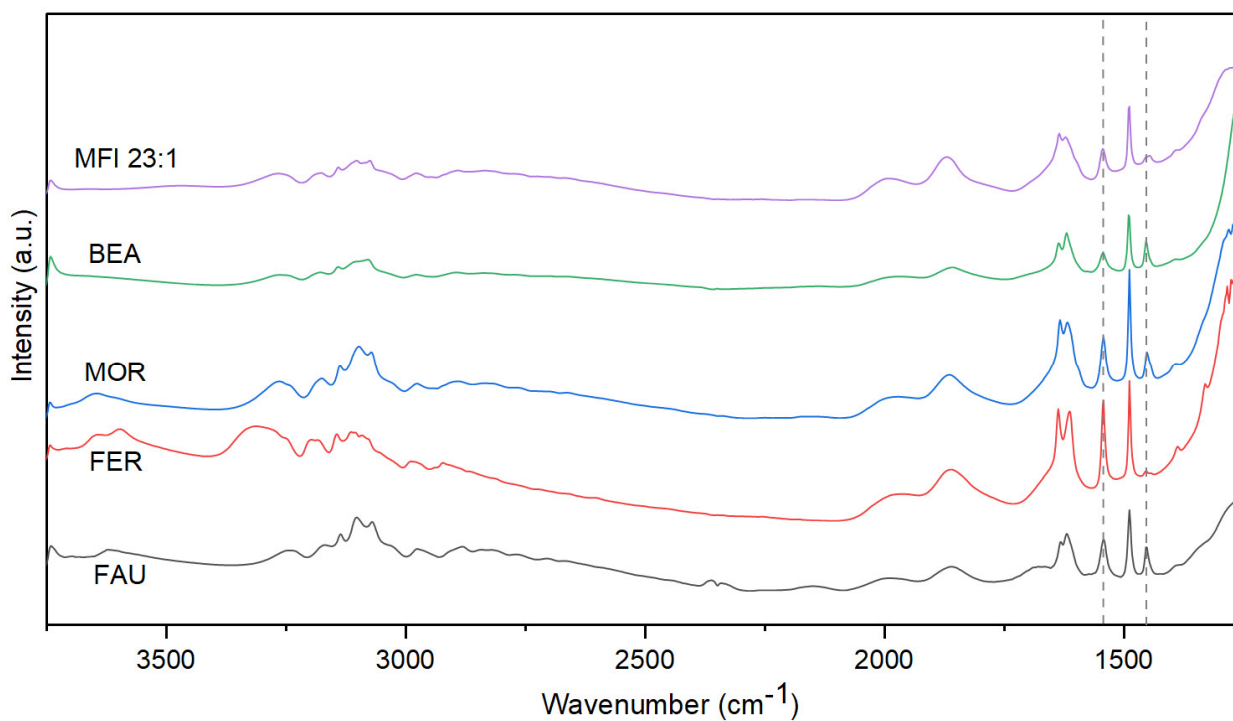

Figure 5.2: Complete FTIR spectra of pyridine adsorption over zeolites with different framework: MFI, BEA, MOR, FER and FAU.

5.6 References

1. Ren, T., Patel, M., & Blok, K. (2006). Olefins from conventional and heavy feedstocks: Energy use in steam cracking and alternative processes. *Energy*, *31*(4), 425-451.
2. Cespi, D., Passarini, F., Vassura, I., & Cavani, F. (2016). Butadiene from biomass, a life cycle perspective to address sustainability in the chemical industry. *Green Chemistry*, *18*(6), 1625-1638.
3. Grubbs, R. H., & Chang, S. (1998). Recent advances in olefin metathesis and its application in organic synthesis. *Tetrahedron*, *54*(18), 4413-4450.
4. Ittel, S. D., Johnson, L. K., & Brookhart, M. (2000). Late-metal catalysts for ethylene homo-and copolymerization. *Chemical Reviews*, *100*(4), 1169-1204.
5. Bender, M. (2014). An overview of industrial processes for the production of olefins–C4 hydrocarbons. *ChemBioEng Reviews*, *1*(4), 136-147.
6. Wright, M. E., Harvey, B. G., & Quintana, R. L. (2008). Highly efficient zirconium-catalyzed batch conversion of 1-butene: a new route to jet fuels. *Energy & fuels*, *22*(5), 3299-3302.
7. Bhuiyan, T. I., Arudra, P., Akhtar, M. N., Aitani, A. M., Abudawoud, R. H., Al-Yami, M. A., & Al-Khattaf, S. S. (2013). Metathesis of 2-butene to propylene over W-mesoporous molecular sieves: A comparative study between tungsten containing MCM-41 and SBA-15. *Applied Catalysis A: General*, *467*, 224-234.
8. Epelde, E., Ibañez, M., Aguayo, A. T., Gayubo, A. G., Bilbao, J., & Castaño, P. (2014). Differences among the deactivation pathway of HZSM-5 zeolite and SAPO-34 in the transformation of ethylene or 1-butene to propylene. *Microporous and mesoporous materials*, *195*, 284-293.
9. Corma, A., Corresa, E., Mathieu, Y., Sauvanaud, L., Al-Bogami, S., Al-Ghrami, M. S., & Bourane, A. (2017). Crude oil to chemicals: light olefins from crude oil. *Catalysis Science & Technology*, *7*(1), 12-46.
10. Khan, T. A., Saud, A. S., Jamari, S. S., Ab Rahim, M. H., Park, J. W., & Kim, H. J. (2019). Hydrothermal carbonization of lignocellulosic biomass for carbon rich material preparation: A review. *Biomass and bioenergy*, *130*, 105384.
11. Wang, H., Wu, Y., Guo, S., Dong, C., & Ding, M. (2020). γ-Valerolactone converting to butene via ring-opening and decarboxylation steps over amorphous SiO2-Al2O3 catalyst. *Molecular Catalysis*, *497*, 111218.
12. Marranca, J. T., Koenig, G., & Neurock, M. (2014). *Theoretical Insights into the Conversion of y-Valerolactone to Butene Over y-Alumina* (Doctoral dissertation, Thesis, University of Virginia).
13. Gupta, S., Arora, R., Sinha, N., Alam, M. I., & Haider, M. A. (2016). Mechanistic insights into the ring-opening of biomass derived lactones. *RSC advances*, *6*(16), 12932-12942.
14. Wang, S., Li, H., & Xu, L. (2006). Application of zeolite MCM-22 for basic dye removal from wastewater. Journal of colloid and interface science, 295(1), 71-78.

15. Woszuk, A., & Franus, W. (2017). A review of the application of zeolite materials in warm mix asphalt technologies. Applied Sciences, 7(3), 293.

16. Lew, C. M., Rajabbeigi, N., & Tsapatsis, M. (2012). Tin-containing zeolite for the isomerization of cellulosic sugars. Microporous and mesoporous materials, 153, 55-58.

17. Weitkamp, J. (1982). Isomerization of long-chain n-alkanes on a Pt/CaY zeolite catalyst. Industrial & Engineering Chemistry Product Research and Development, 21(4), 550-558.

18. Wielers, A. F. H., Vaarkamp, M., & Post, M. F. M. (1991). Relation between properties and performance of zeolites in paraffin cracking. Journal of catalysis, 127(1), 51-66.

19. Sousa-Aguiar, E. F., Trigueiro, F. E., & Zotin, F. M. Z. (2013). The role of rare earth elements in zeolites and cracking catalysts. Catalysis today, 218, 115-122.

20. Maxwell, I. E., & Stork, W. H. J. (1991). Hydrocarbon processing with zeolites. In Studies in surface science and catalysis (Vol. 58, pp. 571-630). Elsevier.

21. Zhang, Q., Li, X., Asami, K., Asaoka, S., & Fujimoto, K. (2004). Synthesis of LPG from synthesis gas. Fuel Processing Technology, 85(8-10), 1139-1150.

22. Hudec, P., Smiešková, A., Schneider, P., & Ŝolcová, O. (2002). Determination of microporous structure of zeolites by t-plot method—state-of-the-art. In *Studies in surface science and catalysis* (Vol. 142, pp. 1587-1594). Elsevier.

23. Storck, S., Bretinger, H., & Maier, W. F. (1998). Characterization of micro-and mesoporous solids by physisorption methods and pore-size analysis. *Applied Catalysis A: General*, *174*(1-2), 137-146.

24. Farneth, W. E., & Gorte, R. J. (1995). Methods for characterizing zeolite acidity. *Chemical reviews*, *95*(3), 615-635.

25. Palkhiwala, A. G., & Gorte, R. J. (1999). Characterization of H-FER and H-TON using temperature-programmed desorption of alkylamines. *Catalysis letters*, *57*(1), 19-23.

26. Emeis, C. A. (1993). Determination of integrated molar extinction coefficients for infrared absorption bands of pyridine adsorbed on solid acid catalysts. *Journal of Catalysis*, *141*(2), 347-354.

27. Zaker, A., Guerra, P., Wang, Y., Tompsett, G. A., Huang, X., Bond, J. Q., & Timko, M. T. (2018). Evidence of heterogeneous catalytic activity of ZSM-5 in supercritical water for dodecane cracking. *Catalysis Today*, *317*, 2-11.

28. Kellicutt, A. B., Salary, R., Abdelrahman, O. A., & Bond, J. Q. (2014). An examination of the intrinsic activity and stability of various solid acids during the catalytic decarboxylation of γ-valerolactone. *Catalysis Science & Technology*, *4*(8), 2267-2279.

29. Jiang, C., Wang, Y., Zhang, H., Chang, N., Li, L., Xie, K., & Mochida, I. (2019). Effect of initial Si/Al ratios on the performance of low crystallinity Hβ-x zeolite supported NiMo carbide catalysts for aromatics hydrogenation. *Catalysis Science & Technology*, *9*(18), 5031-5044.

30. Abraham, A., Lee, S. H., Shin, C. H., Hong, S. B., Prins, R., & van Bokhoven, J. A. (2004). Influence of framework silicon to aluminium ratio on aluminium coordination and distribution in zeolite Beta investigated by 27 Al MAS and 27 Al MQ MAS NMR. *Physical Chemistry Chemical Physics*, *6*(11), 3031-3036.

31. Madon, R. J., & Boudart, M. (1982). Experimental criterion for the absence of artifacts in the measurement of rates of heterogeneous catalytic reactions. *Industrial & Engineering Chemistry Fundamentals*, *21*(4), 438-447.

32. Bond, J. Q., Jungong, C. S., & Chatzidimitriou, A. (2016). Microkinetic analysis of ring opening and decarboxylation of γ-valerolactone over silica alumina. *Journal of Catalysis*, *344*, 640-656.

33. Jones, A. J., & Iglesia, E. (2015). The strength of Brønsted acid sites in microporous aluminosilicates. *Acs Catalysis*, *5*(10), 5741-5755.

34. Schröder, K. P., Sauer, J., Leslie, M., Richard, C., Catlow, A., & Thomas, J. M. (1992). Bridging hydrodyl groups in zeolitic catalysts: a computer simulation of their structure, vibrational properties and acidity in protonated faujasites (H☐ Y zeolites). *Chemical physics letters*, *188*(3-4), 320-325.

35. Solans-Monfort, X., Branchadell, V., Sodupe, M., Sierka, M., & Sauer, J. (2004). Electron hole formation in acidic zeolite catalysts. *The Journal of chemical physics*, *121*(12), 6034-6041.

36. Grajciar, L., Arean, C. O., Pulido, A., & Nachtigall, P. (2010). Periodic DFT investigation of the effect of aluminium content on the properties of the acid zeolite H-FER. *Physical Chemistry Chemical Physics*, *12*(7), 1497-1506.

37. Damjanović, L., & Auroux, A. (2009). Determination of acid/base properties by temperature programmed desorption (TPD) and adsorption calorimetry. In *Zeolite characterization and catalysis* (pp. 107-167). Springer, Dordrecht.

38. Hossain, M. Z., Chowdhury, M. B., & Charpentier, P. A. (2019). Effect of surface acidity of Al2O3 supported metal catalysts on catalytic activity and carbon deposition during SCWG of glucose. *Biomass and Bioenergy*, *124*, 142-150.

39. Yu, K., Kumar, N., Aho, A., Roine, J., Heinmaa, I., Murzin, D. Y., & Ivaska, A. (2016). Determination of acid sites in porous aluminosilicate solid catalysts for aqueous phase reactions using potentiometric titration method. *Journal of Catalysis*, *335*, 117-124.

40. Naranov, E. R., Sadovnikov, A. A., Maximov, A. L., & Karakhanov, E. A. (2018). Development of micro-mesoporous materials with lamellar structure as the support of NiW catalysts. *Microporous and Mesoporous Materials*, *263*, 150-157.

41. Kofke, T. G., Gorte, R. J., & Kokotailo, G. T. (1989). Determination of framework concentrations of gallium in [Ga]-ZSM-5. *Applied Catalysis*, *54*(1), 177-188.

42. Chakraborty, B., & Viswanathan, B. (1999). Surface acidity of MCM-41 by in situ IR studies of pyridine adsorption. *Catalysis Today*, *49*(1-3), 253-260.

43. Vishwanathan, V., Jun, K. W., Kim, J. W., & Roh, H. S. (2004). Vapour phase dehydration of crude methanol to dimethyl ether over Na-modified H-ZSM-5 catalysts. *Applied Catalysis A: General*, *276*(1-2), 251-255.

44. Adebajo, M. O., Long, M. A., & Frost, R. L. (2004). Spectroscopic and XRD characterisation of zeolite catalysts active for the oxidative methylation of benzene with methane. *Spectrochimica Acta Part A: Molecular and Biomolecular Spectroscopy*, *60*(4), 791-799.

45. Fu, J., Feng, X., Liu, Y., & Yang, C. (2017). Effect of pore confinement on the adsorption of mono-branched alkanes of naphtha in ZSM-5 and Y zeolites. *Applied Surface Science*, *423*, 131-138.

46. Carr, R. T., Neurock, M., & Iglesia, E. (2011). Catalytic consequences of acid strength in the conversion of methanol to dimethyl ether. *Journal of Catalysis*, *278*(1), 78-93.

Chapter 6

Future Works

6.1 Future investigation of the activity of ZrO$_2$

In Chapter 4, we have observed that ZrO$_2$ has the highest activity and relatively high Lewis acid strength but low stability. It is worth digging into the potential of such material as a Lewis catalyst. The ZrO$_2$ samples we used in our study were purchased from Thermal Fisher. However, based on the recent reports, the catalytic performance of ZrO$_2$ was proved to be sensitive with its structures and had a unique preparation protocol to make ZrO$_2$ as Lewis acids.

There are three major phases of the crystal structure of zirconia: monoclinic, tetragonal, and cubic. Under room temperature, ZrO$_2$ presents in a monoclinic phase, and it can be transformed into tetragonal phase after heating up to 1100°C. And the latter can be further converted into cubic phase under 2370°C [1,2]. A report has also observed that m-ZrO$_2$ has more severe deactivation comparing to t-ZrO$_2$. In the first hour, m-ZrO$_2$ can lose 50% of initial activity, and this deactivation increases to 80% after 10 hours. Thus, even though they exhibit similar initial activities, the actual productid can be quite different after a small amount of time [3].

Furthermore, the ZrO$_2$ was reported to be synthesized from the salt formation of zirconium. One way to prepare ZrO$_2$ was to use zirconium tetrapropoxide as the precursor. After dissolving zirconium tetrapropoxide in water at room temperature, precipitates can be collected by filtration. ZrO$_2$ power was produced after calcination of dried precipitate at 673K for 8 hours in airflow [4]. Another reported method was to apply zirconyl nitrate hydrate as the precursor. After dissolving zirconyl nitrate hydrate and dried in the oven at 333K for 12 hours and then calcined in air for 673K for 5 hours, m- ZrO$_2$ can be obtained. If one wants to get t-ZrO$_2$, the calcination should be increased to 1173K for 3 hours [5]. Based on this knowledge, we prepared a ZrO$_2$ sample from zirconyl nitrate hydrate with the previously described method, and the surface area was tested based on N$_2$ physical adsorption. The result is summarized in table 6.1. As shown in the table, the

surface area of lab prepared ZrO_2 is significantly improved from 7.4 m^2/g to 90 m^2/g, almost 13 times more than that of ZrO_2 from the commercial supplier. Therefore, considering the enhancement in surface area, it is pertinent to further use the TPD method to examine the acidity on the new sample surface. Also, this lab-prepared ZrO_2 should be packed into the reactor and perform the activity test for the GVL ring opening reaction.

	ZrO_2 (Commercial)	ZrO_2 (Lab Prepared)
BET Surface Area (m^2/g)	7.4369	90.7359
t-Plot External Surface Area (m^2/g)	1.7255	87.8654
t-plot Micropore Area (m^2/g)	5.7114	2.8706
BET Avg Pore Diameter (Å)	101.1125	105.62
BJH Ads Pore Diameter (Å)	103.92	92.001
BJH Des Pore Diameter (Å)	72.325	79.627

Table 6.1: Summary surface information based on BET analysis of N_2 physical adsorption between ZrO_2 from commercial supplier and from Zirconyl nitrate hydrate.

6.2 Microkinetic modeling of GVL ring opening over zeolites

Based on the data collected in Chapter 5, we have already found the difference in turnover frequency between various zeolites with different structures. And the strength of the Brønsted acid site in the zeolite was proved to be influenced by the local structures around the acid site and zeolite framework. To probe the intrinsic decarboxylation activity of GVL ring opening over various zeolites, microkinetic modeling is essential for rigorously discussing the site strength and structural influence.

Previously, Jesse et al. have built a microkinetic model to describe the trends in GVL ring opening and decarboxylation over amorphous silica alumina [6]. This model allows one to not only predict the product distribution in various reaction environments but also regress kinetic and thermodynamic parameters such as barrier for elementary step, heats of chemisorption, and

interaction energy. It is possible to implement this model to explain the activity we observed in zeolites.

To perform the simulation, we need to measure the apparent kinetic data for GVL ring opening, PEA ring closure, GVL decarboxylation and PEA decarboxylation. Thus, the reaction requires to be examined from both directions of GVL/PEA interconversion by feeding GVL and feeding PEA. Also, partial pressure and contact time study will be included to increase the accuracy of the simulation.

However, different from ASA, GVL ring opening and decarboxylation over zeolites have shown more severe deactivation comparing that over ASA. It will be challenging to count for deactivation and trace back to estimate the "zero time on stream" activity, which makes the partial pressure and contact time study may be unreliable. Our plan is to develop a new model with the expression of GVL and PEA concentration to simply our simulation with similar accuracy.

 For now, we have collected PEA ring closure and decarboxylation profiles for MFI-23.0, MFI-30.1, MFI-50.0, MFI-200.0, MFI-500.0. Figure 6.1 illustrates the reaction rate profile over MFI-
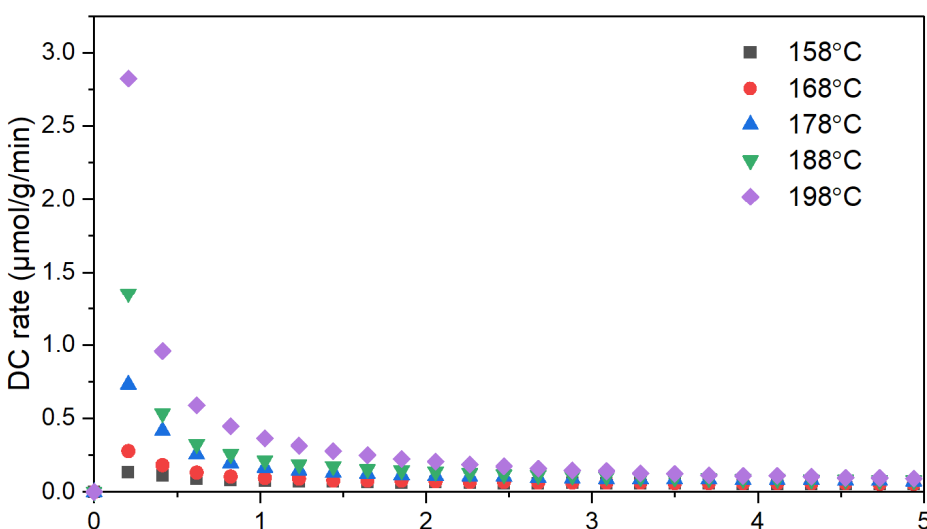

Figure 6.1: The mass normalized rate of PEA decarboxylation as a function of time on stream over MFI 30:1 ranging from 158°C to 198 °C at 10 mbar with Helium as balance gas.
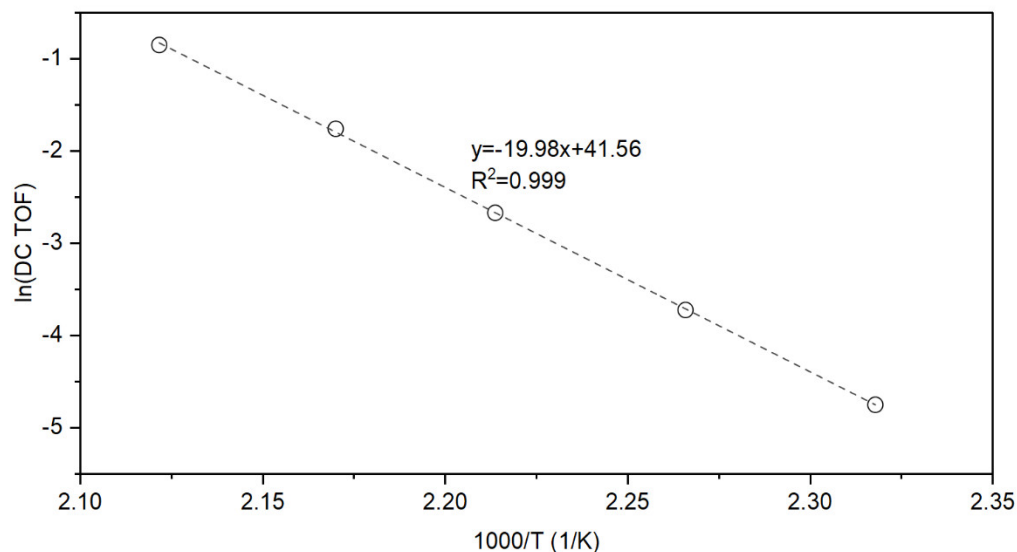
Figure 6.2: Arrhenius plot illustrating the temperature dependence of PEA decarboxylation over MFI 30:1. The unit of DC turnover frequency is hr^{-1}.

23.0 as a function of time on stream. We can see that PEA ring closure and decarboxylation deactivate significantly in the initial hour. It loses almost 90% of the original activity. Fortunately, by applying the optimized first order deactivation model mentioned in Chapter 5, we manage to regress for the initial rate of PEA ring closure and decarboxylation rate at zero time on stream. Figure 6.2 showed the Arrhenius plots for MFI 30.0. And this method has been extended to other materials, giving a good fit to calculate PEA decarboxylation's apparent barrier. These apparent
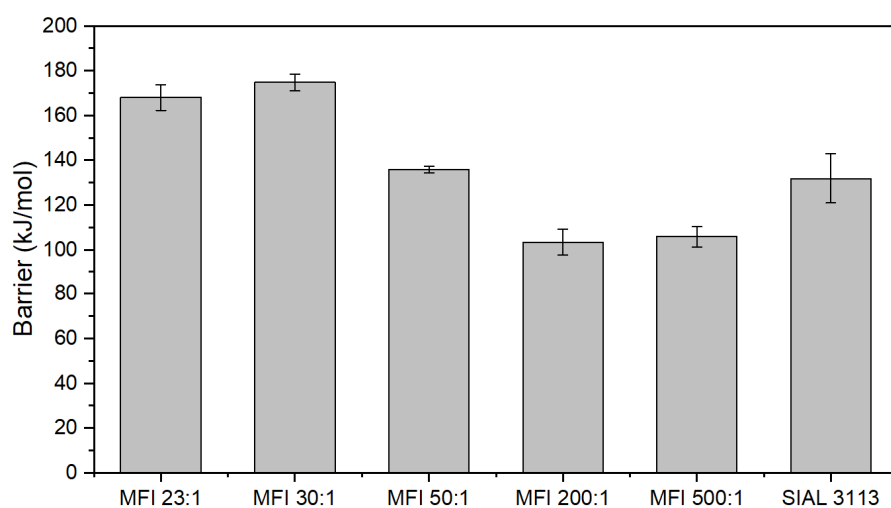

Figure 6.3: Apparent barriers measured for PEA decarboxylation over MFI 23:1, MFI 30:1, MFI 50:1, MFI 200:1, MFI 500:1 and SIAL 3113 under differential conditions at 198℃ and 10 mbar PEA and 1 bar total pressure in a Helium balance.

barriers are summarized in figure 6.3. We can observe that the apparent barriers for PEA decarboxylation over MFI 23:1 and MFI 30:1 were higher than that over other zeolites. The rigorous explanation will be probed later by the simulation results to examine the effect of local environments and confinement effects in zeolites.

6.3 Selective Hydrogenation of biomass derivatives over PtSn bimetallic catalysts

Hydrogenation is a vital process in biomass upgrading [7,8]. Considering the multiple function groups in the biomass derivatives, selective hydrogenation is always challenging but essential for producing valuable chemicals. Monometallic catalysts such as platinum (Pt) and ruthenium (Ru) have been used in industry for a while [9,10]. However, they suffer from low selectivity and catalyst poisoning. Based on previous research, Pt catalyst can lead to decarbonylation. Meanwhile, Ru catalyst is more favorable for decarbonylation and methanation during hydrogenation of biomass-derived chemicals, making it difficult to realize high selectivity towards the target product.

Stassi *et al*. found that by introducing a second metal site such as Sn or Fe into the Pt catalysts, one can significantly improve selectivity to HDO products during hydrogenation of unsaturated aldehyde [11]. PtSn bimetallic seems to only show activity in HDO reaction. Based on our knowledge in Chapter 4, which proves that γ-Al$_2$O$_3$ was an ideal Lewis catalyst for the selective preparation of PEA. Therefore, we proposed a PtSn bimetallic catalyst supported by γ-Al$_2$O$_3$ for selective hydrogenation of LA, GVL or PEA to make valuable compounds. Our lab has performed several preliminary studies to examine the activity for hydrogenation of propanoic acid over PtSn supported by γ-Al$_2$O$_3$. The results showed high selectivity and yield towards propanol. Further studies have been extended to examine the hydrogenation activity over biomass derivatives such as velaric acid (VA), levulinic acid (LA), pentenoic acid (PEA), and γ-valerolactone (GVL).
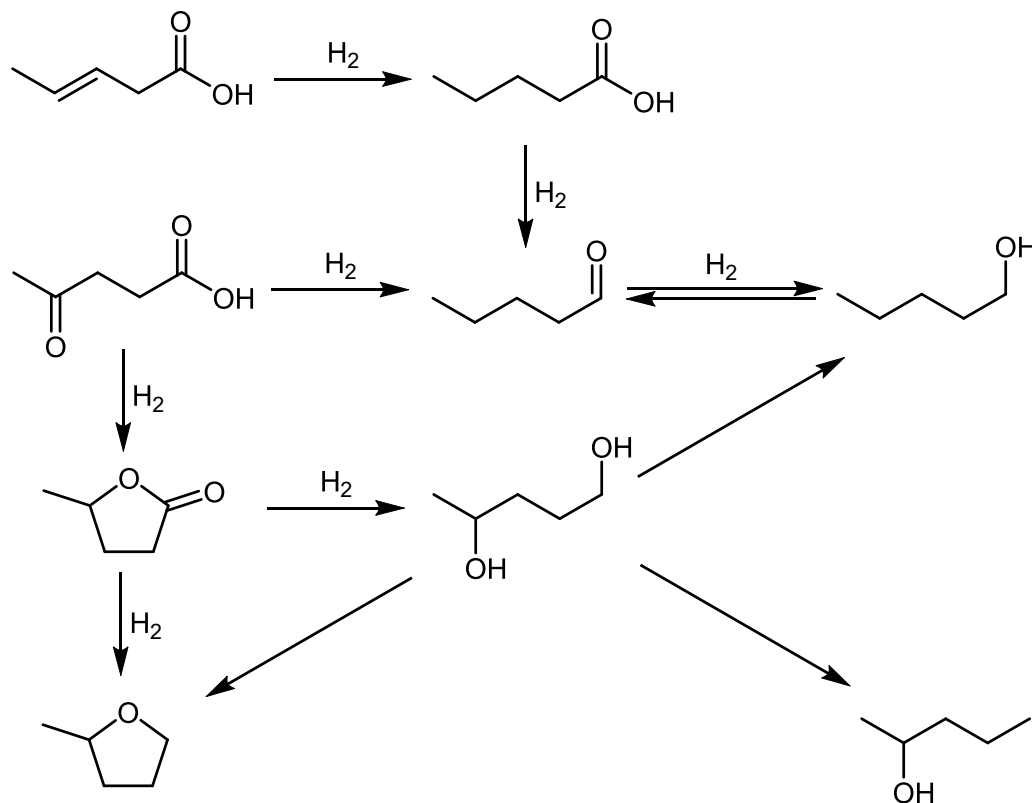
Figure 6.4: Reaction pathways for the hydrogenation of lignocellulose derived biochemicals: LA, GVL, VA and PEA.

Figure 6.4 shows the reaction network of hydrogenation over these compounds. First, after optimizing the reaction temperature and contact time, selectivity hydrogenation of velaric acid to pentanol can be achieved at 198C with a contact time of 10 hr. The pentanol yield can reach 80% with more than 90% selectivity. Although selective hydrogenation to pentanol over pentenoic acid can still be realized, the unsaturated double bond in PEA is also hydrogenated, decreasing the value of this reaction. However, we found that over PtSn, γ-valerolactone can be converted into 2-Methyltetrahydrofuran (2-MTHF). The selectivity to 2-MTHF is more than 90% but the yield remains to be optimized. Moreover, levulinic acid can be transformed into GVL and 2-MTHF over PtSn, the conversion of levulinic is near 100%, 75% selectivity towards GVL and 20% selectivity towards 2-MTHF was observed at 158°C.

The mechanism for the selective hydrogenation over PtSn bimetallic remains elusive [12,13]. Here, we proposed that the synergetic effect between Pt and Sn may contribute to the increase in the yield and selectivity of alcohol products. As figure 6.5 illustrates, over the surface of PtSn catalyst, Pt site serves as a Metal active site that activates H_2 while the Sn site serves as an electrophilic site that activates C=O bond. Group VIII metals such as Pt have been reported as a typical metal active site. However, introducing Sn as an electrophilic site is not commonly reported. This is the first time that PtSn bimetallic catalyst has been applied in this type of reaction. Moreover, the reason why the C=C in pentenoic acid was hydrogenated is that selective hydrogenation of is that the electron density in the oxygen of C=O group in unsaturated carboxylic acid is weaker comparing to that in the oxygen in C=O group in unsaturated aldehyde, limiting the interaction between electrophilic site and C=O group. As a result, the C=C may also have access to contact the active hydrogen on the surface, thus reducing the selectivity towards unsaturated products.

Currently, even if the PtSn bimetallic catalysts may not be selectivity in hydrogenate unsaturated carboxylic acid, the unique synergetic effect between bimetallic active site makes it different from other monometallic catalysts. It is still worthy further investigating the activity in hydrogenation of the α,β-unsaturated compounds such as cinnamaldehyde, 2-cyclohexenone and crotonaldehyde.
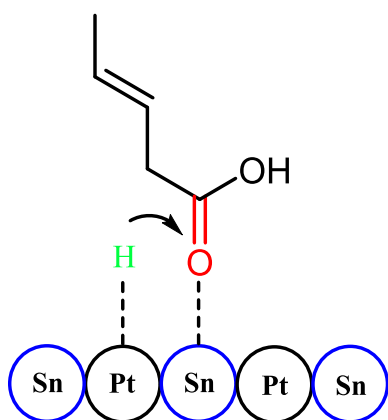

Figure 6.5: Proposed mechanism for synergetic effect during selective hydrogenation of unsaturated carboxylic acid, where Pt serves as a metal active site to activate hydrogen and Sn serves as an electrophilic site to activate C=O.

6.4 Selective preparation of pentadiene and butadiene from biomass derivatives

Diene compounds such as 1,4-butadiene or pentadiene are important industrial precursors for many commercial products such as SBR synthetic rubber, PBR synthetic rubber, Latex synthetic rubber, plastics, C_5 hydrocarbon resins, and adhesives [14]. By 2025, the global diene market will keep growing [15]. Diene chemicals are considered as by-products during ethylene production and are traditionally extracted from the steam cracking process of crude oil and naphtha [16]. However, due to the rapid expansion of ethane cracking in recent years, the production of diene chemicals has been declining in recent years. Thus, a selective and energy-friendly synthesis strategy to achieve on-purpose production of diene compounds is quite demanding.

Omar *et al*. recently reported that selective production of butadiene was achieved from dehydra-decyclization of tetrahydrofuran (THF) over self-pillared pentasil (SPP) (90% selectivity, 89% conversion of THF) [17]. In this study, pentadiene is also obtained from 2-MTHF over SPP in the
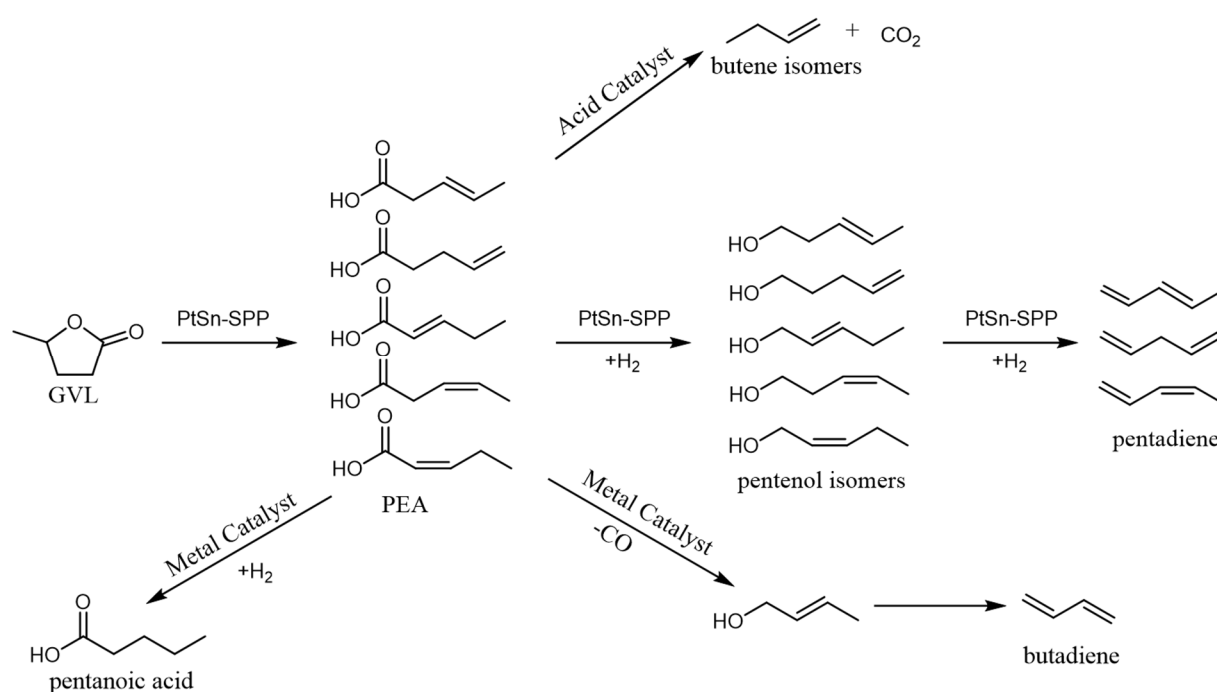

Figure 6.6: Scheme of proposed strategy to produce butadiene and pentadiene from selective hydrogenation, decarbonylation and dehydration with GVL and PEA as feedstock.

same environment. Furthermore, PtSnK supported on silica catalysts was reported to be used for the selective preparation of α-olefins through deoxygenation of methyl esters [18]. Combining these applications with the results we found over PtSn catalysts, we propose a strategy to produce pentadiene and butadiene based on biomass derivatives. Figure 6.6 demonstrates the proposed reaction strategies. If selective hydrogenation of PEA to form pentenol or selective hydrogenation of GVL to form 2-MTHF can be achieved, pentadiene can be acquired through subsequent dehydration over SPP catalyst. Also, butadiene is possible to be obtained through decarbonylation of pentenol over metal catalyst. To realize these plans, catalysts design, reactor design, catalytic kinetics, and thermodynamics are required. Overall, the opportunities and challenges we present here remain to be resolved in future studies.

6.5 Reference

1. Basu, B., Vleugels, J., & Van Der Biest, O. (2004). Transformation behaviour of tetragonal zirconia: role of dopant content and distribution. *Materials Science and Engineering: A*, *366*(2), 338-347.
2. Stevens, R. (1986). "An Introduction to Zirconia." Magnesium Elektron Publication No. 113.
3. Ji, Y., Lawal, A., Nyholm, A., Gorte, R. J., & Abdelrahman, O. A. (2020). Dehydra-decyclization of tetrahydrofurans to diene monomers over metal oxides. *Catalysis Science & Technology*, *10*(17), 5903-5912.
4. Komanoya, T., Nakajima, K., Kitano, M., & Hara, M. (2015). Synergistic catalysis by Lewis acid and base sites on ZrO2 for Meerwein–Ponndorf–Verley reduction. *The Journal of Physical Chemistry C*, *119*(47), 26540-26546.
5. Zhang, Y.-C., Davison, S., Brusasco, R., Qian, Y.-T., Dwight, K., & Wold, A. (1986). preparation and characterization of tetragonal ZrO2. *Journal of the Less Common Metals*, *116*(1), 301-306.
6. Bond, J. Q., Jungong, C. S., & Chatzidimitriou, A. (2016). Microkinetic analysis of ring opening and decarboxylation of γ-valerolactone over silica alumina. *Journal of Catalysis*, *344*, 640-656.
7. Choudhary, T. V., & Phillips, C. B. (2011). Renewable fuels via catalytic hydrodeoxygenation. *Applied Catalysis A: General*, *397*(1-2), 1-12.
8. Furimsky, E. (2000). Catalytic hydrodeoxygenation. *Applied Catalysis A: General*, *199*(2), 147-190.
9. Nimmanwudipong, T., Runnebaum, R. C., Block, D. E., & Gates, B. C. (2011). Catalytic conversion of guaiacol catalyzed by platinum supported on alumina: Reaction network including hydrodeoxygenation reactions. *Energy & fuels*, *25*(8), 3417-3427.
10. Nelson, R. C., Baek, B., Ruiz, P., Goundie, B., Brooks, A., Wheeler, M. C., Frederick, B. G., Grabow, L. C., & Austin, R. N. (2015). Experimental and theoretical insights into the hydrogen-efficient direct hydrodeoxygenation mechanism of phenol over Ru/TiO2. *ACS catalysis*, *5*(11), 6509-6523.
11. Stassi, J. P., Zgolicz, P. D., de Miguel, S. R., & Scelza, O. A. (2013). Formation of different promoted metallic phases in PtFe and PtSn catalysts supported on carbonaceous materials used for selective hydrogenation. *Journal of Catalysis*, *306*, 11-29.
12. Lan, X., & Wang, T. (2020). Highly selective catalysts for the hydrogenation of unsaturated aldehydes: a review. *ACS catalysis*, *10*(4), 2764-2790.
13. Tamura, M., Nakagawa, Y., & Tomishige, K. (2020). Recent developments of heterogeneous catalysts for hydrogenation of carboxylic acids to their corresponding alcohols. *Asian Journal of Organic Chemistry*, *9*(2), 126-143.
14. Wojtkielewicz, A. (2013). Application of cross metathesis in diene and polyene synthesis. *Current Organic Synthesis*, *10*(1), 43-66.
15. Xiaoming, L. Y. W. (2005). Production and Market of Butadiene [J]. *Advances in Fine Fetrochemicals*, *7*.
16. Sun, R., Zheng, M., Li, X., Pang, J., Wang, A., Wang, X., & Zhang, T. (2017). Production of renewable 1, 3-pentadiene from xylitol via formic acid-mediated deoxydehydration and palladium-catalyzed deoxygenation reactions. *Green Chemistry*, *19*(3), 638-642.

17. Abdelrahman, O. A., Park, D. S., Vinter, K. P., Spanjers, C. S., Ren, L., Cho, H. J., Vlachos, D. G., Fan, W., Tsapatsis, M., & Dauenhauer, P. J. (2017). Biomass-derived butadiene by dehydra-decyclization of tetrahydrofuran. *ACS Sustainable Chemistry & Engineering*, *5*(5), 3732-3736.

18. Chiappero, M., Do, P. T. M., Crossley, S., Lobban, L. L., & Resasco, D. E. (2011). Direct conversion of triglycerides to olefins and paraffins over noble metal supported catalysts. *Fuel*, *90*(3), 1155-1165.

VITA

NAME OF AUTHOR:

Xinlei Huang

PLACE OF BIRTH:

Wuhan, Hubei, China

UNDERGRADUATE SCHOOLS ATTENDED:

Central China Normal University, Hubei, Wuhan, China

DEGREES AWARDED:

Bachelor of Science in Chemistry, 2013, Central China Normal University

Bachelor of Art in English, 2013, Central China Normal University

POSSESSIONAL EXPERIENCE

Department of Biomedical and Chemical Engineering, Syracuse University

Research Assistant, 05/2019 – present

Teaching Assistant, 09/2016 – 05/2019